

Physics of Solar Prominences: II - Magnetic Structure and Dynamics

D.H. Mackay* · J.T. Karpen · J.L.
Ballester · B. Schmieder · G. Aulanier

Received: date / Accepted: date

Abstract Observations and models of solar prominences are reviewed. We focus on non-eruptive prominences, and describe recent progress in four areas of prominence research: (1) magnetic structure deduced from observations and models, (2) the dynamics of prominence plasmas (formation and flows), (3) Magneto-hydrodynamic (MHD) waves in prominences and (4) the formation and large-scale patterns of the filament channels in which prominences are located. Finally, several outstanding issues in prominence research are discussed, along with observations and models required to resolve them.

Keywords Solar Magnetic Fields · Solar Prominences · Oscillations · MHD waves

Contents

1	Introduction	2
2	Magnetic Structure of Filaments and Prominences	3
3	Plasma Structure and Dynamics	21
4	Magneto-hydrodynamic Waves in Solar Prominences	29
5	Formation and Large-Scale Patterns of Filament Channel and Filaments	44
6	Open Issues	65

* The authors would like to thank Aad van Ballegooijen for his hard work and dedication without which this review would not exist.

D.H. Mackay
School of Mathematics and Statistics, University of St Andrews, North Haugh, St Andrews, Fife, Scotland, KY16 9SS. E-mail: duncan@mcs.st-and.ac.uk

J.T. Karpen
Code 674, NASA Goddard Spaceflight Center, Greenbelt, MD 20771, USA.

J.L. Ballester
Departament de Física, Universitat de les Illes Balears, E-07122 Palma de Mallorca, Spain.

B. Schmieder
LESIA, Observatoire de Paris, 92195 Meudon Cedex Principal, France.

G. Aulanier
LESIA, Observatoire de Paris, 92195 Meudon Cedex Principal, France.

1 Introduction

Solar prominences consist of relatively cool, dense plasma that is suspended in the solar corona at heights up to 100 Mm above the chromosphere. They are observed as “filaments” on the solar disk, where they are seen in absorption in strong spectral lines (such as H α) and in the Extreme Ultraviolet (EUV) continuum. When described as “prominences” they are seen above the solar limb, where they appear as bright features against the dark background. In this review the terms “filament” and “prominence” will be used interchangeably. The existence of cool, dense plasma suspended in the hot corona has been a mystery ever since the first observations of filaments and prominences (reviewed in Hirayama, 1985; Zirker, 1989; Tandberg-Hanssen, 1995). The discovery by Babcock and Babcock (1955) that solar filaments lie between different polarities of the Sun’s magnetic field, provided one piece of the puzzle by identifying the primary source of support and constraint for the prominence mass (Kippenhahn and Schlüter, 1957). However, the magnetic structure of prominences is still not fully understood, with many observations and theoretical models differing on the exact nature of the magnetic field. As a result the physical processes governing the origin and subsequent behavior of the prominence plasma remain a lively topic of debate.

In recent years, high-resolution observations of prominences from the ground and from space have greatly improved our knowledge of the structure and dynamics of prominence plasmas. There have also been renewed efforts to measure the vector magnetic fields in and below solar prominences using spectro-polarimetric methods (see López Ariste and Aulanier, 2007). These observations have inspired a wide variety of theoretical models describing different aspects of the physics of prominences. The purpose of this review is to report on the progress that has been made in recent years, since the comprehensive review by Tandberg-Hanssen (1995). Both state of the art space and ground based observations, along with models in four different areas of prominence research will be described. The four areas are chosen to give a broad overview of solar filaments, from the smallest structures currently observed, to their properties found on their scale size and finally filament properties on a global scale. These specific topics are:

1. **Prominence magnetic structure** : The first topic describes the basic structure and morphology of solar filaments, including new high resolution observations and magnetic field measurements obtained from ground and space. The relationship of filaments to their underlying magnetic field along with recently developed static 3D magnetic field models, many of which are derived from observations, are described.
2. **The dynamics of prominence plasmas (formation and flows)**: The second topic considers the underlying physics and complex range of models that may describe the origin and behavior of the filaments mass. Models include those based around magnetic forces, such as injection or levitation mechanisms, to thermal pressure force models of evaporation and condensation. In particular, significant new work on thermal non-equilibrium models is discussed.
3. **MHD waves in prominences**: The third topic considers the significant advances that have been made in the last 10 years in observing and modeling the small-scale oscillations observed in filaments and prominences. The effect of flows and damping mechanisms on linear-MHD waves is discussed.
4. **The formation and large-scale patterns of filament channels**: The final topic considers the properties of filament channels and filaments in a global con-

text. In particular H α observations and theoretical models for the formation of filaments and filament channels are discussed, along with schemes used to categorize filaments.

Other aspects of prominence research, including results from space-based spectroscopy of solar prominences, are considered in the review by (Labrosse *et al.*, 2009, hereafter Paper I). We focus on the properties of non-eruptive prominences.

2 Magnetic Structure of Filaments and Prominences

In this section we first describe recent observations relevant to prominence magnetic structure, and then describe related modeling.

2.1 Observations

2.1.1 Basic Properties

Filaments are always located above Polarity Inversion Lines (PILs), i.e., lines on the photosphere where the radial component B_r of the magnetic field changes sign. Filaments can be found above PILs inside activity nests consisting of multiple bipolar pairs of spots (“active regions filaments”), at the border of active regions (“intermediate filaments”), and on the quiet Sun (“quiescent filaments”), including the polar crown. This nomenclature refers to their location on the Sun relative to underlying magnetic fields and not with respect to their internal plasma motions. Intermediate and active region filaments are located at sunspot latitude belts, however quiescent filaments may exist over all latitudes on the Sun. On the quiet sun the magnetic fields are concentrated into discrete network elements that are well separated from each other, with much weaker fields in between. Therefore, a PIL on the quiet sun is actually a zone of mixed polarity, and the precise location of the PIL can best be defined by using spatially smoothed magnetograms (Jones, 2004). An example of a quiescent filament seen in H α through different instruments, along with the underlying photospheric magnetic field distribution can be seen in Figure 1. In the next paragraph we first consider the basic structure of filaments as seen on the solar disk. Following this, the varying structures that are found when prominences are viewed above the limb are illustrated.

Filaments typically consists of 3 structural components: a spine, barbs, and two extreme ends. The spine runs horizontally along the top of the filament, although there may be sections along the filament where the spine is nearly invisible. The barbs protrude from the side of the filament (see Figure 1(b) bottom panel) and when observed closer to the limb, using standard instrumentation with moderate spatial resolution, the barbs are seen to extend down from the spine to the chromosphere below. The barbs, as well as the ends of the filament (also called “legs”) may be a collection of threads that appear to terminate at a single point or at multiple points (Lin *et al.*, 2008a). When viewing a quiescent filament on the solar disk at high resolution, H α observations indicate that each of these three structural components consist of thin thread-like structures (see examples in Malherbe, 1989; Martin, 1998; Pecseli and Engvold, 2000). In Figure 2 these thin threads may be seen, where the observations are at the limit of present day resolution. The threads are found to have widths of about 200 km

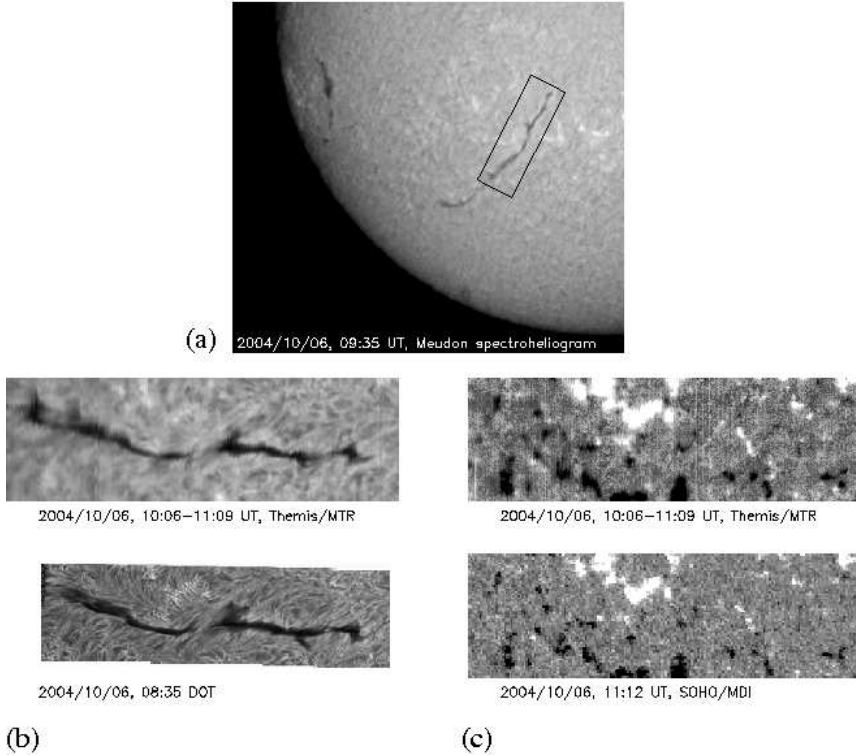


Fig. 1 $H\alpha$ filament observed on 6th October 2004 from Dudik *et al.* (2008). (a) Meudon spectroheliograph in $H\alpha$ line core at 09:35 UT. The box corresponds to the THEMIS/MTR field of view. (b) THEMIS/MTR (10:06–11:09 UT) and DOT (08:35 UT) observations in $H\alpha$ line center. (c) THEMIS/MTR (10:06–11:09 UT) and SoHO/MDI (11:12 UT) longitudinal magnetograms, both saturate at ± 40 G.

(Lin *et al.*, 2005a,b, 2008a,b) and are not necessary aligned with the structural component of the filament to which they belong. Individual threads have lifetimes of only a few minutes, but the filament as a whole can live for many days. These thin threads are thought to be aligned with the local magnetic field. Lin *et al.* (2005a) find that for quiescent $H\alpha$ filaments it is not possible to associate the ends of individual filament threads with bright points in G-band images (such bright points are proxies for small kilogauss flux elements in the photosphere). They conclude that filament threads are located in thin bundles of field lines that are longer than the observed threads, i.e., only a fraction of each field line is filled with absorbing plasma. In a recent paper, Lin *et al.* (2008a) argue that at high resolution, all filaments ranging from active region to quiescent are made up of such thin threads. While short threads are commonly seen in quiescent filaments, active region filaments seem to be composed of relatively longer threads. These differences may be related to the average angle made by the magnetic field to the axis of the filament spine.

In contrast to the view on the disk, when observed above the solar limb different prominences can have very different appearance as can be seen from the three examples in Figure 3. In some cases the prominence consists of a collection of nearly horizontal threads or elongated blobs (Figure 3(a)), similar to the features seen in

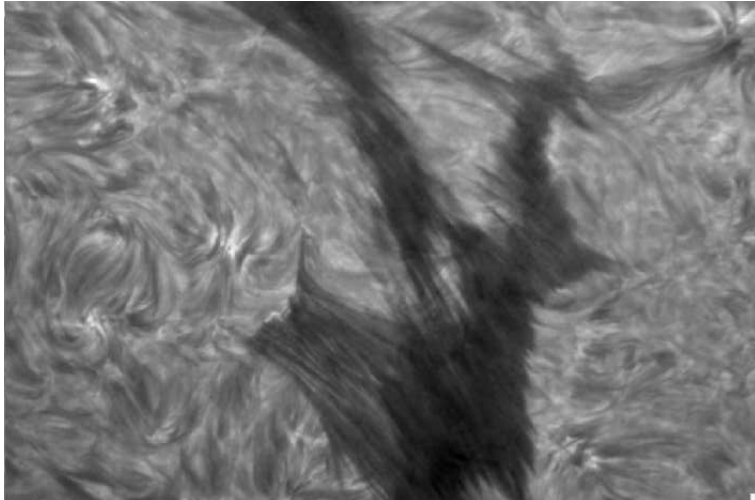


Fig. 2 High-resolution H α images obtained from the Swedish Solar Telescope illustrating thin threads aligned with the local magnetic field (from Lin *et al.* (2005a)).

filaments on the disk. High-resolution H α and Ca II H observations of prominences have recently been obtained with the Solar Optical Telescope (SOT) on the Hinode Satellite. Okamoto *et al.* (2007) observed horizontal threads in a prominence near an active region and studied the oscillatory motions of these threads. A movie of the evolution of these threads may be seen in Okamoto *et al.* (2007). These horizontal threads are most likely aligned with the local magnetic field. In other cases, the prominence consists of a collection of quasi-vertical threads (Figure 3(b) and (c)). Berger *et al.* (2008) observed a hedge-row prominence and found that the prominence sheet is structured by both bright quasi-vertical threads and dark inclusions. The bright structures are down-flow streams with velocity of about 10 km s^{-1} , and the dark inclusions are highly dynamic up-flows with velocity of about 20 km s^{-1} . It is unclear what drives these up-flows and down-flows. The down-flow velocities are much less than the free-fall speed, indicating that the plasma is somehow being supported against gravity (Peceli and Engvold, 2000; Mackay & Galsgaard, 2001). How these quasi-vertical threads relate to the magnetic field in such *hedge-row prominences* is not well understood. For example, Schmieder *et al.* (2009) have shown that dopplershift line-of-sight velocities in such threads can be of the same magnitude as observed vertical velocities. Assuming field-aligned flows, the authors argue for the existance of an oblique magnetic field in 3D, that is projected on the plane of the sky. In addition, it is unclear how the lower altitude quasi-vertical threads seen above the limb relate to the barb threads seen in filaments on the disk. A major challenge of prominence research is to reconcile the different structures observed in filaments and prominences when seen on the disk versus limb.

Filaments and prominences can also be observed in the H I Lyman lines (e.g., Korendyke *et al.*, 2001; Heinzel *et al.*, 2001b; Patsourakos and Vial, 2002; Schmieder *et al.*, 2007; Gunár *et al.*, 2007) and in the He II 304 Å resonance line (Wang, 1999). These lines likely originate in the prominence-corona transition region (PCTR). While prominences simultaneously observed in He II 304 Å and H α must lie in the same mag-

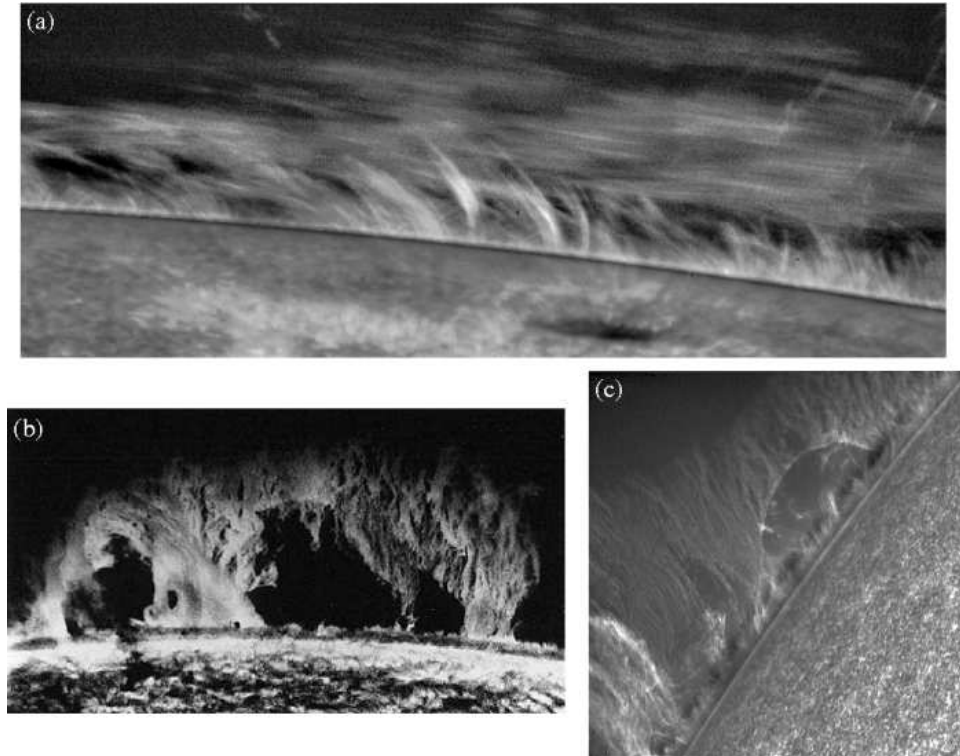


Fig. 3 Examples of solar prominences at the limb in different wavelengths: (a) Ca II H HINODE/SOT image from November 9, 2006 (from Okamoto *et al.* (2007)) ; (b) BBSO H α image from 1970; (c) Ca II H HINODE/SOT image (courtesy of T. Berger).

netic configuration, they commonly have different morphologies (Wang *et al.*, 1998; Heinzel *et al.*, 2001a; Aulanier and Schmieder, 2002; Dudik *et al.*, 2008). Differences may include the observed width and whether the spine is visible or not. Such differences may be explained by different formation mechanisms of these lines (see sections 8.1 and 8.2 in Paper I) and their optical depths. Another question that arises from considering different lines in prominences, is whether lines formed from ions and neutrals should exhibit the same prominence structure and if so what role ion-neutral coupling plays in this?. Observations of prominences with the SUMER instrument on board the Solar and Heliospheric Observatory (SoHO) satellite have shown that the Lyman lines have asymmetric profiles, indicating that (1) there are multiple threads along the line of sight, and (2) the threads move relative to each other with velocities of order 10 km s $^{-1}$ (Gunár *et al.*, 2008). For more detailed discussion of these observations, see sections 8 and 9 of Paper I.

It should be kept in mind that the “filament” plasma seen in absorption on the disk may not be exactly the same as the “prominence” plasma seen above the limb some days earlier (East limb) or later (West limb). One complication in comparing filaments and prominences is that the prominence fine structure changes continually with time. Also, active region filaments, those filaments lying within the centers of activity complexes, generally lie at such low heights (less than 10Mm, the approximate

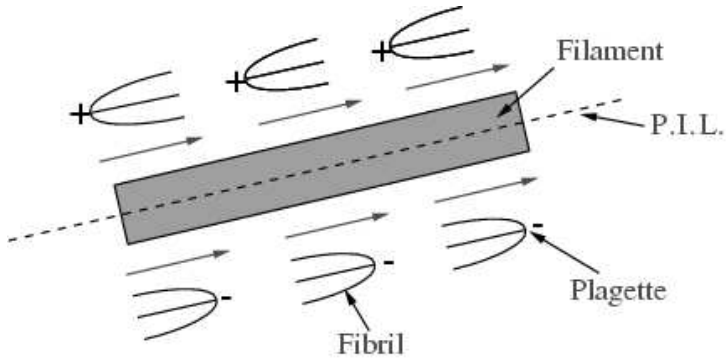


Fig. 4 Schematic of a filament channel with fibrils which lie (1) anti-parallel to one-another on either side of the PIL and (2) nearly parallel to the path of the PIL. The anti-parallel alignment indicates that the magnetic field (arrows) is dominantly horizontal and points in the same direction on either side of the channel.

height of the spicule forest) that they are difficult to see at the limb. Figure 3 (a) and (c) illustrate prominences which lie at active latitudes, but can be seen above the spicular forest. They may be seen, as they are not active region filaments but rather “intermediate filaments” which lie on the borders of active regions and can reach much higher heights. Some prominences can be clearly seen in He II 304 Å above the limb, but may not be so easily visible on the disk because of temperature and density effects (see section 8.2 of Paper I). Schmieder *et al.* (2003) and Schwartz *et al.* (2006) show that cool plasma ($\sim 10^4$ K) with very low density could be present in the vicinity of filaments. This plasma is not visible in H α but is detectable in EUV due to absorption of UV line radiation by the Lyman continuum (see Paper I). This may explain why prominences do not have the same aspect as filaments when crossing the limb.

2.1.2 Filament Channels

Filaments are located in *filament channels*, described as regions in the chromosphere surrounding a PIL where the chromospheric fibrils are aligned with the PIL (Martres, 1966; Gaizauskas, 1998). These fibrils are interpreted as giving the direction of the magnetic field in the chromosphere. Foukal (1971a,b) noted that the fibrils emanating from magnetic elements in the channel show a streaming pattern that is opposite on the two sides of the channel (see Figure 4). Given the magnetic polarity of these elements, Foukal deduced that the horizontal component of magnetic field must point in the same direction on the two sides of the channel (also see Martin *et al.*, 1992, 1994). This magnetic field along the PIL is believed to extend some height into the corona, and the filament is embedded in this field. The existence of this horizontal field within filaments was confirmed by direct measurements using the Zeeman and Hanle effects (Hyder, 1965; Rust, 1967; Leroy *et al.*, 1983; Leroy, 1989; Zirker *et al.*, 1998b). Martin *et al.* (1992) introduced the concept of *chirality* of filament channels. They classified filament channels as either “dextral” or “sinistral” depending on the direction of the axial component of the field as seen by an observer standing on the positive-polarity side of the channel (Figure 5). To determine the chirality of filament channels, which do not necessarily contain a filament, high resolution H α images (to

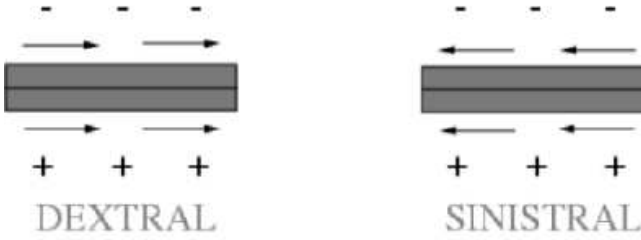


Fig. 5 The *chirality* of a filament channel is defined in terms of the direction of the magnetic field along the channel (denoted by arrows) when viewed by an observer on the positive polarity side of the channel. For a dextral (sinistral) channel, the magnetic field points to the right (left).

resolve individual chromospheric fibrils) are required. In strong field regions usually only H α images are required. In contrast, for weak field regions where fibril patterns are not strong, magnetograms may also be used to aid the determination of chirality, by using them to determine the polarity of the magnetic elements from which the fibrils extend from or go into. Martin *et al.* (1994) showed that channels in the northern hemisphere are predominantly dextral, while those in the south are predominantly sinistral (also see Leroy *et al.*, 1983; Zirker *et al.*, 1997). The origin of this hemispheric pattern will be further discussed in Sections 5.1.2 and 5.5.

As magnetic fields in filament channels are believed to extend to higher heights and the filament embedded in this field. Filaments may also be classified as being of “dextral” and “sinistral type”. The chirality of filaments may be deduced, either, indirectly from that of the channel or directly from magnetic field measurements (also see Leroy *et al.*, 1983). To date no simultaneous studies comparing the chirality in filaments determined both indirectly and directly has taken place.

Spectral diagnostics of the magnetic field orientation in a prominence observed with SUMER can also be used. Lyman lines have reversed/non-reversed profiles when the magnetic field of the prominence is perpendicular/parallel to the line of sight (Heinzel *et al.*, 2005). This has been tested by Schmieder *et al.* (2007) with a round shaped filament crossing the limb. In the EUV, filament channels are much broader than H α filament channels (Heinzel *et al.*, 2001a; Aulanier and Schmieder, 2002). Heinzel *et al.* (2001a) explain this enhanced width by absorption of EUV line radiation by the H I Lyman continuum; lower emission in the channel (“emissivity blocking”) is another mechanism. Aulanier and Schmieder (2002) used their magnetic flux tube models to deduce that magnetic field lines with concavities may be present in EUV filament channels where plasma is cool. The existence of concave up magnetic field lines has been tested recently by polarimetric measurements, in filament channels (Lites, 2005) and close to the feet of filaments (López Ariste *et al.*, 2006).

2.1.3 Filament Barbs

When observed from above (i.e., at disk center), the filament barbs are seen to protrude at an acute angle with respect to the long axis of the filament, like ramps off an elevated highway (Martin *et al.*, 1992). Therefore, filaments can be classified as either *right-bearing* or *left-bearing* depending on the directions of the barbs as seen from above. Martin and collaborators found a one-to-one correlation between the right/left-

bearing structure of the barbs and the chirality of the filament channel: filaments in dextral channels have right-bearing barbs, and those in sinistral channels have left-bearing barbs. An important goal of filament modeling is to explain the cause of this relationship. Bernasconi *et al.* (2005) have developed software for automated detection of filament barbs and the chirality of filament channels.

When observed away from disk center, the barbs are seen to be inclined structures that extend from the filament spine to the chromosphere below (e.g., SST observations of Lin *et al.*, 2008a). The vertical extent of a barb is much larger than the gravitational scale height of the prominence plasma (about 200 km), so the barbs cannot be static field-aligned structures; the plasma must somehow be supported against gravity. Therefore, a key issue is the orientation of the magnetic field in the barbs. This issue will be further discussed in section 2.2.

The relationship between the filament barbs and the underlying photospheric magnetic field has been discussed by many authors. Martin *et al.* (1994) argue that the ends of the barbs of filaments on the disk are connected to weak magnetic fields in between the network elements. Martin and Echols (1994) propose that the filament barbs are anchored in parasitic (minority) polarity elements, i.e., weak magnetic fields with opposite polarity compared to the dominant (majority) polarity elements on the side of the filament where the barb is located. Aulanier *et al.* (1998) show that the barbs move in accordance with the changes of parasitic polarities during one day of observations. Wang (1999, 2001), Chae *et al.* (2005) and Lin *et al.* (2005a) find that the ends of the barbs are located very close to small-scale PILs between majority and minority polarities on the side of the filament.

Wang (2001) and Wang and Muglach (2007) proposed that flux cancellation between the parasitic polarity and the neighboring dominant polarity plays a key role in the formation of filament barbs. Flux cancellation refers to the disappearance of photospheric magnetic flux by mutual interaction of opposite polarity fields in the photosphere (Livi *et al.*, 1985; Martin *et al.*, 1985). It occurs everywhere on the Sun, but is particularly common at large-scale PILs on the quiet Sun where opposite polarity elements intermix and a zone of mixed polarity is created. At the edge of such a mixed-polarity zone, parasitic flux elements are likely to cancel against dominant polarity elements. Wang (1999, 2001) argued that magnetic reconnection accompanying photospheric flux cancellation is the dominant mechanism for injecting mass into quiescent prominences. In contrast, Martens and Zwaan (2001) propose that downward-inclined barbs, linked to parasitic polarity elements, arise as a result of failed cancellation, i.e., the motion of flux elements across the PIL without cancellation. Changes of minor polarities in filament channels lead to strong changes of H α filaments and prove directly the relationship between minor polarities and barbs/ends of filaments. The disappearance and reappearance of a part of a filament has been directly related to emergence of magnetic flux, followed by canceling flux (Schmieder *et al.*, 2006).

Zirker *et al.* (1998a) observed counter-streaming of plasma in a quiescent filament (see section 4, Paper I). Using observations at three wavelengths in the H α line, they found evidence that matter flows along the spine of the filament in both directions. Similar counter-streaming occurs within the barbs: in one wing of the spectral line they observe up-flows from the barbs into the spine, while in the other wing they see down-flows. It is unclear what drives these flows, but they appear to be parallel to the magnetic field. Therefore, the observed flow direction can be used to infer the direction of the magnetic field, which may help resolve the question whether the magnetic fields in barbs are inclined or horizontal. Zirker *et al.* (1998a) propose that a filament barb

consists of a set of closely spaced flow channels that are highly inclined with respect to the vertical direction, with some channels having up-flows and others having down-flow. The velocities involved are 5 to 10 km/s, much less than the free-fall velocity corresponding to the filament height. Deng *et al.* (2002) found counter-streaming in an active region filament. Lin *et al.* (2003) and Schmieder *et al.* (2008) observed such flows in large polar crown filaments two days before filament eruptions, so the counter-streaming may be a signature of the slow rise of a filament before eruption. With new high-resolution observations such as those by Hinode, many more examples of counterstreaming are expected to be found. With this it will be determined whether counterstreaming is a property common to all filaments and prominences, or whether it is a signature of the early stages of the onset of eruption.

To investigate the nature of magnetic fields in the photosphere below and around barbs, polarimetric measurements were recently made by López Ariste *et al.* (2006) using THÉMIS/MTR (Télescope Héliographique pour l'Etude du Magnétisme et des Instabilités Solaires). In Figure 6 an illustration of the 3D field can be seen, where white/black denotes the positive/negative normal field component and the red arrows, the direction of the horizontal field. Through using filament channel chirality rules to resolve the 180° ambiguity, the authors deduce that the field is of inverse polarity at the level of the photosphere. This type of photospheric configuration, with a collection of high altitude magnetic dips crossing the local PIL, as hinted from Figure 6, may fit many different structures of the coronal field lying above. An alternative interpretation of the coronal structure associated with the measured photospheric magnetic field is a vertical current sheet with no connections across the PIL. However such a structure is not stable to any form of non-ideal MHD perturbation and is likely to be short lived. Non-ideal MHD perturbations would first result in the tearing of the field (Furth *et al.*, 1963) and then the formation of an X-point structure (when viewed in a 2D projection along the PIL). Subsequent reconnection would then produce connections across the PIL. Depending on the force balance of the field and the nature of the extended current systems formed in the relaxation process, either a coronal arcade (of normal polarity) or bald patch (of inverse polarity) may result. As the long term existence of such a current sheet is unlikely, and since the photospheric field is of inverse polarity, the authors deduce that bald patches, i.e. magnetic dips that touch the photosphere, are present. These magnetic dips or hammocks are deduced to support the plasma in the barbs. Such observations are a major step in understanding the magnetic field structure in filaments and barbs. However to fully understand the magnetic field in filaments, new high resolution polarimetric measurements in many filaments are required.

2.1.4 Measurements of Prominence Magnetic Field

While observations of prominence fine structure provide some clues to the magnetic topology, the most direct determination of the prominence magnetic field comes from the inversion of spectro-polarimetric data (see reviews by Paletou and Aulanier, 2003; Paletou, 2008; López Ariste and Aulanier, 2007). Only a few spectral lines in the optical spectrum of prominences are suitable for magnetic field measurements using Hanle-effect diagnostic (the Hanle effect is the change in the polarization state of resonantly scattered radiation due to presence of a magnetic field). The H α line is strong and has interesting polarization profiles (López Ariste *et al.*, 2005; Bianda *et al.*, 2006; Ramelli *et al.*, 2006), but the line is generally optically thick and the polarization transfer in this line is not understood. The lines most often used for measuring prominence

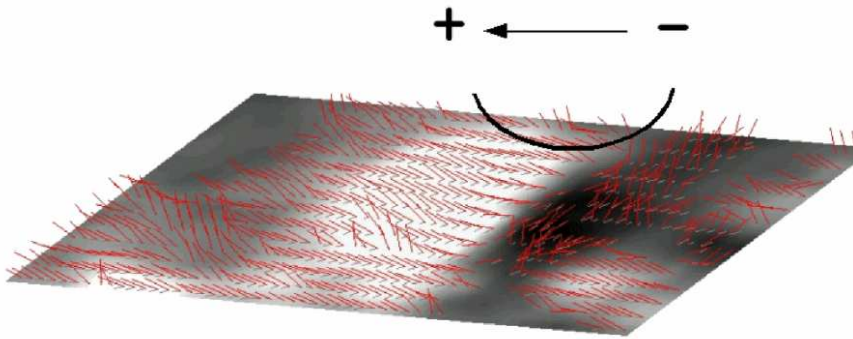


Fig. 6 Vector magnetic field in a filament channel as observed with THÉMIS. From López Ariste *et al.* (2006).

magnetic field are the He I multiples at 5876 Å in the visible (He D₃) and at 10830 Å in the near-infrared. For recent attempts in modeling these lines see Léger & Paletou (2009). The spatial resolution of such measurements is typically a few arc seconds, i.e., they cannot yet resolve the fine-scale structures seen in high-resolution images of prominences such as those obtained in SOT.

A comprehensive effort to measure prominence magnetic fields was conducted in the 1970's and early 1980's, using the facilities at *Pic du Midi* (France) and Sacramento Peak Observatory (USA). The results of this work are reviewed by Leroy (1989), and can be summarized as follows (Paletou and Aulanier, 2003). The magnetic field in quiescent prominences has a strength of 3–15 G. The field is mostly horizontal and makes an acute angle of about 40° with respect to the long axis of the prominence (Bommier and Leroy, 1998). The field strength increases slightly with height, indicating the presence of dipped field lines. Most prominences have *inverse* polarity, i.e., the component of magnetic field perpendicular to the prominence has a direction opposite to that of the potential field. The component along the prominence axis obeys a large-scale pattern (Hyder, 1965; Rust, 1967; Leroy *et al.*, 1983), which is now known as the chirality pattern (Martin *et al.*, 1994; Zirker *et al.*, 1997) and will be further discussed in Sections 5.1.2 and 5.5. In the following discussion unless otherwise stated, angles given for the magnetic field in prominences are measured as an acute angle relative to the long axis of the prominence. Many features may effect these measurements, such as the position of the filament on the disk and the spatial resolution of the images. For each set of observations the reader should refer back to the original papers for such information.

Lin *et al.* (1998) presented the first full-Stokes spectro-polarimetric observations of a filament on the disk in He I 10830 Å. Trujillo Bueno *et al.* (2002) demonstrated the importance of lower-level atomic polarization in such measurements (the lower level of the 10830 Å line is the ground level of the triplet system of neutral helium). They showed that this atomic polarization creates linear polarization of radiation in forward scattering at disk center. This provides a new technique for measuring the azimuth of magnetic fields in filaments. Collados *et al.* (2003) applied this method to observations of two filaments in the Northern hemisphere. They find that the magnetic field is nearly horizontal, and that the magnetic vector is rotated with respect to the filament axis by an angle in the range 15 to 25 degrees.

Paletou *et al.* (2001) reported full-Stokes observations of a prominence in He D₃. Besides linear polarization signals due to the Hanle effect, they also found circular polarization signals and they derived magnetic field strengths of 30–45 G in an active part of the prominence. Casini *et al.* (2003) published the first map of the vector field in a prominence. They found that the average magnetic field in prominences is consistent with earlier studies (see Leroy, 1989): a mostly horizontal field with a strength of about 20 G and with the magnetic vector pointing 20° to 30° off the prominence axis. In addition, the map shows magnetic fields significantly stronger than average (up to 80 G) in clearly organized patches within the prominence (also see Wiehr and Bianda, 2003; López Ariste and Casini, 2002, 2003; López Ariste and Aulanier, 2007). It is unclear whether these structures are related to the fine structures of quiescent prominences (e.g., vertical threads).

Casini *et al.* (2005) discuss various aspects of Stokes profile inversion, including the problem of finite optical depth of the He D₃ line in the prominence, and the effects of line-of-sight integration of the polarization signals from different magnetic configurations. They confirm the presence of magnetic fields significantly stronger than average in limited regions of the prominence. They also emphasize the importance of full Stokes inversion for a correct diagnostic of magnetic fields in prominences. For certain values of magnetic field strength and inclination of the field with respect to the vertical direction, the Van Vleck effect produces a 90° ambiguity in the position angle of the magnetic field as projected onto the plane of the sky (in addition to the well-known 180° ambiguity). This 90° ambiguity makes it difficult to distinguish between horizontal and vertical fields in certain cases, and including Stokes V in the analysis helps disentangle this ambiguity. However, the results from the earlier studies based only on linear polarization measurements are thought not to be strongly affected by this ambiguity (López Ariste, private communication).

Recently, Merenda *et al.* (2006) observed He I 10830 Å in a polar crown prominence above the limb, and found evidence for fields of about 30 G that are oriented only 25° from the vertical direction. The reason for the different orientation of the magnetic field in this prominence (compared to the more horizontal fields found in other studies) is unclear. One possibility is the 90° ambiguity due to the Van Vleck effect, but the authors claim their particular measurement is unambiguous.

2.1.5 Magnetic Fields and Flows in the Photosphere Below the Prominence

An indirect method for probing the prominence magnetic field is to measure the vector field in the photosphere below the prominence. López Ariste *et al.* (2006) deduced the presence of magnetic dips in the photosphere below a filament after having resolved the 180-degree ambiguity in photospheric vector-field measurements using the chirality rules for filaments (see Figure 6). These so-called *bald patches* are sites on the PIL where the horizontal field perpendicular to the PIL has “inverse” polarity, i.e., the field points from negative to positive polarity, opposite to the direction expected for a potential field (see also Lites, 2005). López Ariste *et al.* (2006) argue that the dips are consistent with the presence of a weakly twisted flux rope in the corona above the PIL. If this is the case, the filament is thought to be supported by similar dips in the helical field lines at larger heights.

Flows in the photosphere below the prominence may play an important role in the evolution and stability of the magnetic field supporting the prominence. Observations of shear flows, highlighted by maps of the vorticity, have been found below filaments, but

mostly during their eruption (Balasubramaniam et al., 1998; Keil et al., 1999). Until recently, observations of organised photospheric flows below quiescent filaments were very rare. Rondi *et al.* (2007) measured meso- and super-granular flows in the vicinity and below a filament before and during its eruption. They found that the disappearance of the filament starts where both parasitic and normal magnetic polarities are swept by a continuously diverging flow corresponding to supergranular diffusion. They also observed the interaction of opposite polarity elements, which is another candidate for triggering the filament destabilization as it implies a reorganization of the overlying coronal magnetic field.

Roudier *et al.* (2008) studied large-scale horizontal flows in the photosphere below a filament, using series of full-disk Dopplergrams and magnetograms obtained with the Michelson Doppler Imager (MDI) on SoHO. In Dopplergrams, the supergranular pattern is tracked using local correlation tracking (LCT), while in magnetograms LCT is used to obtain horizontal velocities. The topology of the observed large-scale flow-field changes during the eruptive phase suggests a coupling between the surface flows and the coronal magnetic field. An unusually fast north-south flow stream of amplitude 30 to 40 m s⁻¹ was found to be compatible with the rotation of a part of the filament. This behavior suggests that the filament footpoints have been moved by the surface flows. The influence of the flow stream was enhanced by differential rotation. The authors measured an increase of the zonal shear in the region below the starting point of the eruption, and a decrease after the eruption. These results indicate that, even if large-scale flows do not lead to large-scale changes of the photospheric magnetic field, they nevertheless might be able to perturb the coronal field to an extent that filament eruptions and coronal mass ejections can be triggered.

2.1.6 Coronal Structures Above the Filament Channel

Quiescent prominences are located in cavities at the base of coronal helmet streamers (Engvold, 1989). In white-light observations above the limb, the cavity is darker than its surroundings and the height and width of the cavity is roughly twice the height of the prominence (Saito and Tandberg-Hanssen, 1973). Some streamers contain concentric arch systems (Saito and Hyder, 1968), suggesting the presence of an arcade of coronal loops overlying the cavity. Low and Hundhausen (1995) argue that the cavity represents a magnetic flux rope.

In EUV and X-ray observations of filament channels on the solar disk, the coronal loops overlying a prominence often cannot be clearly identified, perhaps because they are too faint compared with the lower-altitude structures. However, X-ray arcades can often be seen in active regions, and after eruptive events on the quiet Sun (Martin and McAllister, 1996). The coronal loops in these arcades do not cross the PIL at right angles, but are skewed in the direction along the PIL (“sigmoids”). The loops can be right-bearing or left-bearing with respect to the direction along the PIL (as seen from above). The observations indicate that dextral (sinistral) channels have left (right)-skewed coronal arcades, opposite to the right (left)-bearing structure of the filament barbs (Martin and McAllister, 1996; Martin, 1998; McAllister *et al.*, 2002; Schmieder *et al.*, 2004). Taking into account the polarity of the dominant flux on either side of the filament, this implies that the axial component of magnetic field in the arcade is the same as that in the filament channel. Therefore, this implies that the filament channel observed in the chromosphere is part of a larger structure that extends to heights well above the prominence.

2.2 Models of Prominence Magnetic Structure

The above-mentioned observations show that prominences are embedded in magnetic fields that are highly non-potential. As the dominant component of the field lies along the filaments long axis, such non-potential fields exhibit strong magnetic shear. However, the detailed structure of these fields and the associated electric currents are not well understood. In the following we review various models for prominence magnetic structure. To begin with we focus on models that describe the structure as it exists at one instant of time, and we in general will ignore for the moment the question of how the field came to be that way. In Section 3 we will see that the mass in prominences is in fact dynamic. However since the flow speed is generally much less than the Alfvén speed and within filaments the plasma- β is low, such motions are often expected to be along field lines and not to strongly effect the field. Therefore, under this approximation, static modeling is useful to describe the large-scale magnetic field structure of the prominence. This field is expected to evolve on times-scales much longer than that of the observed flows. Issues related to the formation of the prominence magnetic field and its evolution will be addressed in Sect. 5.

An important question in prominence modeling concerns the role of magnetic dips in the structure and dynamics of the prominence plasma. Kippenhahn and Schlüter (1957) showed how cool plasma can be supported against gravity by a magnetic field containing *dips* in the field lines, i.e., sites where the field lines are locally horizontal and curved upward. For example, dips can occur in a potential field when the underlying photospheric magnetic sources have a quadrupolar structure (“quadrupolar dips”). However, the magnetic fields in filament channels are not potential, and contain significant electric currents. Dips in non-potential magnetic fields can occur for several reasons:

1. The structure of the magnetic field is significantly affected by the *weight* of the prominence plasma, distorting the field in such a way as to create magnetic dips. Two examples are the isothermal Kippenhahn and Schlüter (1957) model and the non-isothermal Hood & Anzer (1990) extension. In both the shape of the dipped field lines is determined by the balance between magnetic and gravitational forces. Many authors have constructed magneto-hydrostatic (MHS) models of prominence threads based on the Kippenhahn-Schlüter model (e.g., Malherbe and Priest, 1983; Heinzel and Anzer, 2001; Heinzel *et al.*, 2005; Low and Petrie, 2005). Another example is the “normal polarity” flux rope model by Low and Zhang (2002). In this model the sense of magnetic twist in the flux rope is opposite to that in the overlying coronal arcade, and the force of gravity plays a crucial role in the existence of dipped field lines. In Paper I, Section 9.2 the Kippenhahn-Schlüter model is used to compute the hydrogen spectrum in non-LTE modeling.
2. Another possibility is that the dips exist in the absence of prominence plasma, i.e., the dips are not caused by the weight of the prominence. According to such models, the filament plasma is likely to be located near the dips of the field lines (see, however, Section 3). If the plasma $\beta < 1$, these currents must flow nearly parallel to the field lines, so that the magnetic field is approximately force-free (β is the ratio of gas pressure and magnetic pressure). Such *force-free fields* can contain dips in the field lines even when the underlying photospheric field is dipolar. In fact, many authors have suggested that filaments are supported by nearly force-free *flux ropes* that lie horizontally above the PIL (e.g., Kuperus and Raadu, 1974; Pneuman, 1983;

van Ballegooijen and Martens, 1989; Priest *et al.*, 1989; Rust and Kumar, 1994; Aulanier and Démoulin, 1998; Chae *et al.*, 2001; Gibson and Fan, 2006). An alternative force-free configuration with dips, the *sheared arcade*, has also been studied as a description of the filament channel magnetic structure (Antiochos *et al.*, 1994; DeVore and Antiochos, 2000; Aulanier *et al.*, 2006).

In quiescent prominences with low field strengths ($B < 10$ G) we may have a mixture of these two cases: the existence of the dips is due to the presence of a large-scale flux rope or sheared arcade (as in case 2), but the magnetic field near the dips is significantly distorted by the weight of the prominence plasma ($\beta > 1$). In this case there are significant perpendicular currents near the dips, and the flux rope or sheared arcade is not force free.

In the remainder of this section we consider the second category of models which describe the 3D structure of the magnetic field in the prominence, under the approximation that the weight of the prominence plasma does not play an essential role in the large-scale structure of the magnetic field. These models differ in terms of the requirement of dips for the formation and persistence of filaments. While the models differ in this sense, one common feature is that the magnetic field has a strong axial component along the PIL. Such a field may be described as strongly “sheared”. Magnetic shear either in the form of an arcade or a flux rope may build up through a number of process. Examples include: shearing motions (Antiochos *et al.*, 1994), emergence of the upper part of a flux rope (Manchester *et al.*, 2004; Archontis and Török, 2008; DeVore and Antiochos, 2000; Fan, 2009) or shearing motions followed by convergence and cancellation of photospheric flux (van Ballegooijen and Martens, 1990; Litvinenko and Wheatland, 2005). The origin of the axial fields in filaments will be fully discussed in Section 5.1 where a wide range of models and mechanisms for producing magnetic shear are discussed. Returning to the topic of static configurations, Section 2.2.1 discusses the Martin and Echols (1994) Empirical Wire Model, which suggests that dips are not essential. Following this we describe two models in which dips play increasingly important roles. These are the sheared arcade model (Section 2.2.2) and finally the linear and non-linear flux rope models (Section 2.2.3).

2.2.1 Empirical “Wire Model”

Through following a time series of H α observations of a quiescent filament, along with photospheric magnetic field distributions, Martin and Echols (1994), proposed an empirical “wire model” for the magnetic field geometry in a filament. A key assumption of their model is that the fine scale structure observed in H α lies parallel to the magnetic field. In the “wire-model” the filament plasma is located on magnetic arches that are highly sheared in the direction along the PIL. Although they are highly sheared, the arches do not contain dips. This feature distinguishes this model from others discussed in later sections. Some field lines run along the entire length of the filament and outline the filaments “spine”. Other shorter ones run partially along the spine, but spread out from it and connect down to minority polarity elements on either side of the PIL. These shorter structures represent the filament barbs. As neither the spine or barb field lines contain dips, the model requires the existence of other (non-magnetic) forces to act parallel to the inclined field lines to support the cool dense plasma against gravity. Without such forces, the cool plasma would fall down to the chromosphere in a matter of minutes, which is not observed. The model however does not address this

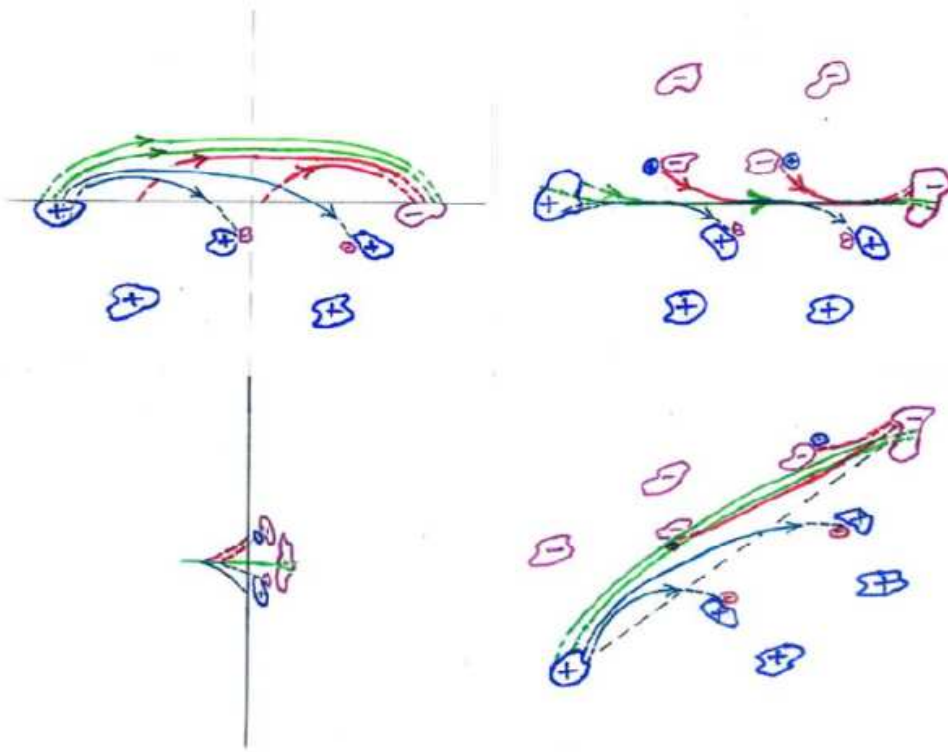


Fig. 7 The Martin and Echols (1994) model of filament magnetic structure. The four panels show a dextral filament as seen from different perspectives. The *green* field lines show the filament spine, and the *blue* and *red* field lines show the barbs. From Lin *et al.* (2008a).

question. In Section 3 possible candidates for such forces will be discussed. While the Martin and Echols (1994) model does not consider the origin of the sheared arcade, such a structure may be formed by shearing motions of the photospheric footpoints or by the emergence of the upper part of a flux rope as will be discussed in Section 2.2.2.

The Martin & Echols model was further discussed and developed by Lin *et al.* (2008a), who presented the diagram shown in Figure 7. The panels illustrate the magnetic field geometry deduced from four high resolution $H\alpha$ images of filaments taken from different angles and including different classifications (active region-top left, intermediate - top right and two quiescent filaments - bottom). In each image the spine is represented by the green field lines and the barbs by blue and red field lines. Finally the end of the filament is denoted by the dashed lines entering the network fields at either end. From high resolution $H\alpha$ images the authors deduce that thread like structures are common to all classifications of filaments and that in some examples the barbs consist of long thin threads that are inclined with respect to the horizontal. The authors conclude that such thin threads as the basic building blocks of all filaments no matter their classification. Subsequently the only difference between classifications may be the relative importance of the spine, barbs and ends.

A key assumption of the Martin & Echols model that is illustrated by Lin *et al.* (2008a) is that as the barbs, which are inclined field lines, spread out from the main

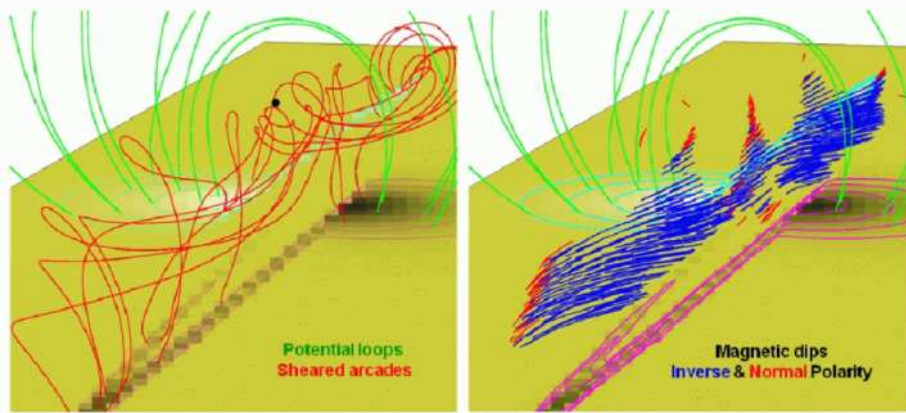


Fig. 8 Sheared arcade model for magnetic field in a filament channel: (a) Sheared field lines (red) with overlying potential loops (green). (b) Distribution of normal polarity (red) and inverse polarity (dark blue) magnetic dips. Each field line is plotted up to a height of 300 km above the dip to simulate the effect of the pressure scale height of the prominence plasma. Adapted from Aulanier *et al.* (2002).

body and only connect to parasitic polarities in the photosphere. If this is the only allowed case it follows that dextral channels produce filaments with right-bearing barbs, and sinistral channels produce left-bearing barbs, consistent with observations. However, as the authors consider barbs as inclined field lines, the model does not explain *why* these inclined field lines cannot extend upwards from network fields on either side and join into the spine, thus producing the opposite bearing orientation of barbs on either side. Therefore, the model only provides a partial explanation for the observed correlation between the right/left-bearing structure of the barbs and the chirality of the filament channel. Later when discussing flux rope models (Section 2.2.3) we will see that these models can provide a possible explanation for this structural asymmetry when magnetic dips are considered.

2.2.2 Sheared Arcade Model

A “sheared magnetic arcade” may be formed for example by shearing motions of the photospheric footpoints localized around the PIL (Antiochos *et al.*, 1994; DeVore and Antiochos, 2000; Aulanier *et al.*, 2002), by the emergence of the upper part of a flux rope or by large-scale vortical motions. Numerical studies of this filament-channel formation mechanism began with a simple bipole embedded in a larger scale background dipolar field, subjected to strong footpoint motions, parallel to the PIL and confined to a narrow zone on either side (DeVore and Antiochos, 2000; DeVore *et al.*, 2005). These oppositely directed flows drag the innermost portion of the bipole into a zone of weaker overlying field, yielding elongated, low-lying field lines that bulge upward at their less constrained ends and hence become dipped. As this stressed system relaxes, a variety of field-line paths are formed: some dipped field lines lean across the PIL, producing inverse polarity compared with the initial bipole, while others reconnect in the corona, producing weakly twisted field lines. Consequently the resulting filament channel is

neither fully normal nor fully inverse polarity. Fig. 8 illustrates the resulting magnetic structure.

2.2.3 Flux Rope Models

In the remainder of this section we consider models in which the weight of the prominence plasma does not play an essential role in the large-scale structure of the magnetic field. Such models may be split into two categories: weakly twisted flux ropes and highly twisted flux ropes (e.g. Rust and Kumar (1994); Okamoto *et al.* (2008)). While two categories exist, we focus on models containing weakly twisted flux ropes with dips in the magnetic field lines; the prominence plasma is assumed to be located at these dips. Weakly twisted flux ropes are only discussed as when non-erupting filaments or prominences are observed, they do not appear to be highly twisted. This is commonly observed in H α images and through flows which are mainly horizontal. In Section 5 when considering models for filament formation a wider range of flux rope models will be discussed including those with strongly twisted flux ropes. Weakly twisted flux ropes are similar to sheared arcades, in the sense that the magnetic field is dominated by the axial component. One constraint on such models is that the flux rope must be approximately in force balance with its surroundings, i.e., the configuration must be close to magneto-static equilibrium, and this equilibrium must be stable. Therefore, a key feature of such models is the existence of a *coronal arcade* overlying the flux rope. The coronal arcade provides the magnetic tension forces necessary to hold down the flux rope in the low corona. Although as previously stated, weakly twisted flux rope models are similar to sheared arcades, there is one key difference. For flux ropes models the flux rope and arcade are independent flux systems with a separatrix surface between them. In contrast, for a sheared arcade only a single flux system exists.

The sense of twist within the flux rope is generally assumed to be consistent with the direction of the magnetic field in the overlying coronal arcade. Since the prominence plasma is located in the dips of the helical windings, the flux rope model predicts that the magnetic field at the prominence has *inverse* polarity with respect to the surrounding photospheric fields, consistent with Hanle measurements (Leroy *et al.*, 1984). Furthermore, the models predict that filament channels with dextral orientation of the axial field have left-helical flux ropes and left-skewed coronal arcades, and sinistral channels have right-helical flux ropes and right-skewed arcades. This is consistent with the observation that dextral (sinistral) channels have left (right)-skewed arcades (Martin and McAllister, 1996; McAllister *et al.*, 2002; Schmieder *et al.*, 2004).

If the effects of gas pressure and gravity are ignored, the magnetic field $\mathbf{B}(\mathbf{r})$ must be more or less *force-free* with electric currents flowing parallel or anti-parallel to the field lines:

$$\nabla \times \mathbf{B} = \alpha \mathbf{B}. \quad (1)$$

Here $\alpha(\mathbf{r})$ is the so-called torsion parameter, which is constant along the field lines ($\mathbf{B} \cdot \nabla \alpha = 0$). The degree of twist of the flux rope is a matter of debate. In some models the magnetic field lines inside the flux rope are highly twisted, but in others the central part of the flux rope is only weakly twisted and the field lines inside this core are nearly parallel to the flux rope axis. The key difference between such models is the spatial distribution of $\alpha(\mathbf{r})$. In models with strong twist, $\alpha(\mathbf{r})$ has its peak on the axis of the flux rope, whereas in models with weak twist $\alpha(\mathbf{r})$ has a hollow core distribution with the peak value of $\alpha(\mathbf{r})$ occurring at the interface between the flux

rope and its local surroundings (e.g., Bobra *et al.*, 2008; Su *et al.*, 2009). The observed field-aligned flows may be difficult to explain with highly twisted flux ropes.

2.2.4 Linear Magneto-hydrostatic Models

Aulanier and collaborators have developed 3D magnetic models of filaments by extrapolating photospheric magnetograms into the corona, assuming either linear force free fields (LFFF, Aulanier and Démoulin, 1998) or linear magneto-hydrostatic fields (LMHS, Aulanier *et al.*, 1998, 1999, 2000; Aulanier and Démoulin, 2003; Dudik *et al.*, 2008). Such models produce helical flux ropes overlying the PIL, and the filament plasma is assumed to be located at dips in the helical field lines. The flux rope may be perturbed by the presence of magnetic elements in the photosphere. In areas where parasitic polarity elements are located close to the flux rope, the dips extend away from the main body of the filament, consistent with the observation that filament barbs are located near parasitic polarities (Martin and Echols, 1994; Martin, 1998; Wang, 2001). A key feature of the flux rope model is that the dips that represent the main body of the filament are all of inverse polarity. Therefore only minority polarity elements may perturb them to produce extended dips away from the main flux rope that represent barbs. Due to the direction of the axial field in the flux rope, combined with the inverse polarity nature, such a perturbation always results in a right/left-bearing structure of barbs in dextral/sinistral orientations of the axial field (Martin *et al.*, 1992, 1994). Therefore the flux rope model, along with any other model that exhibits these same properties, provides a natural explanation for the observed orientation of barbs. In addition the flux rope model resolves the problem of the opposite orientation of filament fine structures and the overlying loops, which is a real problem for the Martin & Echol's model.

The modeling by Aulanier and collaborators predicts that the lowermost dips form bald patches on a part of the PIL separating the parasitic polarity from the surrounding dominant flux. Therefore, the “ends” of the barbs are located at the PIL, and the field lines passing through the barb are not actually rooted in the parasitic polarity. The model agrees with recent observations of bald patches in the photospheric vector field in areas where filament barbs are located (López Ariste *et al.*, 2006). This means that the ends of the filament barbs would not be rooted directly in the photosphere as proposed by Wang (2001) and Lin *et al.* (2005a). The observations of magnetic dips are in contradiction with the idea of barbs rooted in parasitic polarities (Lin *et al.*, 2005a) and with the interpretation of the observed counter-streaming motions as plasma flows along fixed, inclined field lines (Zirker *et al.*, 1998a). More polarimetric observations should be done jointly with H α high spatial resolution observations of fine structures in quiescent filaments to distinguish between the different magnetic models for the barbs. For active filaments and dynamic fibrils the situation may be different, and the fine structures probably end in the dominant polarities (Lin *et al.*, 2008b).

Dudik *et al.* (2008) used THÉMIS/MTR observations of the photospheric vector field to construct a LMHS model of a filament. Figure 9 shows selected magnetic field lines and a comparison of the modeled dips with H α observations. The authors find significant departures from translational invariance along the PIL. They show that the flux rope is split into two parts: one part is rooted in a network element (P2) on the positive polarity side of the filament, while the other part is present along the full length of the computational domain. This shows that flux ropes can have a complex

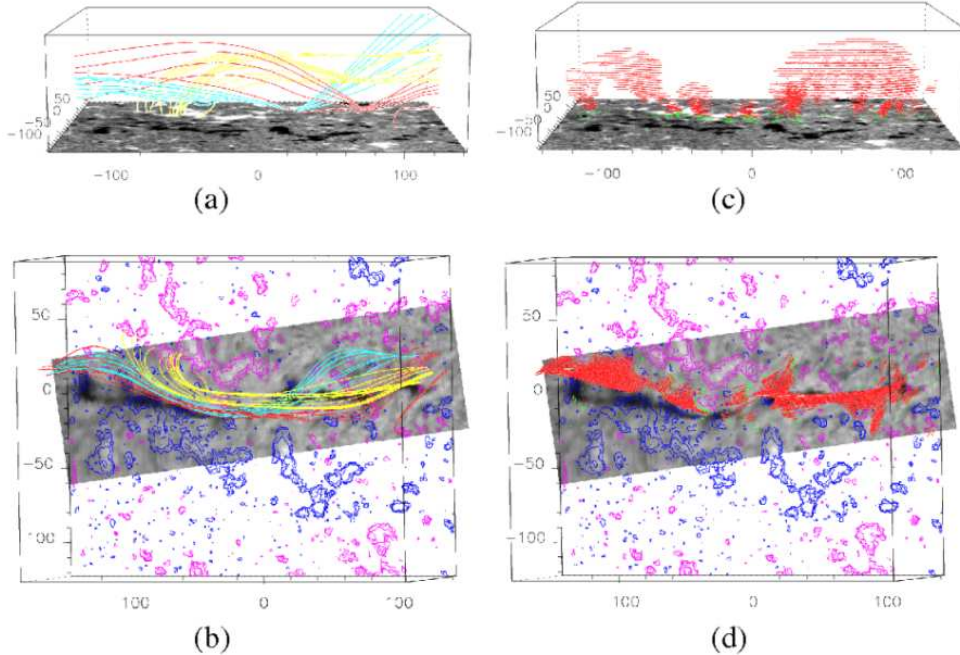


Fig. 9 Linear magneto-hydrostatic model of a filament observed with THÉMIS (Dudik *et al.*, 2008). The *left* panels show selected magnetic field lines as seen (a) from the side of the computational domain, (b) by an observer on Earth. The *yellow* field lines are rooted within the domain, while the *red* and *blue* lines pass through the left and right boundaries. The *right* panels show the locations of dips in the field lines as seen from the same perspectives. Each field line is plotted up to a height of 300 km above the dip to simulate the effect of the pressure scale height of the prominence plasma. All panels show the vertical magnetic field on the photosphere, either as a greyscale image (upper panels) or as *blue* and *purple* contours (lower panels). Panels (b) and (d) also show the co-aligned H α image from THÉMIS.

magnetic structure, and may consist of multiple strands that are twisted together. The axial magnetic flux may vary along the length of the filament.

2.2.5 Non-Linear Force-Free Field Models

Several authors have developed non-linear force-free field (NLFFF) models that include the local environment of the flux rope. This is important because the overlying coronal arcade plays a key role in the equilibrium and stability of the flux rope. For example, Régnier and Priest (2007) construct NLFFF models by “extrapolating” observed photospheric vector fields into the corona (also see Régnier *et al.*, 2002; Régnier and Amari, 2004; Régnier and Canfield, 2006; Canou *et al.*, 2009). They consider two active regions: one a decaying active region with strong currents (AR 8151), the other a newly emerged active region with weak currents (AR 8210). For the old decaying active region the connectivity and geometry of the NLFFF model include strong twist and strong shear, and are very different from the potential field model. The twisted flux bundles store magnetic energy and helicity high in the corona (about 50 Mm). The newly emerged region has a complex topology and the departure from a potential field

is small, but the excess magnetic energy is stored in the low corona and is enough to trigger powerful flares.

An alternative method for constructing NLFFF models of filaments was developed by van Ballegooijen (2004). The technique involves inserting a flux rope into a potential field based on an observed photospheric magnetogram, and then evolving the field in time to an equilibrium state using magneto-frictional relaxation. The advantage of this method is that the axial flux Φ_{axi} and poloidal flux F_{pol} of the flux rope can be specified, and these parameters can be varied until a good fit to the observations is obtained. If the axial and poloidal fluxes are not too large, the relaxation results in a NLFFF describing both the flux rope and its surroundings. The method was applied to a filament observed at the Swedish Vacuum Solar Telescope (SVST) in June 1998. This U-shaped filament had a prominent barb that exhibited interesting fine structure and internal motions. It was found that the dipped field lines in the NLFFF model reproduce some of the observed features of the filament barb, but not all. The barb is attributed to the presence of a magnetic element directly below the filament, so it is difficult to decide whether this element is “dominant” or “parasitic.”

Bobra *et al.* (2008) developed NLFFF models of two active regions using the above flux-rope insertion method. The models are constrained by H α observations of the filaments and by TRACE observations of coronal loops in the overlying corona. The best fit to the observations is obtained for a model in which the flux rope is only weakly twisted; the peak value of α occurs at the boundary between the flux rope and its surroundings, not at the flux rope axis. Bobra *et al.* find that the axial fluxes of the flux ropes are close to the upper limit for stability of the force-free equilibrium; however, no major eruptions occurred in these active regions either several days before or after these observations. This suggests that active regions can release magnetic free energy gradually, and that the build-up of free energy does not necessarily lead to large flares or coronal mass ejections. In contrast, Su *et al.* (2009) modeled a different active region and found that the flux rope present in that region has an axial flux that is well below the threshold for eruption. Clearly, observations of filaments can provide important constraints on the structure and stability of magnetic fields in active regions. For filaments between active regions and on the polar crown it is not known how close they are to the limit of stability.

In more recent modeling of NLFFFs, Mackay *et al.* (2009) consider how the structure of dips in a filament may vary as a single bipole polarity is advected towards the main body of the filament. The authors demonstrate how the bipole may result in the break up of the filament and a significant change in vertical extent of the dips. In contrast to linear force-free models they show that through considering a time-series of evolved non-linear force-free fields that barbs may form when either the minority or dominant polarity is advected towards the PIL.

In the previous discussion the observed structure and morphology of solar filaments has been discussed along with recent developments in constructing static 3D models of their magnetic structure. In the next section the review considers the origin of the mass within filaments, along with the properties of observed flows.

3 Plasma Structure and Dynamics

Although the Sun’s magnetic field clearly is the primary source of support and constraint for the prominence mass, the underlying physics governing the origin and sub-

sequent behavior of this material remains a lively topic of debate. The observed characteristics of prominence plasmas are discussed in depth in Paper I (sections 3 and 4) with a brief summary given below. The key observational constraints that must be satisfied by any successful plasma formation model are as follows:

1. Active region prominences tend to be shorter (of order 10 Mm), short-lived (minutes to hours), and lower (<10 Mm), while those formed outside active regions can be hundreds of Mm long, persist through multiple solar rotations, and extend as high as 100 Mm.
2. Prominence plasma is predominantly dynamic, exhibiting horizontal and/or vertical motions of order 10-70 km s⁻¹ (Kubota and Uesugi, 1986; Schmieder *et al.*, 1991; Zirker *et al.*, 1998a; Kucera *et al.*, 2003; Lin *et al.*, 2003; Okamoto *et al.*, 2007; Berger *et al.*, 2008; Chae *et al.*, 2008). Quiescent filaments can go through phases of enhanced internal motion and activity (Martin, 1973; Tandberg-Hanssen, 1995; Kucera *et al.*, 2006), altering the amount of cool material in the filament (Kilper *et al.*, 2009).
3. Prominence plasma frequently appears *in situ* high in the hot corona (McMath and Pettit, 1938; Schrijver, 2001), but also is observed flowing up from the chromosphere (Chae *et al.*, 2000; Liu *et al.*, 2005; Schwartz *et al.*, 2006).
4. Prominences appear to be composed of multiple knots and threads with widths down to the resolution limit (~100 km) and typical lengths of 3 - 20 Mm (Lin *et al.*, 2003, 2005a; Heinzel and Anzer, 2006; Gunár *et al.*, 2007, 2008; Berger *et al.*, 2008).
5. Barbs — lateral extensions from the prominence spine toward patches of parasitic polarity with vertical extents much greater than the local gravitational scale height — apparently are connected to the chromosphere (Kiepenheuer, 1953; Malherbe, 1989; Martin, 1998; Chae *et al.*, 2005).

As is discussed below, no single model can explain the entire complex range of characteristics at present.

It was recognized over 30 years ago that the large prominence mass must come from the chromosphere, because there is not enough plasma residing in the ambient corona (Pikel'ner, 1971; Saito and Tandberg-Hanssen, 1973; Zirker *et al.*, 1994). Sufficient mass to explain prominences must be extracted from the chromosphere, either through magnetic forces, which inject or lift cool plasma directly into the corona, or through thermal pressure forces, which evaporate heated plasma that subsequently condenses into prominence knots or threads. Here we summarize the current status of these models for the prominence plasma, and discuss one well-studied example of an evaporation-based mechanism — the thermal non-equilibrium model — in greater detail.

3.1 Injection Models

According to the injection models, cool plasma is forced upward in filament-channel flux tubes with sufficient force to reach the observed heights of prominence plasma. Most injection models (see Fig. 10) generally invoke reconnection low in the solar atmosphere as the pivotal cause of mass at prominence temperatures being expelled into the corona (Wang, 1999; Chae, 2001). This conjecture is largely motivated by the well-observed, but poorly understood, connection between flux cancellation and filament channel formation (van Ballegooijen and Martens, 1989; Martin, 1998; Wang and Muglach, 2007).

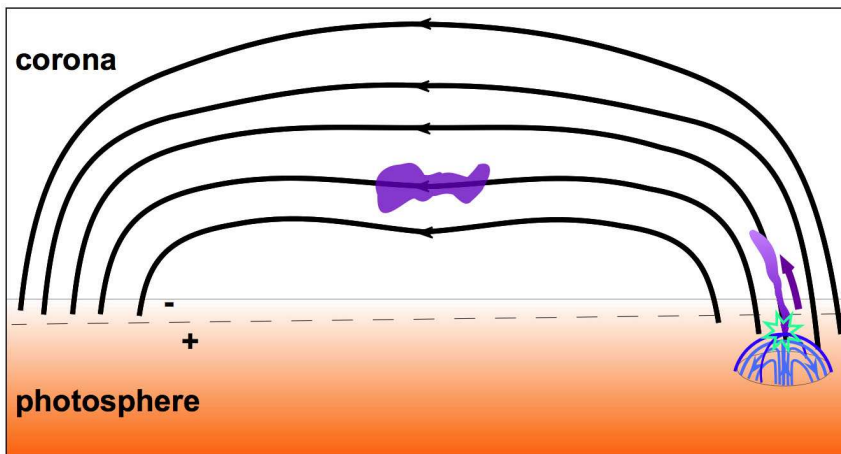


Fig. 10 Illustration of *injection* of prominence plasma (purple) by reconnection between minority-polarity bipole (blue lines) and preexisting filament-channel field (black lines). The polarity inversion line is dashed.

Because injection necessarily produces unidirectional flows in each flux tube, counter-streaming could arise either through reconnection occurring at the bases of different flux tubes on opposite sides of the PIL or through sequential reconnection at each foot-point. Some injection models propose that the reconnection sites are at the PIL (*e.g.*, Chae, 2003), while others suggest that the jets originate at minority-polarity intrusions offset from the PIL (*e.g.*, Wang, 1999). Many active-region prominences provide strong evidence for the type of jetting expected from reconnection events, and may well be explained by injection (Chae, 2003). However, active region prominences are short-lived, low-lying and highly variable, and are sufficiently distinct from quiet-Sun prominences that different physical mechanisms may be involved. Prominence barbs also might be explained by the injection of cool plasma by reconnection between the filament channel field and small bipoles emerging in the channel (Litvinenko, 2000; Wang, 2001; Chae *et al.*, 2005). Both large- and small-scale up-flows have been recorded in quiet-Sun hedge-row prominences (Zirker *et al.*, 1994; Berger *et al.*, 2008), although it is difficult to determine whether these flows originate at the photosphere due to spicules and other obscuring chromospheric activity. Recent high-resolution observations by SOT reveal strong jetting throughout the chromospheric network (de Pontieu *et al.*, 2007); it is possible that this activity occurs within filament channels on field lines capable of hosting prominence material.

On the other hand, it is unclear whether injection can account for all aspects of the observed dynamic evolution of quiet-Sun prominences, such as the frequency with which cool plasma appears suddenly in the corona and the predominantly horizontal, fine-scale counter-streaming flows. Furthermore, the extent to which reconnection can drive cool filament-channel material as high as 100 Mm in the corona, without also heating this plasma, has not been demonstrated in a realistic three-dimensional (3D) geometry with applicable energy sources and sinks. In simulations of Yohkoh X-ray jets by Yokoyama and Shibata (1995), reconnection produces hot jets directly, while the associated (but not co-spatial) cool jets are produced by compression of nearby open field. A similar mechanism might explain the association between flux cancel-

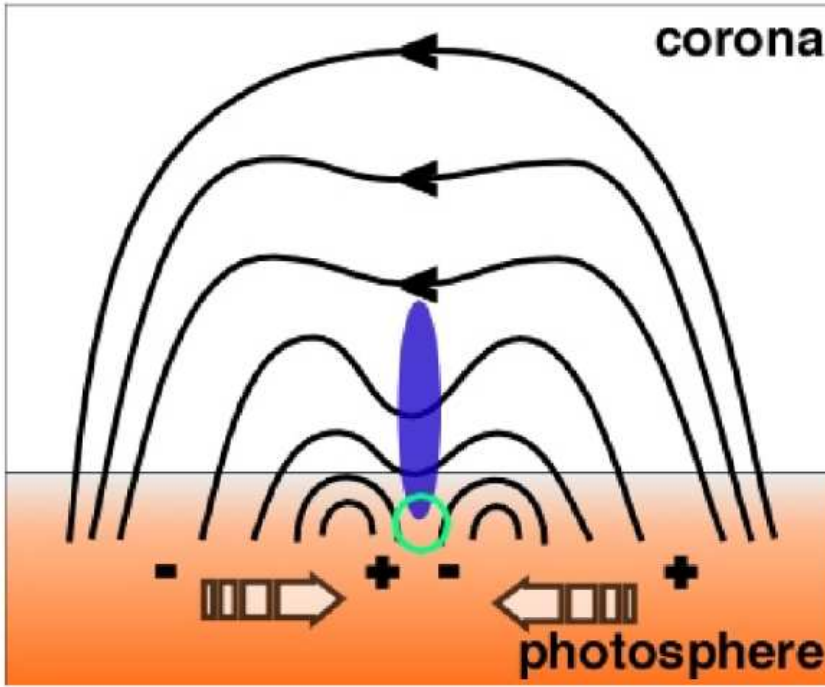


Fig. 11 Illustration of *levitation* of prominence plasma (purple) by U-loop emergence or post-reconnection relaxation associated with flux cancellation.

lation and injection of cool plasma. Another unresolved issue is whether cancellation reconnection preferentially occurs in or below the chromosphere; if the interacting flux systems reconnect instead in the low corona (see below), then cool, dense plasma will not be lifted or injected directly. As is well-known, the fact that cancellation is observed in the photosphere or chromosphere does not necessarily indicate that the associated reconnection site is at the same level (Zwaan, 1987; Harvey *et al.*, 1999). The temperature minimum is thought by some to be the most favorable location for reconnection, because the Spitzer resistivity is highest there (Roumeliotis and Moore, 1993; Sturrock, 1999; Litvinenko *et al.*, 2007) or because of enhanced plasma turbulence (Chae *et al.*, 2002). In summary, the essential distinguishing features predicted by the injection model are that photospheric or chromospheric mass is injected with substantial speed at locations of flux cancellation/reconnection, either at or away from the PIL, and that this mass rises into the corona at or near its original cool temperature.

3.2 Levitation Models

Levitation models propose that cool plasma is lifted by rising magnetic fields at the PIL and transported transverse to the magnetic field (see Fig. 11). In one class of levitation models, the filament-channel magnetic structure is a highly twisted flux rope that brings up cool plasma as the axis and lower portions of the rope emerge above the photosphere; thus, the prominence plasma should reside in the upward concavities

of the helical field (Rust and Kumar, 1994). However, such concave-upward formations have been observed only rarely in non-erupting prominences (see, *e.g.*, Lites, 2005; López Ariste *et al.*, 2006; Okamoto *et al.*, 2007). An alternative lifting mechanism is the relaxation of magnetic fields during emergence of U loops (Deng *et al.*, 2000) or after reconnection associated with flux cancellation (van Ballegooijen and Martens, 1989; Priest *et al.*, 1996; Oliver *et al.*, 1999; Litvinenko and Martin, 1999; Galsgaard and Longbottom, 1999; Litvinenko and Wheatland, 2005; Welsch *et al.*, 2005). Simulations of the reconnection-levitation mechanism have verified that rising field lines are indeed produced by reconnection between bipolar systems, but significant work remains to prove that this mechanism is responsible for the observed motions and properties of prominence plasma. Detailed calculations of reconnecting dipoles (Galsgaard and Longbottom, 1999; von Rekowski and Hood, 2008) predict significantly different plasma properties, depending on the dimensionality, the initial conditions, and the terms included in the energy equation. For example, Galsgaard and Longbottom (1999) found a 20% density contrast between the elevated material and the background corona, much less than the 2 orders of magnitude deduced from prominence observations, whereas von Rekowski and Hood (2008) predict that the uplifted plasma can exhibit X-ray-emitting coronal characteristics, filament-like photospheric properties, or a mixture of both (note, however, that the latter model is intended primarily to explain coronal bright points). The difference between the two results is that Galsgaard and Longbottom (1999) due to computational reasons only considered a simple hydrostatic atmosphere with a uniform temperature profile and did not include a transition region. One common result is that most of the uplifted cool plasma drains along the rising field lines onto the chromosphere. Quiet-Sun prominences that resemble a central pillar from which cool material streams outward and downward are the best candidates for supporting this scenario. The extent to which this process can lift photospheric or chromospheric material as high as 100 Mm into the corona also has not been demonstrated. To date, none of these levitation models has allowed flux to retract beneath the photosphere during reconnection, thus preferentially favoring upward motions. Flux emergence simulations have shown that emerging U-loops and the associated photospheric plasma do not readily break through the photosphere nor rise to coronal heights characteristic of quiet-Sun and intermediate prominences, even without the inhibiting presence of a preexisting coronal field (Fan, 2001; Archontis *et al.*, 2004; Manchester *et al.*, 2004; Magara, 2006; Galsgaard *et al.*, 2007; Magara *et al.*, 2008; Archontis and Török, 2008). Although the U-loops of the emerging tube do not rise to coronal heights, the process of flux emergence may still produce a coronal flux rope with dips. A flux rope may form through the reconfiguration of emerged sheared field lines that lie above the emerging tubes axis. The flux rope may be formed either by magnetic reconnection (Manchester *et al.*, 2004; Magara, 2006; Archontis and Török, 2008) or through helicity injection by torsional Alfvén waves (Fan, 2009). Once the tube is formed above the photosphere, it may rise to coronal heights, in principle dragging cool photospheric or chromospheric plasma with it. Such a process acting during flux emergence, is unlikely to explain quiescent or intermediate prominences but would be of importance to active region prominences. This will be further discussed in Section 5.6. One effect not considered thus far in 3D flux-emergence calculations, the partial ionization of portions of the chromosphere and photosphere, might enable more rapid emergence as well as the emergence of more flux (and frozen-in plasma) into the corona (Leake and Arber, 2006). As discussed above for the injection models, it is unclear where reconnection between such flux systems would occur in the solar atmosphere; for example, the reconnection in the Galsgaard and Longbottom

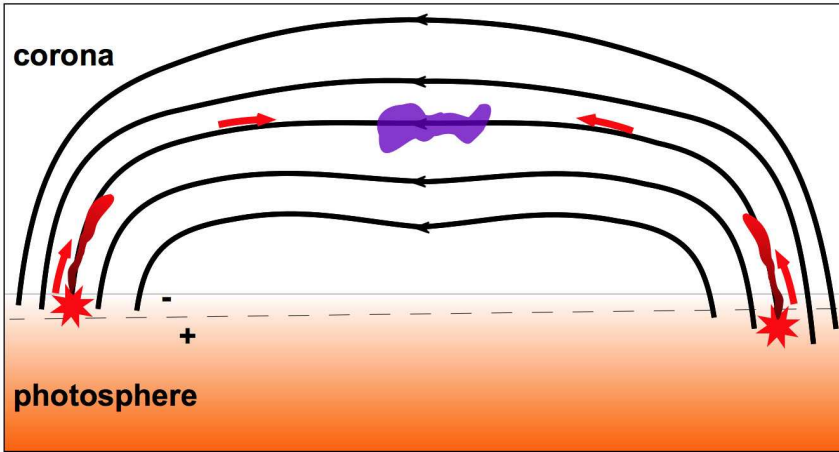


Fig. 12 Illustration of an *evaporation-condensation* model: hot up-flows (red) driven by heating localized above the footpoints evaporate chromospheric plasma that ultimately condenses in the corona as cool prominence material (purple).

(1999) study begins in the corona, at the apex of a null-null separator, so the bulk of the mass lifted at that location is coronal. An alternative mechanism proposed to lift and support prominence plasma in the corona is upward-propagating, weakly damped MHD waves (Peceli and Engvold, 2000); recent observational evidence for significant Alfvénic perturbations in chromospheric structures (de Pontieu *et al.*, 2007) makes this an intriguing suggestion, but further quantitative work is needed to evaluate this mechanism rigorously. In general, the key features of levitation models overlap significantly with those of injection models (see above); however, the levitated mass does not travel as far or as fast as injected mass would, and typically is predicted to be located above the PIL.

3.3 Evaporation-Condensation Models

Evaporation-condensation models are based on the fact that adding heat to a coronal loop increases the density of the corona while decreasing slightly the chromospheric mass (Fig. 12). Different temporal combinations of heating and cooling were studied, without successfully reproducing the basic properties of a prominence (Engvold and Jensen, 1977; An, 1985; Poland and Mariska, 1986). Subsequent research found that concentrating coronal heating near the footpoints of a loop should produce a cool condensation at or near the apex (Serio *et al.*, 1981; Mok *et al.*, 1990; Antiochos and Klimchuk, 1991; Dahlburg *et al.*, 1998). Although recent analysis of TRACE observations of some coronal loops independently indicated that the heating is concentrated near the loop footpoints (Aschwanden *et al.*, 2001; Winebarger *et al.*, 2002), the observational evidence for the spatial distribution of coronal heating is inconclusive at best. Confirmation of the basic principle behind this evaporation-condensation model for prominence plasma formation required the use of adaptive-mesh numerical simulations, to handle the rapid birth and subsequent evolution of a new, thin transition region at each interface between the loop and the cool condensation (Antiochos *et al.*, 1999). The

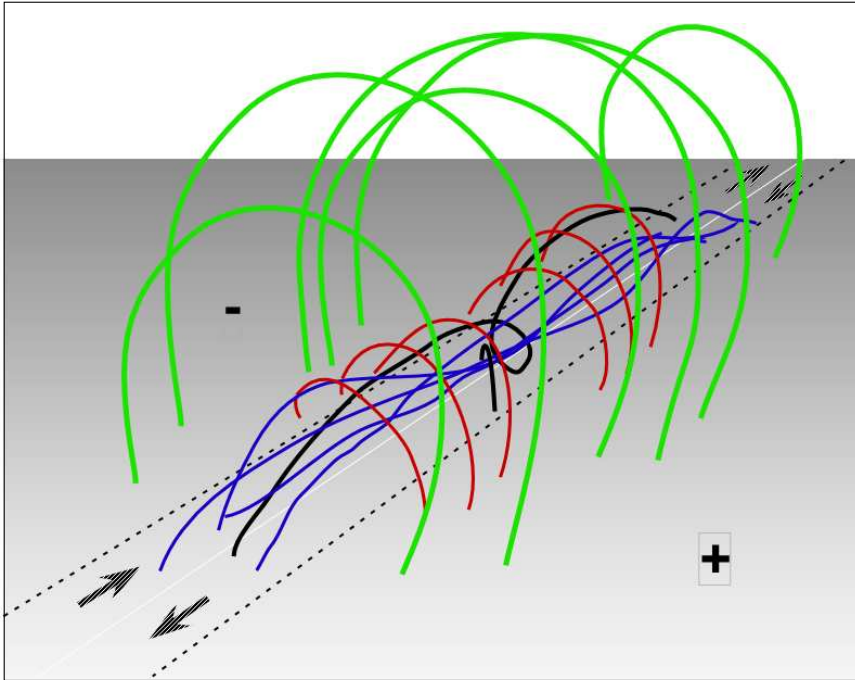


Fig. 13 Prominence locations predicted by the thermal non-equilibrium model, assuming that the filament-channel magnetic structure is a sheared arcade. The white line on the grey photosphere is the PIL, and the boundaries of the surrounding filament channel are denoted by dashed lines. Only the *blue* field lines match the requirements for thermal non-equilibrium to produce dynamic and stationary condensations consistent with observed prominence structure.

central concept of this model is that, if the heating scale λ is small compared to the length of a coronal loop and localized near the chromospheric footpoints, then the plasma in the midsection of the tube, where the heating is negligible, must undergo a radiatively-driven thermal collapse to low temperatures. A runaway situation develops in the coronal plasma because the radiative losses increase with decreasing temperature T for $T \geq 10^5$ K as well as with the square of the density: once the local plasma has cooled to this critical transition-region temperature, it must cool all the way to chromospheric temperatures to regain equilibrium (Hood & Anzer, 1988). The ratio of the heating scale to the loop length is a crucial factor because the total radiative losses from the loop increase linearly with length, but the thermal conduction and other energy transport or loss terms either decrease or remain constant with loop length. Clearly, the radiative losses will dominate for lengths above a threshold value that is approximately an order of magnitude greater than the heating scale (Mok *et al.*, 1990). As discussed in section 2.2, the magnetic structure containing the quiet-Sun prominence material is most likely to be a sheared arcade (Martin and Echols, 1994; DeVore and Antiochos, 2000) or weakly twisted flux rope (Martens and Zwaan, 2001; Bobra *et al.*, 2008), in which many of the loops nearly aligned with the PIL are much longer than typical coronal loops. Therefore, for a given heating scale, condensations are more likely to form in these elongated loops than in shorter loops rooted outside the filament channel (see Fig. 13).

A series of computational investigations of this evaporation-condensation process, denoted *thermal non-equilibrium*, has systematically explored the dynamics and energetics of the plasma within individual elongated flux tubes heated near the footpoints (Antiochos *et al.*, 1999, 2000; Karpen *et al.*, 2001, 2003, 2005, 2006; Karpen & Antiochos, 2008). While the nature of the footpoint heating is not well understood, this work has established constraints on the conditions favorable to condensation formation, the magnetic structure of prominences, and the nature of the associated coronal heating. The key factors in determining the likelihood and behavior of condensations are the flux tube geometry and the localized heating properties. In long, low-lying flux tubes with shallow arches or dips, unequal quasi-steady heating yields a repetitive cycle of condensation formation, motion along the tube, and destruction by falling onto the nearest chromosphere (Antiochos *et al.*, 2000; Karpen *et al.*, 2001, 2006). It is important to note that this process does not require the presence of dipped flux tubes, in contrast to the assumptions of many magnetic-structure models (*e.g.*, Anzer and Heinzel, 2003), although shallow dips facilitate the collection and retention of cool plasma. On the other hand, if the host flux tube has a deep dip, as would occur in the outer portions of a highly twisted flux rope, thermal non-equilibrium produces condensations that rapidly fall to the lowest part of the dip and remain there, stationary but growing as long as the heating remains quasi-steady (Karpen *et al.*, 2003, 2005). Condensations also form when the energy input is impulsive in nature and randomly distributed in time, as in nanoflare models of coronal heating (Klimchuk, 2006), so long as the average interval between energy bursts is shorter than the radiative loss time in the ambient corona (Karpen & Antiochos, 2008). The calculated condensation speeds, counter-streaming, lifetimes, and sizes are consistent with observations of many quiet-Sun prominences. However, this model does not provide a satisfactory explanation of active-region prominences, which are too short to support the thermal non-equilibrium process with typical values of the heating scale, or of the vertical structure and dynamics of hedge-row prominences. Barbs could be consistent with thermal non-equilibrium if they are composed of vertically aligned dips in otherwise horizontal flux tubes (Heinzel and Anzer, 2001), as long as the dips are deep enough to trap the condensed matter: for example, in photospheric “bald patches” near parasitic polarity sites (Aulanier *et al.*, 1998; Aulanier and Schmieder, 2002; van Ballegooijen, 2004; López Ariste *et al.*, 2006).

This process could occur in any favorable magnetic structure, but thus far has been considered systematically only within the context of the sheared arcade model (section 2.2). The color coding in Fig. 13 illustrates the implications of the thermal non-equilibrium studies summarized above for the location and evolution of prominence material within a filament channel formed by the sheared arcade mechanism. Only the blue field lines match the requirements for thermal non-equilibrium to produce dynamic and stationary condensations consistent with observed prominence structure. Red field lines are too short; the helical black field line can host only a condensation sitting at the bottom of the dip; and green field lines are capable of hosting small, intermittent, short-lived condensations known as coronal rain (Müller *et al.*, 2003, 2005). Three-dimensional MHD simulations of both the magnetic and the plasma structure with localized heating, radiation, and thermal conduction are needed to determine the full scope and applicability of thermal non-equilibrium to solar prominence plasmas. For a discussion of energy balance considerations in solar prominences see section 10 of Paper I. Evaporation-condensation models, as represented by thermal non-equilibrium, uniquely predict both stationary and highly dynamic prominence threads that condense *in situ* in the corona and trace the supporting flux tubes; an increase in coronal density

precedes each condensation episode, while the collapse of the condensations reduces the ambient coronal density and generates waves and shocks.

As discussed above, flows are commonly observed in solar filaments and prominences. In addition to this a wide variety of oscillations are observed. The properties of these oscillations, along with theoretical models used to describe them is now discussed.

4 Magneto-hydrodynamic Waves in Solar Prominences

4.1 Overview

Theoretical studies of small-amplitude oscillations and MHD waves in the solar corona started long before clear observational evidence about the presence of these phenomena in the solar corona was available. The interest of their study lies in their potential relationship with the coronal heating problem and with the possibility to perform local seismology of the solar corona. Thanks to ground- and space-based observations, evidence about the presence of oscillations in coronal structures (loops, prominences, plumes, etc) is now widely available.

Solar prominences are subject to various types of oscillatory motion (section 4, Paper I). In the early days of filament observations, all the data collected on oscillations were related with motions induced by disturbances coming from a nearby flare (*e.g.*, Ramsey and Smith, 1966). These disturbances produce large-amplitude oscillations with velocity amplitudes of 20 km s^{-1} or higher. Observations of large-amplitude oscillations in filaments are rare, although in recent years with the help of new observational capabilities more detections have been reported (Eto *et al.*, 2002; Okamoto *et al.*, 2004; Jing *et al.*, 2003, 2006; Gilbert *et al.*, 2008). Also, theoretical modeling of such events is lacking. On the other hand, from observations performed with ground-based telescopes it is well known that most quiescent prominences and filaments display small-amplitude oscillations. The motions are mainly detected through the periodic Doppler shifts of spectral lines (*e.g.*, Tsubaki, 1988), and the observations have shown that (1) the oscillations are of local nature; (2) simultaneously flowing and oscillating features are present; (3) the oscillations seem to be strongly damped in time, and (4) there are spatially coherent oscillations over large regions of prominences/filaments. A key aspect of prominence oscillations is the knowledge of its triggering mechanisms. While for large-amplitude oscillations they are well known, in the case of small-amplitude oscillations, the excitation process still remains a mystery, in spite of the available observational information.

In this section, we will focus on small-amplitude oscillations in prominences, which can be interpreted as linear magneto-hydrodynamic (MHD) waves, and which constitute an important tool for understanding the physical properties (sections 2 and 3 of Paper I) and the internal structure of prominences. Traditionally, the study of prominence oscillations has been based in the determination of the normal modes of oscillation of different equilibrium configurations, such as slabs or cylindrical flux tubes, without including any dissipative mechanism. Recently, the study of the damping of prominence oscillations has been the subject of intense theoretical modeling by considering different dissipative mechanisms. Prominence seismology seeks to obtain information about prominence physical conditions from a comparison between observations and theoretical models of oscillations. Attempts to determine the Alfvén speed, the magnetic field, the shear angle, etc. have already been carried out. In the following

we first provide a summary of the observations of prominence oscillations, and then discuss various aspects of the theoretical modeling.

4.2 Observational Background

4.2.1 *Ground-Based Observations*

Prominences above the limb exhibit oscillations with velocity amplitudes in the range 2 to 10 km s^{-1} . The oscillations appear to be local in nature, disturbing only some regions of prominences. Most information about this type of oscillation has been obtained from Doppler velocity data, although there are also detections coming from other spectral indicators such as line intensity and line width (section 2.1 and 3.4, Paper I). Only rarely are the oscillations detected in several of these spectral indicators at the same time and with the same period, which constitutes one of the puzzling features of prominence oscillations. Earlier, the first observational detections of oscillations using one-dimensional spectroscopic observations led to a classification in terms of short- and long-period oscillations. However, when the number of available observations increased, it was clear that a wide range of periods, between 1 and 90 minutes, were present. Detailed information on the oscillatory periods detected in limb prominences is available in Tsubaki (1988), Oliver (1999) and Oliver and Ballester (2002). Although the classification in terms of short- and long-period oscillations is still in use, it does not cast any light nor gives any help with regard to the nature, origin or exciter of oscillations.

On the other hand, far more interesting results can be obtained from two-dimensional, high-resolution observations of prominences (Molowny-Horas *et al.*, 1999; Terradas *et al.*, 2002) which allow the construction of maps of the Doppler velocity, wave period, damping time and wave vector, and the extraction of interesting information about oscillations in prominences. For instance, Terradas *et al.* (2002) reported the existence of large regions with periodic Doppler (line of sight) velocity oscillations having similar periods, around 75 minutes, noticing also that the oscillatory amplitude tends to decrease in time in such a way that the periodicity totally disappears after a few periods. Reliable values for the damping time, τ_D , have been derived from different Doppler velocity time series by Molowny-Horas *et al.* (1999) and Terradas *et al.* (2002). The values of τ_D thus obtained are usually between 1 and 4 times the corresponding period, and large regions of the prominence display similar damping times. Also, Terradas *et al.* (2002) reported the presence, along two selected paths in the prominence region, of plane propagating waves as well as a standing wave. The plane waves propagate in opposite directions with wavelengths of 67,500 and 50,000 km and phase speeds of 15 km s^{-1} and 12 km s^{-1} , respectively, while in the case of the standing wave the estimated wavelength is 44,000 km and a phase speed is 12 km s^{-1} . Furthermore, the analysis has identified the existence of a wave generating region, indicating that oscillations are locally excited.

For the case of filaments on the disk, old two-dimensional observations of filament oscillations (Thompson and Schmieder, 1991; Yi and Engvold, 1991; Yi *et al.*, 1991) reveal that the Doppler signals of filaments form fibril-like structures. Yi *et al.* (1991) concluded that the fibrils form an angle of about 25° with the filament long axis, that individual fibrils or groups of fibrils may oscillate independently with their own periods, and that these fibril structures represent mass motions in magnetic flux tubes. Thanks to the improvement in spatial resolution provided by modern solar telescopes, high-

Table 1 Periods detected in prominence fine structure oscillations.

Reference	Period (min)
Thompson and Schmieder (1991)	4.4
Yi, Engvold, and Keil (1991)	5.3, 8.6, 15.8
Lin (2004)	26
Lin et al. (2007)	3 - 9

resolution observations have given us key information about the internal structure and features of filaments, which is useful for the study of filament oscillations. For instance, observations of filaments made by Lin *et al.* (2005a,b) suggest that the thickness of thin threads forming the filaments is ≤ 250 km, that only a small portion of filament threads are filled with cool plasma, and that this absorbing plasma is continuously flowing along the thread structure with velocities 15 ± 10 km s $^{-1}$. Lin (2004) analyzed the Doppler signals obtained from two different regions of a polar crown filament, showing the presence of oscillation that are coherent over each observed region (size about 25 Mm) and are strongly damped after a few periods. Furthermore, in the middle part of the filament 49 H α moving features display periodic variations in Doppler velocity. Finally, Lin *et al.* (2007) have found evidence for traveling waves in the threaded structure of a filament and, in some cases it seems that the propagating waves move in the same direction as mass flows. They also have determined the wavelength of a propagating wave, obtaining a value of around 3,000 km. In Table 1 the periods found from ground based observations are summarized.

4.2.2 Space-Based Observations

Prominence oscillations have also been observed with space-based instruments. Blanco *et al.* (1999) used SUMER to study the behavior of different lines of Si IV and O IV in a limb prominence. The results show that a large amount of energy is contained in oscillations with periods between one and six minutes, corresponding to characteristic periods of the chromosphere and photosphere. Furthermore, for all the considered wavelengths, the energy versus the slit position varies in such a way that minima and maxima for each wavelength are coincident. Later on, oscillations in an active-region filament were reported by Régnier *et al.* (2001). Using SUMER they observed the He I line, obtaining a time series of the filament with a duration of 7 h 30 min and with a temporal resolution of 30 s. A Doppler velocity time series was derived, and by Fourier analysis significant power was found at periods between 5 and 65 min suggesting the presence of oscillations. Foulon *et al.* (2004) used SoHO/EIT 195 Å with a time cadence of 12 min to observe an EUV filament during its crossing of the solar disk. They reported intensity variations of long period, 8 - 27 h, with a dominant period of about 12.1 h, while the amplitude of the intensity variations reached 10% of the background intensity. Furthermore, the periodic intensity variations seem to be correlated along the filament, and the most pronounced oscillations were detected during 6 days. Pouget *et al.* (2006) used SoHO/CDS to observe two filaments, during different days, in the optically thick He I line (section 8.2, Paper I). The duration of the observations was 15 - 16 h with a time resolution of 20 s. Before performing the Fourier analysis of Doppler velocities, the mean velocity averaged over the width of the filament was computed and the obtained power spectrum points out the existence of a wide range of periods arriving up to 5 - 6 h. The results derived from these observations must be taken with care. First,

Table 2 Periods detected from space-based observations of prominence oscillations.

Reference	Period (min)
Blanco et al. (1999)	1 - 6
Régnier et al. (2001)	5 - 65
Foullon et al. (2004)	720
Pouget et al. (2006)	up to 360
Okamoto et al. (2007)	2 - 4.5
Berger et al. (2008)	20 - 40
Ning et al. (2009)	3.5 - 6

it should be noted that the He I line may be formed either by a 20,000K plasma or by scattering in a cooler 8,000K plasma. Therefore the emission may originate in the outer parts of the prominence, whereas the authors assume that the detected motions are propagated from the prominence core. Moreover, the averaging of Doppler signals coming from each pixel means that spatial information is lost and, furthermore, it is difficult to be sure that the same region of the filament is tracked when long-time observations are performed, and that there is no time evolution of the filament (brightenings, fadings, small eruptions, etc). Recently, Okamoto *et al.* (2007) using SOT and the Ca II H line have obtained about 1 h of continuous images of an active region. The Ca II H line movie shows continuous horizontal motions along the prominence. Some of the flows display constant velocities while others accelerate. Hinode movies also show that the threads suffer synchronous vertical oscillatory motions. Finally, recent high-resolution (0.2'') observations of limb prominences made by SOT (Berger *et al.*, 2008) reveal very complex dynamics with vertical filamentary down-flows and vortices, as well as episodic, vertical up-flows. Furthermore, using horizontal time slices taken at different heights within the prominence, they suggest the presence of large-scale oscillations with periods between 20 and 40 minutes, lasting one or two periods, and with a vertical phase speed of 10 km s^{-1} . Finally, Ning *et al.* (2009) have analysed the oscillatory behaviour of a quiescent prominence observed with Hinode. They find that prominence threads exhibit vertical and horizontal oscillatory motions. In some parts of the prominence, the threads seem to oscillate independently of each other, and the oscillations seem to be strongly damped. The periods reported are very short, with the dominant one appearing at 5 minutes. The range of periods determined from space based observations are summarised in Table 2.

In summary, from the available observational information some characteristic features of prominence oscillations can be highlighted: The oscillations only affect parts of the prominence, and in the case of filaments are confined to the thread structure. The presence of simultaneously flowing and oscillating features is a common feature. The oscillations seem to be strongly damped in time. There are spatially coherent oscillations over large regions of prominences and filaments. More detailed information about observations of small amplitude oscillations in filaments and prominences can be found in Engvold (2001, 2004, 2008), Oliver and Ballester (2002), and Banerjee *et al.* (2007).

4.3 Theory of Small-Amplitude Oscillations in Prominences

Theoretical interpretations of prominence oscillations are mostly based on linear MHD waves. An important ingredient in the modeling of MHD waves in prominences is the

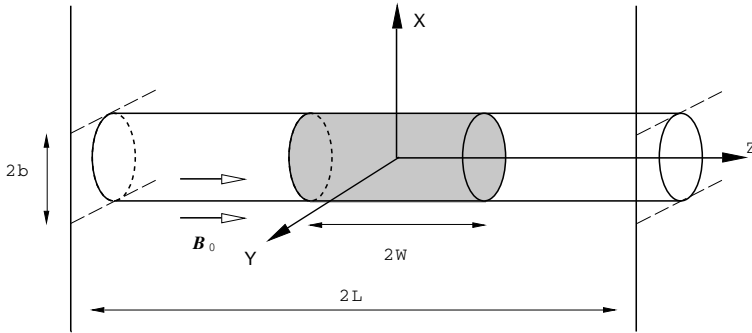


Fig. 14 Sketch of the equilibrium configuration for a cylindrical model of a prominence thread. The grey zone represents the cold part of the loop, *i.e.*, the prominence. The density in the prominence region is ρ_p , in the evacuated (coronal) part of the loop, ρ_e , and in the coronal environment, ρ_c . The magnetic field is uniform and parallel to the z -axis, and the whole configuration is invariant in the φ -direction. Adapted from Díaz *et al.* (2002).

chosen equilibrium configuration. In the past, slab models were used as a representation of limb prominences. However, due to present day high-resolution observations, models now pay more attention to equilibria based on thin cartesian or cylindrical threads. These threads represent thin magnetic flux tubes, partially filled with cold plasma. Such structures seem to be the building blocks of filaments when observed on the disc. Furthermore, attempts have been also made to reproduce the observed damping of prominence oscillations. The damping involves various thermal and non-thermal mechanisms. The thermal processes include damping due to optically thin radiative losses (section 8.1 and 10 of Paper I) and thermal conduction. The non-thermal processes include ion-neutral collisions in a partially ionized plasma (section 2.3, Paper I) and resonant absorption of wave energy in the inhomogeneous prominence plasma. In the following we first consider undamped, adiabatic MHD waves in prominence fine structures, and then discuss various damping mechanisms. Flows seem to be a characteristic feature of prominences (see section 3), and the combined influence of flows and non-adiabatic waves on oscillations will be considered in section 4.3.5.

4.3.1 Adiabatic MHD Waves in Prominence Fine Structures

Cylindrical geometry seems to be the most suitable to model prominence threads. Díaz *et al.* (2002) considered a straight cylindrical flux tube with a cool region representing the prominence thread, which is confined by two symmetric hot regions (Fig. 14). In this case, the fundamental sausage mode ($m = 0$) and its harmonics are always leaky. However, for all other modes ($m > 0$), at least the fundamental mode lies below the cut-off frequency. Regarding the spatial structure of perturbations, in cylindrical geometry the modes are always confined in the dense part of the flux tube. Therefore, an oscillating cylindrical fibril is less likely to induce oscillations in its neighboring fibrils, unless they are very close.

Díaz *et al.* (2005) studied multithread systems in Cartesian geometry. In this case the equilibrium configuration consists of a collection of threads separated by a distance $2c$ (see Fig. 15), and the individual threads are modeled as slabs (Díaz *et al.*, 2001). Following this approach, inhomogeneous filaments were constructed with different thread

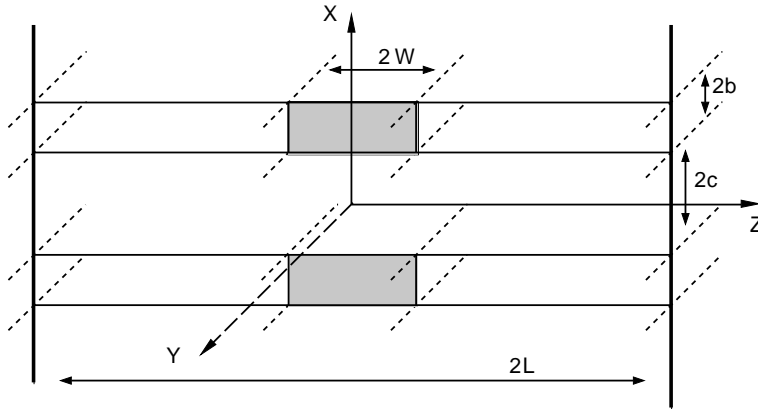


Fig. 15 Sketch of the equilibrium configuration for a collection of fibrils. The grey zone represents the cold part of the loop, *i.e.*, the prominence. The density in the prominence region is ρ_p , in the evacuated (coronal) part of the loop, ρ_e , and in the coronal environment, ρ_c . The magnetic field is uniform and parallel to the z -axis, and the whole configuration is invariant in the y -direction. Adapted from Díaz *et al.* (2005).

density ratios representing the inhomogeneity in density of a real prominence, and the separation between threads has been chosen randomly within the realistic range. When the separation between threads is small, there is a strong interaction between them since the perturbation can easily overcome the separation. As a result, only one even non-leaky mode can cause all the threads to oscillate in phase. The dependence of the oscillation frequency on the thread separation c can be studied: in the limit $c \rightarrow \infty$, the structure and the frequencies of each thread oscillating alone are recovered, while for small values of c only the mode described before remains having a slightly smaller frequency than in the case of the single dominant thread mode. Therefore, for realistic values of the separation between threads, the multithread system would oscillate in phase, with similar amplitudes and the same frequency. These results, although derived in Cartesian geometry, strongly agree with the observations of filament thread oscillations reported by Lin *et al.* (2005a). However, in the case of cylindrical geometry, the spatial structure of perturbations indicates that the modes are always confined to the dense part of the flux tube. Therefore, an oscillating cylindrical fibril is less likely to induce oscillations in its neighboring fibrils, unless they are very close.

4.3.2 Thermal Damping Mechanisms

Soler *et al.* (2008a) studied the oscillatory modes of an equilibrium configuration representing a prominence thread (Fig. 16) which is made of a homogeneous plasma layer with prominence conditions embedded in an unbounded corona. Thermal conduction parallel to the magnetic field, optically thin radiative losses, and heating have been considered as non-ideal, damping mechanisms. Figure 17 shows the period P , the damping time τ_D , and their ratio, versus the longitudinal wavenumber, for the fundamental kink modes. Taking into account the results in the range of wavelengths typically observed in prominences, we observe that the internal slow mode (responsible for longitudinal motions) produces periods compatible with intermediate- and large-period oscillations,

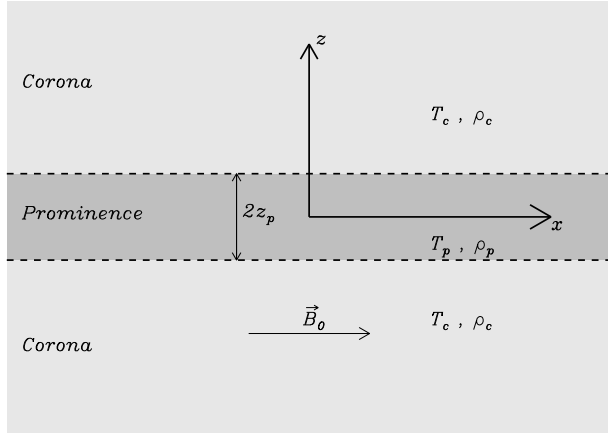


Fig. 16 Sketch of the equilibrium configuration for studying the damping of prominence oscillations in a single thread. Adapted from Soler *et al.* (2008a).

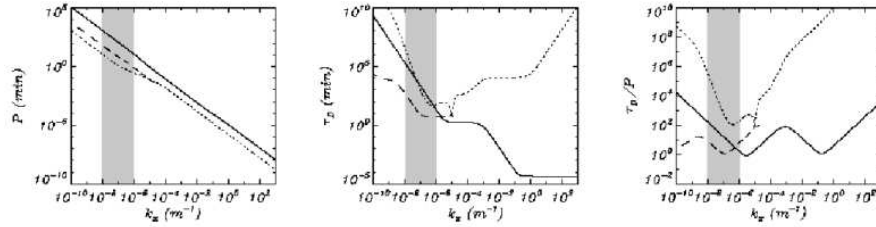


Fig. 17 Period (left), damping time (center) and ratio of the damping time to the period (right) versus the longitudinal wavenumber for the fundamental kink oscillatory modes: internal slow (solid line), fast (dotted line) and external slow (dashed line). The shaded zones correspond to those wavelengths typically observed in prominence oscillations. Adapted from Soler *et al.* (2008a).

whereas the fast mode (responsible for transverse motions) could be associated with short-period oscillations. On the other hand, the external slow mode mainly disturbs the surrounding corona, the amplitude of its motions within the prominence fibril being very small; hence it could be rather difficult to observe. Regarding the damping time, both internal and external slow modes are efficiency attenuated, with damping times of the order of their periods. However, again, the fast wave is much less attenuated since its damping time is between 2 and 6 orders of magnitude larger than its period.

In order to assess the relative importance of each non-adiabatic damping mechanism, a comparison was made between the damping time obtained when considering all non-adiabatic effects (displayed in the middle column of Fig. 17) and the results obtained when a specific mechanism is removed. The results of these computations suggest that (1) the internal slow mode is only affected by prominence-related mechanisms, radiative losses from the prominence plasma being responsible for the attenuation of this solution in the range of typically observed wavelengths; (2) the prominence thermal conduction is only efficient for very small wavelengths outside the observed range; (3) the fast mode is affected by both prominence and coronal mechanisms; (4) the damping of the external slow mode is entirely governed by coronal-related damping mechanisms,

mainly the coronal thermal conduction, which is the dominant mechanism in the range of typically observed wavelengths.

4.3.3 Damping of MHD Waves in a Partially Ionized Prominence Plasma

Prominences are partially ionized plasmas since hydrogen lines are observed (section 8.1 and 2.3 of Paper I). This fact was already considered by Mercier and Heyvaerts (1977) when they studied, from a theoretical point of view, the diffusion of neutral atoms due to gravity. A few years ago, Gilbert *et al.* (2002) studied the diffusion of neutral atoms in a partially ionized prominence plasma, concluding that the loss time scale is much longer for hydrogen than for helium. Recently, Gilbert *et al.* (2007) have investigated the temporal and spatial variations of the relative abundance of helium with respect to hydrogen in a sample of filaments. They have found that a majority of filaments show a deficit of helium in the top part while in the bottom part there is an excess. This seems to be due to the large loss time scale for neutral helium with respect to neutral hydrogen.

The consideration of prominence plasmas as partially ionized is extremely important for the physics of prominences, and the effects on MHD waves in prominences need to be taken into account. In particular, the frictional damping of magneto-acoustic waves in a partially ionized plasma is much stronger than in a fully ionized plasma because the presence of neutrals causes the Joule dissipation to increase as a result of electron-neutral and ion-neutral collisions (Khodachenko *et al.*, 2004). A comparative study of the role of ion-neutral damping of MHD waves and their damping due to viscosity and thermal conductivity was made by Khodachenko *et al.* (2004, 2006), finding that collisional damping is dominant.

The effects of partial ionization on fast and slow waves in an unbounded prominence plasma have been studied by Forteza *et al.* (2007). They have considered a partially ionized hydrogen plasma but have not included the effects of particle ionization and recombination, and they have assumed a strong thermal coupling between the species, so that electrons, ions, and neutrals have the same temperature ($T_e = T_i = T_n = T$). The separate governing equations for the three species can be easily substituted by a set of one-fluid equations for the whole partially ionized plasma, where isotropic pressure has been assumed and gravity, viscosity, heat conduction, and non-adiabatic effects have been neglected. A uniform plasma with density ρ_0 and pressure p_0 permeated by a magnetic field $\mathbf{B}_0 = B_0 \hat{x} = \text{const.}$ has been considered, and linear magneto-acoustic waves have been studied. The results shown in Fig. 18 suggest that ion-neutral collisions are more important for fast waves (for which τ_D/P is between 1 and 10^5) than for slow waves (for which τ_D/P varies between 10^4 and 10^8). Therefore, one can conclude that the effects arising from the partial ionization of the plasma are unimportant for slow waves, while fast waves can be damped efficiently for moderate values of the ionization fraction, $\tilde{\mu} \sim 1$, i.e., almost neutral plasmas.

Another interesting feature is that when plotting the period or the damping time of the fast wave versus the wavenumber, at a certain critical wavenumber (k_c) the fast wave disappears. The reason is that the critical wavenumber depends on the ionization fraction through η_C (Cowling's magnetic diffusivity). Hence, in a partially ionized plasma the fast mode only exists as a damped propagating wave for wavenumbers below the critical value, k_c . For wavenumbers greater than this critical value we have a damped disturbance instead of a propagating wave.

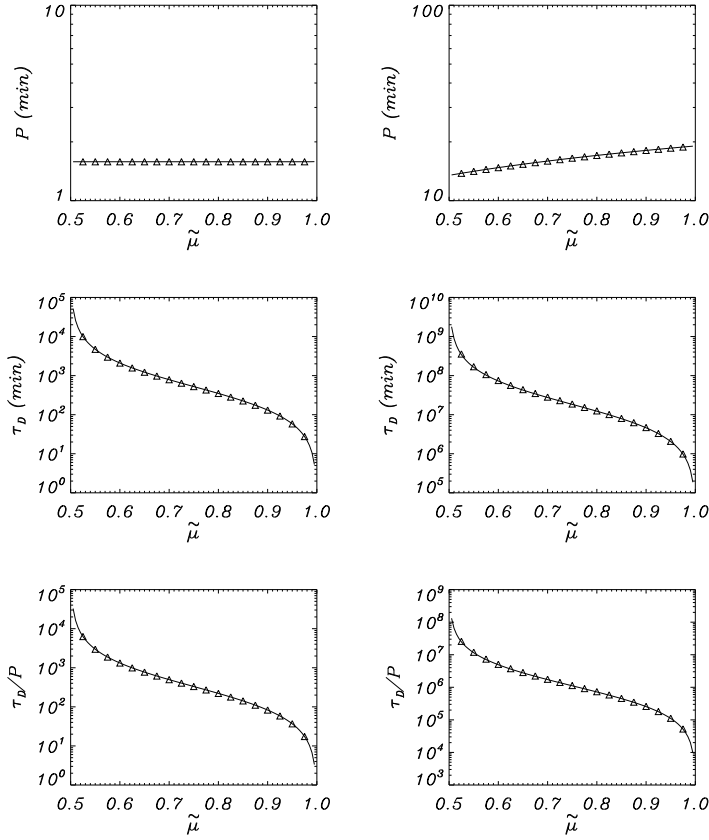


Fig. 18 Period, damping time and τ_D/P versus the ionization fraction for the fast wave (left) and the slow wave (right). The parameter values used are $T_0 = 8000$ K, $\rho_0 = 5 \times 10^{-14}$ g/cm³ and $B_0 = 10$ G, for which the Alfvén speed is 126 km s⁻¹, the sound speed ranges from 10.5 to 14.9 km s⁻¹ and the plasma β varies between 0.008 and 0.017. In addition, $k_x x_0 = \pi/2$ and $k_z x_0 = 0.1$. The solid lines represent the numerical solutions of the dispersion relation while the triangles represent the results obtained with approximate expressions. Adapted from Forteza *et al.* (2007).

Apart from magneto-acoustic waves, the time damping of Alfvén waves due to partial ionization effects has also been studied (Forteza *et al.*, 2008). Figure 19 shows the results obtained for the period, the damping time and the ratio of the damping time to the period. In this Figure the solution for a fully ionized plasma ($\tilde{\mu} = 0.5$) with magnetic resistivity (Ferraro and Plumpton, 1961; Kendall and Plumpton, 1964) is also shown. The Alfvén wave behavior is similar to that of the fast wave in the adiabatic partially ionized case. When ion-neutral collisions become the dominant mechanism, fast and Alfvén waves have similar period and damping time and, as for the fast wave, the ratio of the damping time to the period decreases when going to almost neutral plasmas. A critical wavenumber (k_c^a) also appears for the Alfvén waves. This quantity depends on the ionization fraction and on the propagation angle. Usually, k_c^a is larger than k_c for fast waves, and both critical wavenumbers become equal for parallel propagation.

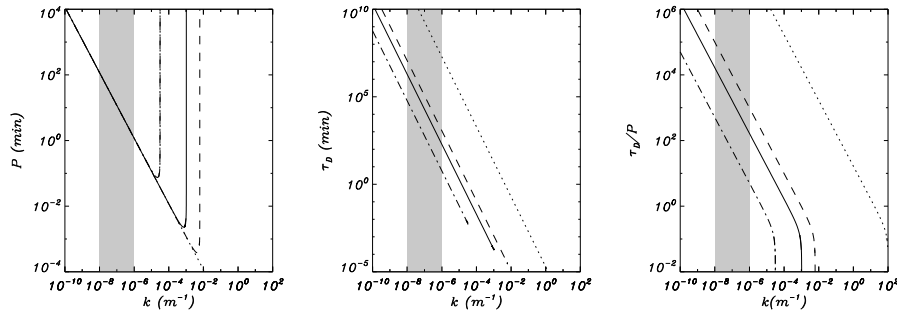


Fig. 19 Period, damping time and ratio of the damping time to the period for the Alfvén wave in a partially ionized plasma with $\tilde{\mu} = 0.5$ (dotted), $\tilde{\mu} = 0.6$ (dashed), $\tilde{\mu} = 0.8$ (solid) and $\tilde{\mu} = 0.99$ (dash-dotted). Adapted from Forteza *et al.* (2008).

4.3.4 Damping of Prominence Thread Oscillations by Resonant Absorption

Arregui *et al.* (2008) studied the resonant absorption of transverse kink waves in filament threads. They considered a straight, cylindrically symmetric flux tube of mean radius a , and neglected the effects of gravity. The inhomogeneous filament thread occupies the full length of the tube, and is modeled as a density enhancement with a non-uniform radial distribution of density $\rho(r)$ across the structure. The authors use the zero- β approximation, so that slow waves are absent, and they consider perturbations with azimuthal mode number $m = 1$, representing fast kink waves with transverse displacement of the tube. For fast kink waves to be damped by resonant absorption, the Alfvén speed must vary across the structure. The authors assume that there is a transition layer with thickness l between the interior of the filament and the surrounding corona. The ratio l/a provides a measure of the transverse inhomogeneity length scale, and can vary in between $l/a = 0$ (homogeneous tube) and $l/a = 2$ (fully non-uniform tube). The global $m = 1$ kink mode is resonantly coupled to local Alfvén waves. This coupling causes excitation of localized Alfvénic oscillations and damping of the global kink mode.

Combining long-wavelength and thin boundary ($l/a \ll 1$) approximations, analytic expressions for the damping time over the period can be written as (e.g., Hollweg and Yang, 1988; Sakurai *et al.*, 1991; Goossens *et al.*, 1992, 1995; Ruderman and Roberts, 2002):

$$\frac{\tau_d}{P} = F \frac{a}{l} \frac{c+1}{c-1}, \quad (2)$$

where c is the density contrast of the thread, and F is a numerical factor that depends on the details of the density variation in the transition layer. Arregui *et al.* (2008) obtained numerical solutions of the MHD wave equations for the $m = 1$ modes. Figure 20 shows that analytical and numerical solutions display the same qualitative behavior with density contrast c , wavelength λ , and transverse inhomogeneity length scale l/a . For low values of the density contrast, the ratio τ_d/P rapidly decreases with increasing thread density (Fig. 20a). Interestingly, for the larger contrasts typically found in filament threads ($c \sim 100$), τ_d/P is nearly independent of c and λ (Fig. 20b), but rapidly decreases with increasing l/a (Fig. 20c).

The above results suggest that resonant absorption is a very efficient mechanism for the attenuation of fast kink waves in filament threads. It is not yet clear how this

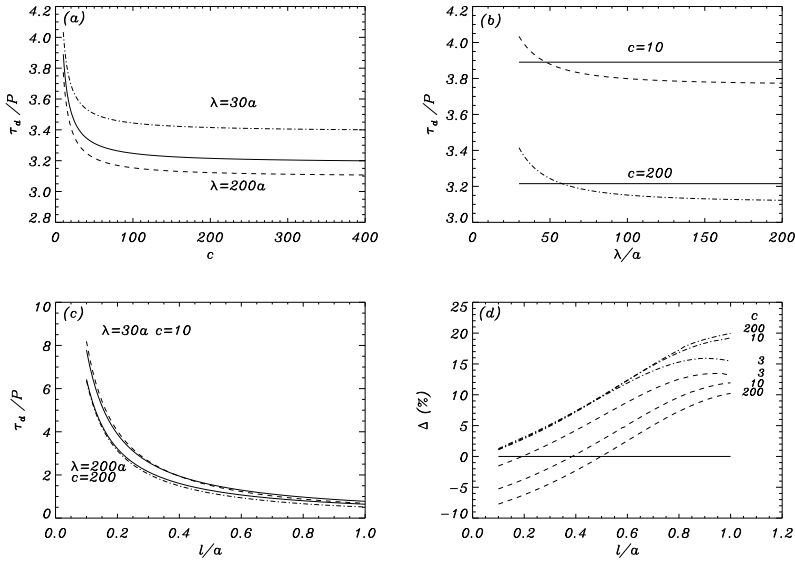


Fig. 20 Ratio of damping time τ_d and wave period P for fast kink waves in filament threads with $a = 100$ km. In all plots solid curves correspond to analytic solutions given by equation (2) with $F = 2/\pi$, and other curves correspond to numerical solutions. (a): Damping ratio as function of density contrast c with $l/a = 0.2$ and for two wavelengths. (b): Damping ratio as function of wavelength with $l/a = 0.2$ and for two density contrasts. (c): Damping ratio as function of transverse inhomogeneity length scale l/a for two combinations of wavelength and density contrast. (d): Percentage difference Δ of numerical and analytical values of the damping ratio, for $\lambda = 30a$ (dashed lines) and $\lambda = 200a$ (dash-dotted lines), and for different values of density contrast (see labels). Adapted from Arregui *et al.* (2008).

affects of overall dynamics of prominence plasmas. One possibility is that the resonant absorption causes significant heating of the prominence plasma, resulting in chromospheric evaporation (section 3). This may alter the density profile of the prominence thread, which changes the Alfvén wave resonance condition (e.g., Ofman *et al.*, 1998). Future modeling of the dynamics of prominence plasmas should include the effects of resonant absorption.

4.3.5 The Effects of Material Flows

As discussed in section 3, flows are a ubiquitous feature in prominences and filaments, and are routinely observed in H α , UV and EUV lines (see section 4, Paper I). Soler *et al.* (2008b) investigated the effects of both mass flow and non-adiabatic processes on the oscillations of an individual prominence thread. The thread is modeled as an infinite homogeneous cylinder with radius a , density ρ_p , temperature T_p , and parallel flow velocity $U_p \geq 0$. The cylinder is embedded in an unbounded homogeneous corona with density ρ_c and temperature T_c . The magnetic field is B_0 everywhere and the total pressure is assumed to be continuous across the interface between the flux tube and the external medium. For simplicity, the hot coronal part of the magnetic tube that contains the thread is not taken into account, and gravity is neglected. The equilibrium configuration is shown in Figure 21.

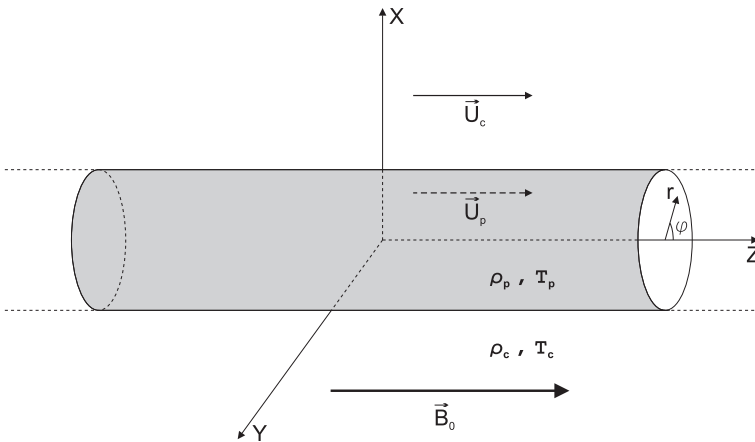


Fig. 21 Sketch of the equilibrium. Adapted from Soler *et al.* (2008b).

Figure 22 shows the dependence of the period, damping time, and their ratio as a function of the flow velocity for the slow, fast and thermal modes (for an explanation of the thermal mode, see Carbonell *et al.*, 2009). The longitudinal wavenumber has been fixed to $k_z a = 10^{-2}$, which corresponds to a value within the observed range of wavelengths. The flow velocities in the range $0 - 30 \text{ km s}^{-1}$ are considered, which corresponds to the observed flow speeds in quiescent prominences. The anti-parallel slow wave becomes a backward wave for $U_p \approx 8.5 \text{ km s}^{-1}$, which corresponds to the non-adiabatic sound speed, causing the period of this solution to grow dramatically near such flow velocity. However, the period of both parallel and anti-parallel fast kink waves is only slightly modified with respect to the solution in the absence of flow, and the thermal wave now has a finite period, which is comparable to that of the parallel slow mode. The damping time of slow and thermal modes is independent of flow velocity, but the attenuation of the fast kink mode is affected by the flow. The larger the flow velocity, the more attenuated the parallel fast kink wave, whereas the opposite occurs for the anti-parallel solution. This behavior is due to weak coupling of the fast modes to external slow modes (for details see Soler *et al.*, 2008b).

Terradas *et al.* (2008) modeled the transverse oscillations of flowing prominence threads as observed by Okamoto *et al.* (2007) with SOT. The kink oscillations of a flux tube containing a flowing dense part, which represents the prominence material, were studied from both analytical and numerical points of view. The results determined that there is almost no difference between the oscillation periods when steady *vs.* flowing threads are considered. Also, the resulting period matches that of a kink mode. In addition, to obtain information about the Alfvén speed in oscillating threads, a seismological analysis as described in 4.4 was performed.

4.4 Prominence Seismology

The main goal of prominence seismology is to infer the internal structure and properties of solar prominences from the study of their oscillations. One of the most searched for parameters is the prominence magnetic field strength and attempts to determine it have

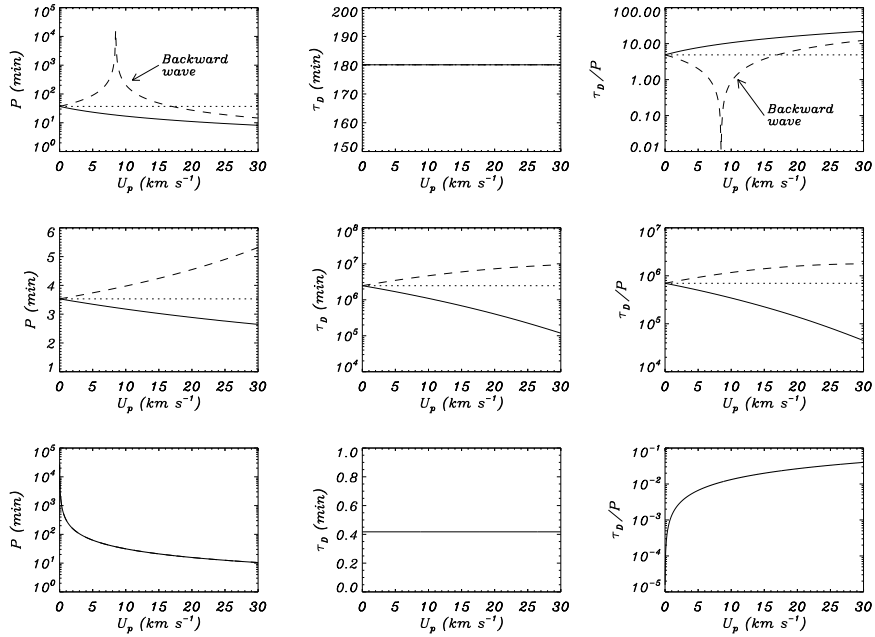


Fig. 22 Period (left), damping time (center), and ratio of the damping time to the period (right) versus the flow velocity for the fundamental oscillatory modes with $k_z a = 10^{-2}$. Upper, mid, and lower panels correspond to the slow, fast kink, and thermal modes, respectively. Different line styles represent: parallel waves (solid line), anti-parallel waves (dashed line), and solutions in the absence of flow (dotted line). Adapted from Soler *et al.* (2008b).

been made. For instance, using the significant periods obtained from the Fourier analysis of Doppler velocity time series belonging to an active region filament, Régnier *et al.* (2001) applied the theoretical model of Joarder and Roberts (1993) to determine the magnetic field and the angle of the magnetic field with the long axis of the observed filaments. They used the periods to identify the modes involved in the oscillations and after this identification they obtained $18^\circ \pm 2.5^\circ$ for the angle, assuming a prominence temperature of 8000 K and an analytical relationship between the magnetic field strength and the density. Pouget *et al.* (2006) followed the same procedure in the case of filaments observed with CDS. They identified six modes (slow, fast and Alfvén) involved in the oscillations and, using the same theoretical model, they obtained values between 19° and 35° for the angle and between 10 and 35 G for the magnetic field strength. All these determinations must be considered with care because the identification of the modes based on the periods is very uncertain; apart from the periods, the velocity polarization is of paramount importance for the mode identification in slab models.

As discussed in section 4.3.1, Díaz *et al.* (2002) considered a cylindrical model of a prominence thread. According to this model, the cool prominence thread has a radius b , and its length $2W$ is less than the length $2L$ of the flux tube on which the thread is located (see Fig. 14). The density in the prominence is ρ_p , the density in the coronal part of the flux tube is ρ_e , and the density in the surrounding corona is ρ_c . An important result of Díaz *et al.* (2002) is that the dimensionless oscillation frequency

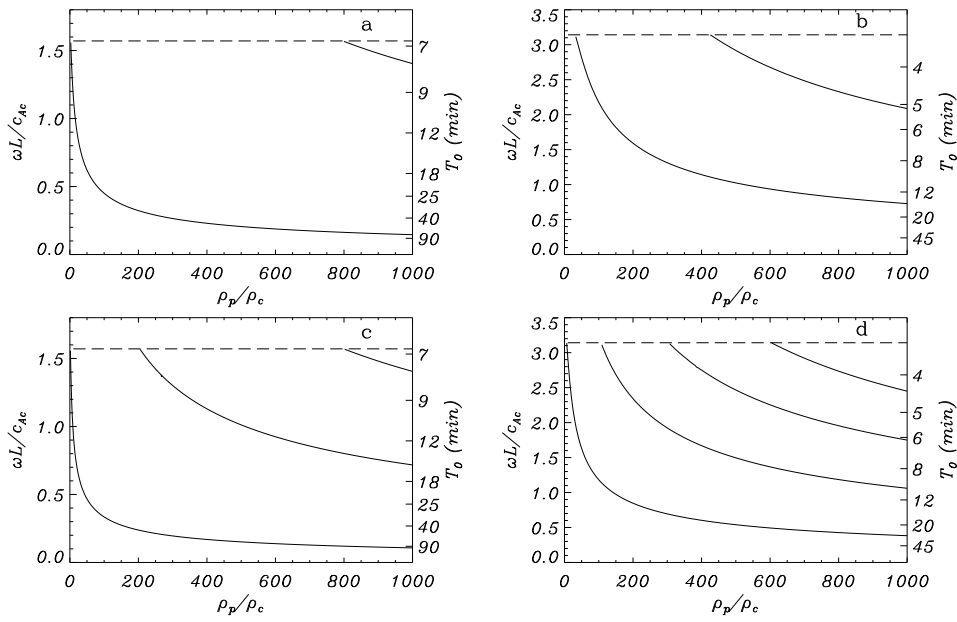


Fig. 23 Frequency of (a) and (c) the kink even modes and (b) and (d) the kink odd modes against ρ_p/ρ_c for the parameters $\rho_e/\rho_c = 0.6$ and $b/L = 0.001$. In (a) and (b) $W/L = 0.1$, while in (c) and (d) $W/L = 0.2$. The right axis provides with the period T_0 obtained after assuming the background magnetic field strength, the coronal density and the half-length of field lines are $B_0 = 5$ G, $\rho_c = 8.37 \times 10^{-13}$ kg/m³ and $L = 5 \times 10^4$ km. The horizontal dashed line in each plot gives the cut-off frequency. Adapted from Díaz *et al.* (2002).

$\omega L/c_{Ae}$ depends mainly on the ratios ρ_p/ρ_c and W/L , and is insensitive to the ratios b/L and ρ_e/ρ_c . Here c_{Ae} is the coronal Alfvén speed. Fig. 23 shows the dimensionless frequency of some modes for fixed values of fibril length W/L , thickness b/L , and ρ_e/ρ_c . Using such diagrams, we can perform a seismological analysis if some of the involved quantities are provided by observations. The availability of this observational information would allow us to determine the numerical values of the rest of prominence physical parameters. These examples point out that in order to determine the magnetic field strength, and apart of the oscillatory period, other physical properties of the prominence, such as the density, must be known or assumed.

In the theoretical model used by Terradas *et al.* (2008) (section 4.3.5), prominence and coronal Alfvén speeds are related through the ratio between prominence and coronal densities. Therefore, once this ratio is fixed and the coronal Alfvén speed is determined from the dispersion relation for the kink mode, the Alfvén speed in prominence threads can be determined. Figure 24 shows the dependence of the Alfvén velocity in the thread as a function of the coronal Alfvén velocity, for two different threads, when different density ratios and lengths of the magnetic field lines are considered. It can be seen that for a certain value of the coronal Alfvén speed the prominence Alfvén speed stabilizes. Using this analysis, lower bounds on the Alfvén speeds in different prominence threads can be obtained.

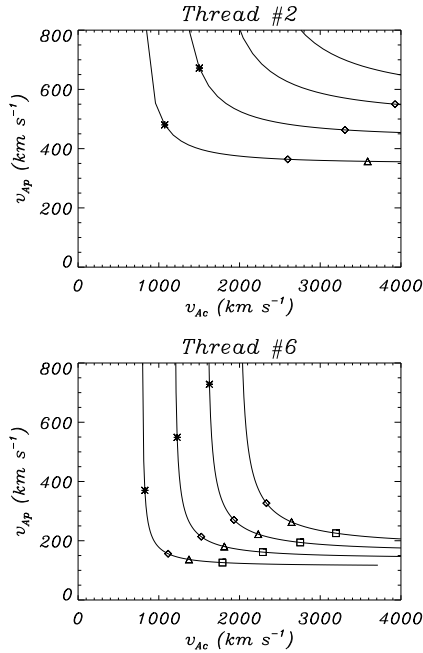


Fig. 24 Dependence of the Alfvén velocity in the thread as a function of the coronal Alfvén velocity for two of the threads studied by Okamoto *et al.* (2007). In each panel, from bottom to top, the curves correspond to a length of magnetic field lines of 100,000 km, 150,000 km, 200,000 km, and 250,000 km, respectively. Asterisks, diamonds, triangles, and squares correspond to density ratios of the thread to the coronal gas $\rho_p/\rho_c \simeq 5, 50, 100, 200$. Adapted from Terradas *et al.* (2008).

For the threads considered and taking the length of the magnetic field lines to be 100,000 km, the lower bounds of the Alfvén speed are between $120 - 350 \text{ km s}^{-1}$. These values are consistent with strong magnetic fields (50 G) and large densities ($1 - 8 \times 10^{11} \text{ cm}^{-3}$), or weaker magnetic fields (10 G) and lower densities ($0.4 - 3 \times 10^{10} \text{ cm}^{-3}$). These densities are within the ranges inferred from spectroscopic techniques (see sections 2.2 and 3.3 of Paper I). Further assumptions about the density, appropriate for the considered model, but not based upon simultaneous observations (which are not available), must be made for a numerical determination of the magnetic field.

Finally, an important conclusion in Arregui *et al.* (2008) (section 4.3.4) is that in equation (2) the damping rate becomes independent of density contrast for large values of this parameter. This fact has several seismological implications: First, the determination of the density contrast in the case of prominences is not as crucial as in other problems where the density contrast is low; second, by assuming a density contrast c of infinity in equation (2) an estimate of the transverse inhomogeneity length scale l/a can be determined. Using $\tau_d/P = 4$, we find $l/a \sim 0.15$, i.e. high-density threads are compatible with thin inhomogeneous layers. Furthermore, knowing the period and the wavelength, the Alfvén speed in threads can be also obtained. To make further progress and to obtain the magnetic field strength the prominence density is required.

In summary, the determination of the magnetic field strength is not straightforward. Depending on the theoretical model assumed to interpret the oscillations, additional information on numerical values of parameters such as prominence and coronal densities, geometrical dimensions, etc., need to be observationally acquired before the magnetic field strength can be determined.

4.4.1 Concluding Remarks

The study and understanding of small-amplitude prominence oscillations is a challenging task from the observational and theoretical point of view. The number of different physical effects (non-adiabaticity, flows, partial ionization, etc.) involved suggests that they must be explored in a systematic manner in order to obtain a full understanding of the properties of these oscillations. From a theoretical point of view, the main question could be: What do we need in order to foster theoretical understanding of prominence oscillations? Of course, a simple answer would be better observations having high spatial and time resolution. However, this would not be enough because our current knowledge of the internal structure and physical properties of solar prominences is not complete. For example, the magnetic field structure which supports and shields the prominence is not fully understood. Without a clear understanding of the magnetic structure it becomes difficult to advance our knowledge of prominence oscillations. Furthermore, are the flows real or are there ionization or excitation fronts changing the physical conditions and mimicking flows? What is the mechanism responsible for prominence heating? Partial ionization seems to be a key feature in prominences, influencing not only magneto-hydrodynamic waves but also the manner in which prominence plasma is tied to magnetic field lines and, right now, is starting to be considered in some theoretical studies.

From the above considerations, one can easily conclude that from the theoretical and observational point of view we are far from a complete understanding of prominence oscillations, and this conclusion is correct. In the near future, the joint use of two-dimensional, high-resolution observations, modern data analysis techniques, and complex theoretical models, incorporating as much physics as possible and using state of the art numerical simulations, should help us to make further progress in this field.

5 Formation and Large-Scale Patterns of Filament Channel and Filaments

5.1 Global Patterns and Formation Locations

Solar filaments (a.k.a. prominences) form over a wide range of latitudes on the Sun. Their locations spread everywhere, from the active belts to the polar crown. Poleward transport of magnetic flux across the solar surface during the solar cycle is accompanied by a poleward migration of the preferred locations of filament formation (McIntosh, 2002; Minarovjech *et al.*, 1998; Ambroz and Schroll, 2002; Mouradian and Soru-Escaut, 1994). Although filaments may form at many locations on the Sun, they always form above Polarity Inversion Lines (PILs), which divide regions of positive and negative flux in the photosphere. As discussed in Section 2.1.2, a necessary condition for the formation of a filament is the presence of a filament channel at the height of the chromosphere (*e.g.*, Gaizauskas, 1998). Filament channels are the unique sites of filament formation. Channels are more fundamental than the filaments that form within them,

as not every channel contains a filament and a single channel may survive a succession of filament formations and eruptions. The structure of a filament channel is illustrated in Figure 4. A key feature of a filament channel, is that it is a region of dominant horizontal field where the field on either side points in the same direction. As a result, filament channels are interpreted as locations of strong magnetic shear and highly non-potential magnetic fields. The channels are believed to be a low atmosphere signature of a larger horizontal non-potential field that extends into the coronal volume (see Section 2.1.2). Presently it is unclear why channels and their non-potential fields build up along PILs, so understanding filament channel formation is key to understanding the evolution of magnetic fields on the Sun and their relationship to eruptive phenomena. By observing and interpreting their formation and evolution, we may examine directly the buildup to, and initiation of geoeffective space weather. In the discussion below we consider the global properties and formation locations as deduced from H α observations.

5.1.1 Global Classification Schemes

While filaments form at many locations on the Sun, very few studies have considered the exact nature or history of the PILs above which they form. Those studies that have considered this, are mainly restricted to studying large-scale, stable filaments and neglect smaller unstable filaments forming in the centers of activity complexes. Understanding the type of magnetic environment in which filaments form is key to understanding the magnetic interactions required for their formation.

Over the years many classification schemes for filaments and prominences have been developed (d'Azambuja and d'Azambuja, 1948). These schemes have referred to different features, including: the dynamics of the material in the prominence, whether it is stable or eruptive, or finally with respect to the distribution of the magnetic flux below the filament. For a discussion see Tandberg-Hanssen (1995). In this paper we use a classification scheme of filaments in terms of their spatial location on the Sun (Engvold, 1998). In later sections when we discuss the possible mechanisms of filament formation this classification scheme will prove useful in illustrating that different mechanisms may form different types of filaments. As given in the introduction the types of filament were described as: ARF (Active Region Filament), IF (Intermediate Filament), and QF (Quiescent Filament). An ARF is one which forms in the centers of active regions or activity complexes. In contrast, IFs form between active regions and decaying regions of unipolar plage. Finally QFs form in regions of weak background fields. Observations tend to show that IFs and QFs are larger, much more stable structures with longer lifetimes (weeks to months) compared to ARFs, which are generally unstable with a lifetime of only a few hours to days.

While the classification scheme of Engvold (1998) provides a useful distinction between filaments forming inside and outside active regions, to understand the role that magnetic fields play in the formation, structure and evolution of filaments it is important to understand the exact type of magnetic configurations wherein filaments form. One early classification scheme (Tang, 1987) splits them into two categories based on the nature of the PIL above which the filament lies. The first category is one in which the filament forms above a PIL lying within a single bipolar unit of flux, and is classified as an “Internal Bipolar Region Filament” (see Figures 25a and 26a). In the second, the filament forms above a PIL which lies between two separate magnetic dipoles and is called an “External Bipolar Region Filament” (Figures 25b and

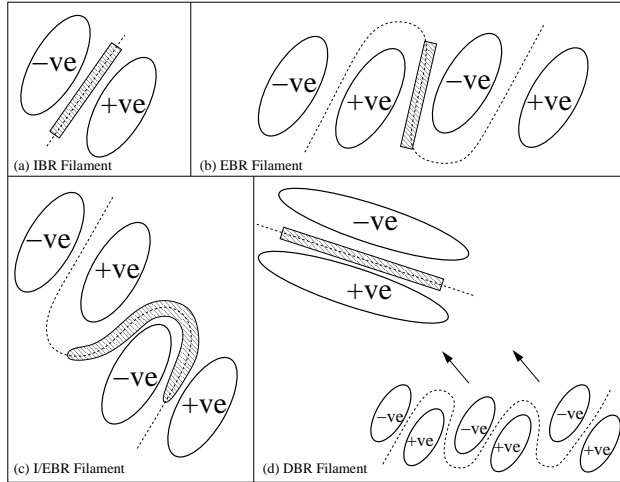


Fig. 25 Classification scheme for solar filaments based on those of Tang (1987) and Tandberg-Hanssen (1995) with two new categories (c and d) introduced by Mackay *et al.* (2008). (a) Filaments which form above the internal PIL of a single bipole are classified as IBR. (b) Those forming on the external PIL between bipoles or between bipoles and unipolar regions of flux are classified as EBR. (c) Filaments that lie both above the internal PIL within a bipole and the external PIL outside the bipole are classified as I/EBR. (d) Filaments that form in diffuse bipolar distributions created through multiple flux emergences (such that the diffuse region can no longer be associated with any single bipole emergence) are classified as DBR. This category is expected to lie only at high latitudes. This figure is taken from Figure 2 of Mackay *et al.* (2008).

26b). Tandberg-Hanssen (1995) describes these two categories as Type A and Type B, respectively. Early observations by Tang (1987) showed that, when filaments are classified into these two types, over 60% of filaments form external to bipolar regions.

In a more recent study Mackay *et al.* (2008) reconsidered where long, stable solar filaments form. Their study followed the history and evolution of the PILs underneath filaments using a wide range of data. The data included H α synoptic maps, large-scale H α images from the Ottawa River Solar Observatory (ORSO), Kitt Peak (KP) full disk and synoptic magnetograms, KP He 10830 synoptic images, and results from magnetic flux transport simulations (Yeates *et al.*, 2007). Through following the history and evolution of the PILs above which filaments form, the authors determined the origin of flux regions at high latitudes from their initial bipolar source regions at active latitudes. As with previous studies the data and techniques employed were preferentially directed towards studying large, stable filaments, so they did not include smaller unstable filaments such as those found in the centers of activity complexes.

To distinguish the different bipole interactions that could lead to the formation of filaments, Mackay *et al.* (2008) introduced two additional categories for filaments compared to those defined by Tang (1987): “Internal/External Bipolar Regions Filaments” (I/EBR) and “Diffuse Bipolar Region Filaments” (DBR). The I/EBR filaments are defined as filaments that lie above both the internal PIL of a bipole and the external PIL surrounding the bipole (Figures 25c and 26c), and therefore could not be classified into the scheme proposed by Tang (1987). In contrast, the DBR filaments are located in essentially a bipolar distribution of flux, but where the polarities defining the bipole

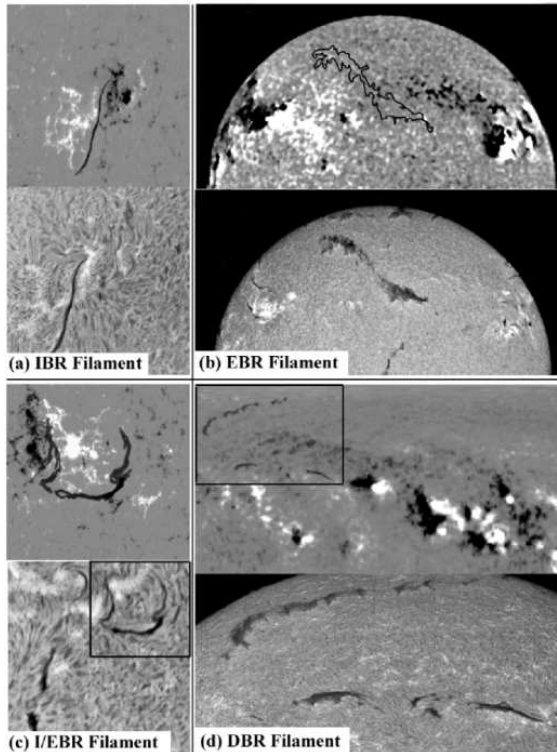


Fig. 26 Examples of the four categories of filaments shown in Figure 25 (from Mackay *et al.*, 2008). In each of the panels (a)-(d), the bottom plot is an H α image from the ORSO, while the top image shows the radial magnetic field derived from either (a)-(c) a full-disk magnetogram or (d) a synoptic magnetogram from Kitt Peak. Outlines of the H α filaments are superimposed on each of the magnetograms. The dates of the observations are (a) 26th June 1979, (b) 6th May 1979, (c) 27th September 1979 and (d) 14th July 1979. For panels (c) and (d) the areas enclosed by the boxes denote the corresponding area of (c) the magnetogram and (d) the H α image. In panel (d) (top image) the low latitude activity complexes which will extend poleward over time and interact to produce diffuse regions of flux at high latitudes can be clearly seen.

did not emerge together. The formation of the bipolar distribution was the result of many flux emergences, coalescences and cancellations such that the polarities on either side of the filament could not be attributed to a single bipole emergence (Figures 25d and 26d). On comparing the classification scheme of Engvold (1998) with those of Tang (1987) and Mackay *et al.* (2008), ARFs could be of either Internal Bipolar, External Bipolar or Internal/External Bipole filament categories. IFs are always of External Bipolar type and QFs either Internal, External, Internal/External or Diffuse Bipolar Region type. Therefore in principle active region and quiescent filaments may form in very different magnetic environments. By using the four categories (of IBR, EBR, I/EBR and DBR) and extending the work of Tang (1987) to four distinct phases of the solar cycle (two before and two after cycle maximum) the authors were able to distinguish more clearly the different types of bipole interactions leading to the formation of Intermediate and Quiescent filaments.

Of the 603 filaments studied by Mackay *et al.* (2008), 92% formed at locations requiring multiple bipole interactions (the breakdown comprised of 62% EBR, 17% DBR and 13% I/EBR). Only 7% formed within a single bipole. These results show that large-scale filaments, namely those of the IF and QF type preferentially form at sites of multiple bipole interactions. Very few of them occur within a single bipole. Furthermore, by considering four distinct phases of the solar cycle, Mackay *et al.* (2008) showed that only EBR filaments exhibit any form of solar cycle dependence, with the other three types remaining essentially constant (see Figure 3 of Mackay *et al.*, 2008). The dependence showed that the number of EBR filaments varied in phase with the solar cycle with more at cycle maximum than minimum. Such a variation indicates that the formation of EBR filaments must be strongly related to the amount of flux emergence in the solar cycle.

5.1.2 The Hemispheric Pattern of Solar Filament Channels and Filaments

While the basic properties of solar filaments have long been known, filament channels and filaments have been classified more recently in terms of their chirality (Martin *et al.*, 1994). As discussed in section 2.1.2, this chirality may take one of two forms: dextral or sinistral. Dextral/sinistral filament channels and filaments have an axial magnetic field that points to the right/left when the main axis of the filament is viewed from the positive polarity side of the PIL (see Figure 5). The chirality of filament channels may be deduced from high resolution H α images combined with magnetograms, whereas the chirality of filaments may be determined from that of the channel, direct magnetic field measurements or from the relationship of filaments to their barbs (dextral filaments \sim right bearing barbs, sinistral filaments \sim left bearing barbs). In general due to the lack of high resolution H α data and direct measurements of magnetic fields within prominences, filaments are mostly classified using their relationship to barbs (Pevtsov *et al.*, 2003; Yeates *et al.*, 2007). López Ariste *et al.* (2006) and Martin *et al.* (2008) used the chirality rules to resolve the 180-degree ambiguity in photospheric vector-field measurements. In force-free field models (e.g., Aulanier and Démoulin, 1998; Mackay, Longbottom & Priest, 1999; van Ballegooijen *et al.*, 2000; Mackay and van Ballegooijen, 2005) this chirality is directly related to the dominant sign of magnetic helicity that is contained within the filament and filament channel. A dextral filament will contain dominantly negative helicity, while a sinistral filament positive helicity. Hence, filaments and their channels may be regarded as indicators of sheared non-potential fields within the solar corona. Their transport across the solar surface is therefore an indication of the large-scale transport of magnetic helicity across the Sun (Yeates *et al.*, 2008b) a key feature in explaining many eruptive phenomena. A surprising feature of the chirality of filaments is that it displays an unusual large-scale hemispheric pattern: dextral/sinistral filaments dominate in the northern/southern hemispheres respectively (Martin *et al.*, 1994; Zirker *et al.*, 1997; Pevtsov *et al.*, 2003; Yeates *et al.*, 2007). This pattern is unusual as it is exactly opposite to that expected from differential rotation acting on a North-South coronal arcade. Although dextral/sinistral filaments dominate in the northern/southern hemisphere, observations show that exceptions to this pattern do occur. Therefore any model which tries to explain the formation of filaments and their dominant axial magnetic fields must explain not only the origin of this hemispheric pattern but also why exceptions arise. The origin of this hemispheric pattern will be discussed in Section 5.5.

It is clear from the above discussion that solar filaments form or are found in a wide range of magnetic environments on the Sun, ranging from the rapidly evolving activity complexes to the slowly evolving poleward streams of flux that extend out of the active latitudes towards the poles. To explain the formation of these filaments, observational studies and a wide range of theoretical models have been produced. The review will now consider observational case studies of the formation of filaments (Section 5.2). After discussing these, models of filaments formation will be discussed in Section 5.3. The observations will then be used to clarify which models of filament formation are applicable to which filament formation locations (Section 5.6).

5.2 Observations of Filament Channel and Filament Formation

To understand the magnetic environment and interactions leading to the formation of filament channels and filaments, it is useful to discuss test cases. To date, very few examples of filament channel formation have ever been observed, so the exact formation mechanism remains debatable. Six recent publications present detailed case studies. Four cases show the formation of filament channels through surface effects that reconfigure pre-existing coronal fields, while in the latter two examples flux emergence of horizontal flux ropes is deduced by the authors to play a critical role. Thus from interpreting the observations there appear to be two opposing views on how filament channels and filaments form. In this discussion we will consider the key observational features and determine whether the two views may be reconciled.

5.2.1 Evidence of the Reconfiguration of Pre-Existing Coronal Fields in the Formation of Filament Channels

Observations reported by Gaizauskas *et al.* (1997) and Gaizauskas *et al.* (2001) show that surface motions acting on pre-existing coronal fields play a critical role in the formation of filament channels and filaments. In the first case, an Intermediate Filament (IF) forms over a short period of a few days, while in the second a Quiescent Filament (QF) forms over a period of months. In both cases the filaments form on PILs external to any single bipole and in the classification scheme of Section 5.1.1 would be classed as External Bipolar Regions Filaments. Although the two cases occur over very different time and length scales there are a number of important similarities.

Both cases begin with the emergence of a significant amount of magnetic flux in the form of an activity complex. Importantly however, no filaments form during the process of flux emergence. In fact, for the large scale QF the filament forms approximately 27 days after major flux emergence subsides. In both cases a necessary condition for the formation of the filament channels was flux convergence and cancellation at a PIL between separate bipolar regions. Such convergence and cancellation of flux was also shown to be important for filament formation in the papers by Gaizauskas (2002) and Martin (1998). Finally and most importantly, in each case a significant amount of magnetic shear was seen to build up in the activity complexes as they emerged. The redistribution of this non-potential field through surface motions towards the PIL produces a preferred direction of the coronal field above the PIL and plays a critical role in the formation of the filament channels, the necessary ingredient for filament formation (Mackay and Gaizauskas, 2003).

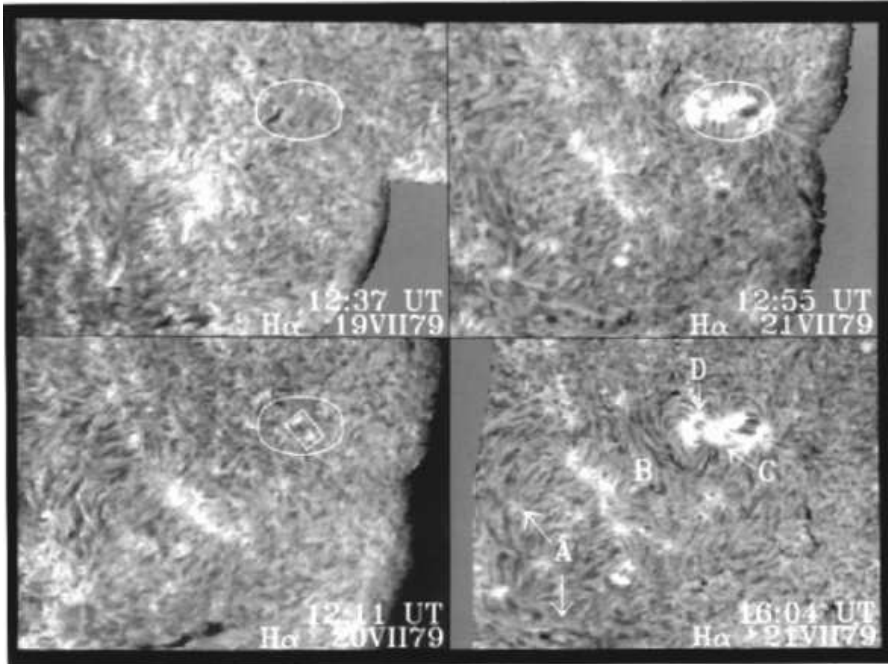


Fig. 27 H α images from Gaizauskas *et al.* (1997) (Figure 2) of the early stages in the formation of an Intermediate Filament between an old remnant region (bright plages A and B in bottom right images) and an emerging activity complex (inside oval). The H α images correspond to 19th-21st July 1979 whereas the filament did not form until the 25th July 1979.

Figures 27 and 28 illustrate the main stages in the formation of a filament channel and IF over a period of five days between the 20th-25th July 1979 (see Figures 2 and 4 in Gaizauskas *et al.*, 1997). The formation of this southern-hemisphere IF involves the interaction of two distinct magnetic flux distributions, an old remnant region (M^cMath 16159) and a new emerging region (M^cMath 16166). In the H α image of Figure 27 (top left) the bright North-South plage outlines the old remnant region; the oval denotes the location where new magnetic flux will emerge on the following day. A key feature of this image is that the chromosphere is free of any strong patterns of magnetic fields within the oval. New magnetic flux first emerges inside the rectangle within the oval on the 20th July (bottom left) and then more strongly between the 20th and 21st (top right). Over this time there is very little change in the magnetic field of the old remnant region. Magnetic field observations show that the activity complex (Gaizauskas *et al.*, 1983; Benevolenskaya, 2005) is made up of two or more sunspot pairs. Significantly, no filament forms near or around the activity complex during this period of rapid flux emergence. The key development in the formation of the filament channel occurs between the two right hand panels taken just three hours apart on the 21st July (at the location denoted by B in lower right panel). Over this period a band of co-aligned fibrils form at the tail end of the new activity complex, between it and the old remnant region. These co-aligned fibrils indicate a magnetic field at this location with a dominant horizontal component, i.e. that a filament channel has formed. According to a model by Mackay *et al.* (1997) this pattern of co-aligned fibrils can only be explained

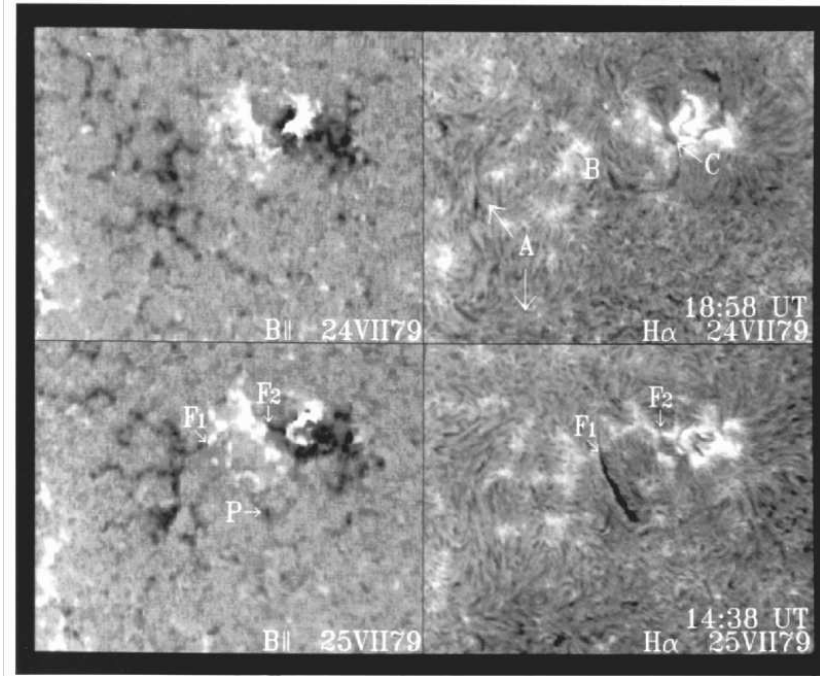


Fig. 28 H α image (right) and magnetogram (left) from Gaizauskas *et al.* (1997) showing the final stages of the formation of an Intermediate Filament on the 24th and 25st July 1979. For the magnetogram images white represents positive and black negative flux. The Intermediate Filament forms on the 25th July after flux convergence and cancellation occurs at F1.

by the extended non-potential magnetic field of the activity complex in which the field contains a large amount of positive helicity (correct sign for the southern hemisphere).

No filament forms as magnetic flux continues to emerge within the activity complex. The emergence ceases on the 23rd July, thereafter the activity complex expands and flux begins to disperse into the filament channel. In Figure 28 the distribution of magnetic flux (left column) and corresponding H α images (right column) can be seen for the 24th and 25th July. In the magnetogram images, white (black) represents positive (negative) flux. After major flux emergence ceases on the 23rd the trailing positive polarity of the activity complex disperses or diffuses out. This dispersion causes a convergence of flux between the old and new regions. On 25th July, five days after the complex started to emerge, cancellation of flux occurs at the point F1 (bottom right). The filament forms after this cancellation and passes through the location of flux cancellation. It was a stable structure which survived for a full solar rotation and can clearly be seen to lie on a PIL which is external to any one bipolar region. Subsequent modeling by Mackay *et al.* (1997) showed that the resulting magnetic structure of the filament could only be explained by the interaction of the combined fields of both the old and new magnetic distributions. Both fields were highly non-potential, again with a significant amount of positive helicity which must have originated during the creation of the new activity complex. It is clear from the observations that reconfiguration of the previously emerged fields played a critical role in the formation of the filament channel.

Gaizauskas *et al.* (2001) described a similar process of filament channel and filament formation, but this time for a QF which is nearly $1R_{\odot}$ in length. The process of formation once again begins with the emergence of new flux, but this time in the form of two neighboring activity complexes in the northern hemisphere. Fibril alignment at the chromosphere once again shows that the extended fields of the activity complexes are highly non-potential with negative helicity. As with the previous case, the filament only forms after major flux emergence ceases and the activity complexes converge and partially cancel with one another. In contrast to the filament in the previous case, which took 5 days to form, for the large-scale case the QF takes nearly one full solar rotation (27 days) to appear.

In both cases described above no stable filaments form during the periods of the highest rates of flux emergence, and the authors concluded that surface motions acting on pre-existing coronal fields play a critical role in the formation of stable filaments through the interaction of multiple dipoles. This result is consistent with the classification of filaments given in Section 5.1.1 where the majority of filaments are found to lie in magnetic configurations that involve more than one dipole. A key role of these surface motions is to redistribute the helicity which is seen to emerge in the early stages to form the filament channel (Gaizauskas *et al.*, 1997, 2001; Mackay and Gaizauskas, 2003; Mackay and van Ballegooijen, 2005, 2006). At a later stage a filament may appear when mass is deposited into the channel. Convergence and cancellation of flux have also been shown to be important for filament channel formation according to the observations reported by Martin (1998) who reviews several clear examples, and Gaizauskas (2002), who shows that early in the solar cycle a unipolar region of flux has to extend 180° around the Sun to interact and cancel with an opposite polarity region before a filament can form on that PIL. For these cases the redistribution of flux, after emergence, is inferred to be a key process in the formation of the filament channel. In the more recent paper by Gaizauskas (2008), three different arrangements of interacting nests are considered for the formation of filament channels and filaments as flux disperses across the Sun. In each case channels and quiescent filaments form on the boundaries of these activity nests.

Schmieder *et al.* (2004) studied the formation of a filament in the complex center of a decaying active region formed out of smaller individual components, using multi-wavelength observations obtained during a “Joint Observing Programme” between ground-based instruments in the Canary Islands (the SVST and the MSDP on the VTT) and the TRACE satellite. They followed the evolution of three individual filament segments denoted F1, F2 and F3 over several days, and found that F1 and F2 gently merged into a single structure, as observed by a gradual filling in $H\alpha$ of the gap between them. This merging was associated with mild EUV brightenings and with small $H\alpha$ Doppler shifts at the merging point. While EUV brightenings are a good indicator of magnetic reconnection, the flows revealed that the merging first took place by dynamic exchanges between the two progenitors, until they formed a single long stable filament. Two days later segments F2 and F3 came into contact and produced a confined flare, as evidenced by EUV post-flare loops (Deng *et al.*, 2002). To determine the directions of the axial fields in the three filament segments, Schmieder *et al.* (2004) used the chirality rules for chromospheric fibrils and magnetic field polarity, the skew of the overlying coronal arcades, and the sense of twist in neighboring sunspots. It was then confirmed that when two filaments interact, magnetic reconnection takes place and leads to a merging when their chiralities are of the same sign, but leads to a flare when the chiralities are opposite (also see Malherbe, 1989; Martin, 1998; Rust, 2001;

van Ballegooijen, 2004; DeVore *et al.*, 2005). It was also inferred that magnetic helicity must slowly accumulate prior to filament merging, as seen by the rotation of a small twisted sunspot close to the merging point. Finally, it was suggested that magnetic reconnection first accelerates plasma between both progenitor filaments, and that it may later result in a change of topology which can sustain stable plasma all along the new filament.

More recent observations by Wang and Muglach (2007) have supported the work of Gaizauskas *et al.* (1997, 2001). Wang and Muglach (2007) describe examples of the formation of filament channels and filaments through comparing BBSO H α images with MDI normal component magnetograms. The authors describe how fibrils which are initially normal to the PIL rotate to lie parallel to the PIL over a period of 1 to 2 days and in doing so form a filament channel. Through studying the evolution of the magnetic fields the authors deduce that flux cancellation as a result of supergranular convection plays a key role in the formation of the filament channels. They argue that this cancellation process between opposite polarity elements removes the normal component of the field but leaves the component parallel to the PIL which builds up gradually to form the axial field of the filament channel. In contrast to Gaizauskas *et al.* (1997, 2001) they do not observe any significant helicity resulting from the emergence of the active regions. For the two clearest examples of filament formation, 15th January 2002 and October 7th 2002 (see Wang and Muglach (2007) Figures 2 and 5) the filaments form between bipolar regions of flux and background fields and therefore would be classified as IF and Exterior Bipolar Region Filaments. For the third case which is not so clear, the filament partially lies on both the internal and also the external portions of the PIL so would be an I/EBR filament or an AR filament.

On comparing the results of Gaizauskas *et al.* (1997) and Wang and Muglach (2007), while there are many similarities, there are also some differences in time scale. The clearest is the time difference required to form the filament channel. For Gaizauskas *et al.* (1997) the formation of the filament channel occurs over a 3 hour period and is attributed to the extended non-potential field of the activity complex containing a large amount of helicity. Cancellation of flux could not produce such a strongly sheared field over such a short period of time. In contrast, Wang and Muglach (2007) do not report any strong patterns of fibrils associated with helicity emerging in the active regions but rather form the filament channel over a period of 1 to 2 days in a much slower process of cancellation. Therefore there appear to be two complementary methods of forming a filament channel over different time scales.

5.2.2 Evidence of Emerging Horizontal Flux Tubes in Filament Formation

It is clear from the above observations that surface effects play a critical role in forming the studied IFs and QFs (which are long stable structures). Lites and Low (1997) describe a different process for forming short, unstable active-region filaments. In Lites and Low (1997) the emergence of a δ -spot is traced through vector magnetic field measurements using Advanced Stokes Polarimetry. Magnetic field vectors along part of the PIL within the emerging δ -spot show a concave up or dipped magnetic structure (see Figure 1 of Lites and Low (1997); also see Lites (2005)). A small active region filament forms at this location. The filament was however unstable with a lifetime of only 2 days. Lites and Low (1997) suggest photospheric material is dragged up into the corona through the levitation process, as a horizontal flux rope emerges (Rust and Kumar (1994), also see section 3).

A more recent example of the effect of evolving magnetic fields on the structure and stability of an active region filament is described by Okamoto *et al.* (2008) and Okamoto *et al.* (2009). In two papers, the authors present observations of a time series of vector magnetic fields taken by SOT underneath a pre-existing filament. The vector magnetic field measurements show a PIL with dominant horizontal field along it. This horizontal field probably represents that of the filament channel of the pre-existing filament. Over a period of 1.5 days the horizontal field vector changes from normal to inverse polarity and a dominant blue shift is observed. During this period the filament alters its appearance from a single structure, to a fragmented one and back again. Before returning to a single structure, brightenings are observed along the filament fragments in the Ca II H line.

From the observations the authors deduce two possible scenarios. In the first scenario they interpret the observations in terms of an emerging horizontal flux rope which fully emerges into the corona and occupies the position of the pre-existing filament. With this scenario the mass of the prominence originates from below the photosphere. The second scenario interprets the brightenings in Ca II H as evidence for reconnection between the pre-existing filament and a new flux rope that emerges free of mass. The reconnection then produces a single structure along the PIL. A difficulty with both scenarios is that no simulations of magnetic flux emergence have been able to emerge a horizontal flux rope through the photosphere.

In contrast to that put forward by the authors, a third possibility also exists. This fits the theoretical models discussed in Section 3.2. As the top part of a flux rope emerges, a likely outcome is the emergence of sheared arcades. A coronal flux rope may then be formed out of these arcades through the process of reconnection. This reconnection may lift cool material into the corona, as has been discussed in Section 3. If the axial component of the emerging arcade lies in the same direction as that of the pre-existing filament channel, the new and old flux systems may join to produce a single structure (see Section 5.4). To consider which, if any of these three scenarios are correct, new high resolution magnetic field observations at multiple levels in the solar atmosphere (e.g. photosphere, chromosphere and corona) are required.

5.2.3 Summary of Observations

The observations described in Section 5.2.1 and 5.2.2 provide evidence for filament formation arising from surface motions that reconfigure already existing coronal fields or, emerging flux tubes. So can the two methods be reconciled? The important distinction between these cases is the type and location of filaments formed in each case. For the first four cases surface motions play an important role in forming long stable Quiescent or Intermediate filaments which are External Bipolar Region Filaments, the dominant type of large-scale filament found at all latitudes on the Sun. In contrast, flux tubes emerging in a δ -spot forms an Active Region or Internal Bipolar Region Filament which is unstable, lasting merely two days.

While it is difficult to draw general conclusions from just six specific observations, they indicate that two different mechanisms might form filaments in different magnetic environments on the Sun. Thus large stable filaments of the IF and QF type (External or Diffuse Bipolar Region) may require surface motions to gradually reconfigure pre-existing coronal fields, while small, short-lived ARFs (Internal Bipolar Region) may form due to flux emergence. To determine whether different mechanisms do produce different types of filaments at different locations on the Sun, the formation of filaments

Table 3 Surface Models of Filament Formation

Single Bipole	Multiple Bipoles
van Ballegooijen and Martens (1989) ^{1,3,4,10}	Kuperus (1996) ^{1,3,4}
DeVore and Antiochos (2000) ^{1,4}	Kuijpers (1997) ^{3,4,8,10}
	Mackay <i>et al.</i> (1998) ^{3,4,6,8,10}
	Galsgaard and Longbottom (1999) ^{3,4}
	van Ballegooijen <i>et al.</i> (2000) ^{1,4,10}
	Martens and Zwaan (2001) ^{3,4,10}
	Lionello <i>et al.</i> (2002) ^{8,10}
	DeVore <i>et al.</i> (2005) ^{1,3,4}
	Mackay and van Ballegooijen (2005) ^{1,4,8,10}
	Welsch <i>et al.</i> (2005) ^{3,4,8,10}
	Litvinenko and Wheatland (2005) ^{3,4,8,10}
	Yeates <i>et al.</i> (2008a) ^{1,4,8,10}

Table 4 Sub-Surface Models of Filament Formation

Single Bipole	Multiple Bipoles
Low (1994) ⁷	van Ballegooijen and Martens (1990) ^{2,3,4,7}
Rust and Kumar (1994) ^{7,9}	Priest <i>et al.</i> (1996) ^{2,3,4,6}
Gibson <i>et al.</i> (2004) ^{7,9}	Oliver <i>et al.</i> (1999) ^{2,3,4,6}
Low and Hundhausen (1995) ^{7,9}	
Fan and Gibson (2004) ^{7,9}	
Fan and Gibson (2006) ^{7,9}	
Gibson and Fan (2006) ^{7,9}	
Magara (2006) ^{7,9}	
Magara <i>et al.</i> (2008) ^{7,9}	
(Fan, 2009) ^{6,9}	

over a wide range of latitudes needs to be considered in detail. Observational programs required to do this will be discussed in Section 5.6.3.

5.3 Theoretical Models of Filament Formation

Over the years many models have been constructed, each employing a variety of mechanisms in order to describe the formation of filaments. These models vary from descriptive papers to full numerical MHD simulations and consider two main problems. First, how to obtain the correct dipped magnetic field configuration with dominant axial magnetic field that follows the hemispheric pattern, and secondly, the origin of the dense plasma. While the second question relates more to thermodynamics (Karpen *et al.* (2001), section 3), this section which relates filaments to their underlying magnetic polarities is relevant to the first group of models. It is widely accepted that magnetic flux ropes are a suitable configuration to represent solar filaments; the main area of debate is how exactly these flux ropes may form. Therefore, the various models in that group may be broadly split into two distinct sub-groups: those employing surface effects to reconfigure coronal fields (Table 3) and those employing subsurface effects (Table 4). This split naturally arises from the discussion of the observations in Section 5.2. At the present time only those employing surface mechanisms can be directly compared to observations. In these tables the surface/subsurface models have also been subdivided

Table 5 Mechanisms of Filament Formation

Surface Mechanisms	Subsurface Mechanisms
(1) Differential Rotation (shear flows)	(2) Subsurface Motions
(3) Converging Flows	
(4) Magnetic Reconnection (atmosphere)	(5) Magnetic Reconnection (subsurface)
(6) Flux Emergence (bipoles)	(7) Flux Emergence (U-loops)
(8) Magnetic Helicity	(9) Magnetic Helicity
(10) Flux Cancellation/Diffusion	

into those acting in single or multiple bipolar configurations in account of the observations discussed in Section 5.1.1. The list contains models which consider the physical processes and mechanisms that may produce the 3D magnetic structure of filaments. It should only be regarded as representative and not exhaustive. Where the same authors publish multiple papers based on the same mechanism, generally only the first paper outlining the process is listed. Due to this, readers are recommended to search for other such papers in the literature. For each of the entries in the table the numbers attached correspond to the various mechanisms that the models employ, as listed in Table 5. From Table 3 it is clear that surface models rely on a variety of mechanisms combined together, while subsurface models generally rely on the emergence of twisted flux ropes where the filament forms in the dips of the flux rope or U-loop.

Surface mechanisms include: differential rotation; shear flows along a PIL (differential rotation is just a weak shear flow); and converging flows onto a PIL. Recent helioseismic observations by Hindman *et al.* (2006) show that underneath a well developed filament strong shear flows may be observed. However this was after the filament had formed and not during the formation process. Photospheric converging or shearing flows may be detected by local correlation tracking (cf. Magara, 1999; Roudier *et al.*, 2007; Roudier *et al.*, 2008). For some surface models diffusion of flux towards a PIL with subsequent cancellation plays the role of the converging flow. To produce an axial magnetic field consistent with observations, these flows generally have to occur in a specific order. In contrast to these surface motions, subsurface shear flows have also been employed. In both sets of models magnetic reconnection is generally required to reconfigure the fields; the reconnection may occur either above or below the surface.

Another feature common to both sets of models is flux emergence, but it is used in very different ways. For surface models, magnetic dipoles which emerge either untwisted or twisted are advected across the solar surface and reconfigured with other pre-existing coronal fields as discussed in the observations of Section 5.2.1. A key element in recent papers describing filament formation is that these dipoles are non-potential and include an initial magnetic helicity (Mackay and van Ballegooijen, 2005; Yeates *et al.*, 2008a). In contrast, flux emergence for subsurface models is presumed to occur in the form of twisted U-loops (Section 5.2.2).

Whilst it is impractical to describe each of the models listed in Tables 3 and 4 in detail, key elements may be considered from a few selected cases. The cases chosen are picked solely for illustrative purposes. The key feature of any sub-surface model is described in the papers by Low (1994) and Rust and Kumar (1994). For these models a filament is formed by a horizontal twisted magnetic flux tube in the convective layer of the Sun. Due to magnetic buoyancy the tube rises through the convective layer and emerges into the photosphere and corona, dragging cool dense material with it, to produce the mass of the prominence. Not every part of the tube has to rise at

the same time; subsequent rising parts could explain canceling magnetic features (see Figure 13 in Rust and Kumar, 1994). Such a feature has been considered in the numerical simulations of Gibson and Fan (2006) and Magara *et al.* (2008). In Magara *et al.* (2008) the flux rope is forced to rise into the solar atmosphere by imposed velocity fields. In other flux emergence simulations where the authors use only buoyancy and magnetic buoyancy instabilities, it is found that the axis of the flux rope does not rise through the photosphere (Moreno-Insertis, 2004; Archontis *et al.*, 2004; Archontis, 2008; Murray *et al.*, 2006; Galsgaard *et al.*, 2007). Although the axis and U-loops of the emerging tube do not rise to coronal heights, the process of flux emergence may still produce a coronal flux rope with dips. A flux rope may form through the reconnection of emerged sheared field lines that lie above the emerging tubes axis (Manchester *et al.*, 2004; Magara, 2006; Archontis and Török, 2008; Fan, 2009).

In contrast, one of the first surface models, by van Ballegooijen and Martens (1989), considers shearing motions acting on a coronal arcade in a bipolar configuration. The footpoints of the arcade are sheared in such a way that their separation increases and an axial field component is produced along the PIL (see Figures 29a and 29b). In principle this shear could be supplied by solar differential rotation or by other shear flows on the Sun. Next convergence, or diffusion of the flux towards the PIL, brings the foot points together where they may reconnect to produce, a long axial field line along the PIL and also a small loop which submerges through the surface (Figures 29c and 29d). Subsequent repetition of this process creates dipped magnetic field lines consistent with the topology required for filaments (Figures 29e and 29f).

In an extension to the van Ballegooijen and Martens (1989) model, Martens and Zwaan (2001) put forward a “head-to-tail” linkage model for the formation of filaments in a multiple bipolar configuration. A key element of their model was once again flux convergence and cancellation, which acts as the driver for reconnection between initially unconnected magnetic sources (also see Kuperus, 1996; Kuijpers, 1997)). In this scenario Martens and Zwaan (2001) describe how the filament channel and filament may be produced by the interaction of two dipoles, one older and more diffuse lying at a slightly higher latitude. As long as these sources satisfy Hale’s Polarity Law and Joy’s Law, then convergence and cancellation as a consequence of differential rotation, of the following polarity of the lower latitude dipole and lead polarity of the high latitude dipole, could result in a strongly sheared field line along the PIL. As with van Ballegooijen and Martens (1989) successive repetitions of this process would build up helical field structures. In addition, if multiple dipoles are involved over a range of latitudes large filaments extending over a full solar radius could be produced. While Martens and Zwaan considered the interaction of multiple dipoles in a conceptual model, Mackay *et al.* (2000); Mackay and van Ballegooijen (2001) carried out numerical simulations of a similar process.

Galsgaard and Longbottom (1999) consider a similar scenario with 3D numerical MHD simulations without the processes of flux cancellation and submergence. The interaction of two bipolar regions of flux, one which is older and more spread out than the other, is considered. The numerical simulations are based on the magnetic configurations discussed by Gaizauskas *et al.* (1997). In the model the two dipoles are initially connected to one another and the authors demonstrate how a current sheet may form in the coronal volume between the two dipoles as a result of flux convergence but no cancellation or submergence. Subsequent reconnections resulting from the convergence, then lift cool dense plasma over a number of pressure scale heights where it is able to form a region of high density plasma overlying the PIL. As

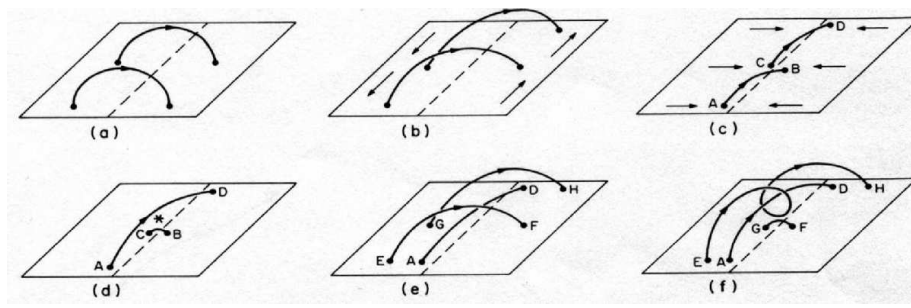


Fig. 29 Example of the formation of a filament's axial magnetic field through shearing motions, convergence, and reconnection as put forward by van Ballegooijen and Martens (1989).

part of this reconnection process dipped and sometimes helical field lines are formed with an upward tension force. Although the authors carried out the simulation with a simple isothermal atmosphere it remains one of the few full MHD simulations to consider both the origin of mass and of the shear in the magnetic field.

An alternative method of forming a similar magnetic structure was proposed by DeVore and Antiochos (2000) using a single bipolar configuration (also see Antiochos *et al.*, 1994). In this model, a bipolar magnetic field distribution is subjected to a strong shearing motion parallel to the PIL, however, no converging flow is applied. Once the footpoints of the field lines are sheared a distance comparable to the bipole width, an untwisted dipped magnetic configuration forms. The authors show that through further shearing of the dipped field lines the initially untwisted field may form a helical structure similar to that of van Ballegooijen and Martens (1989) through a two stage reconnection process. Therefore, in contrast to van Ballegooijen and Martens (1989) and Martens and Zwaan (2001), DeVore and Antiochos (2000) do not rely on convergence and cancellation of flux to produce the helical field.

From the discussion above it is clear that a wide range of theoretical models exist to explain the 3D magnetic structure of solar filaments. These models employ a variety of mechanisms. As will be discussed in Section 5.6 at the present time none of these models may be ruled out. However, by combining the observations discussed in Sections 5.1 and 5.2 it may be argued that some models are more relevant than others for the formation of large stable filaments (Quiescent and Intermediate) compared to Active Region filaments. A full discussion along with the presented hypothesis will be carried out in Section 5.6.

5.4 Models of Filament Merging

Numerical MHD simulations of the formation and interaction between filament segments were conducted by DeVore *et al.* (2005). The footpoint motions of the sheared arcade model (section 2.2.2) were applied to two adjacent, initially current-free, magnetic dipoles. As shown in Fig. 30, four possible combinations of chiralities (identical or opposite) and axial magnetic fields (aligned or opposed) between the participating filaments were considered. These four simulations exhibited substantially different degrees of linkage.

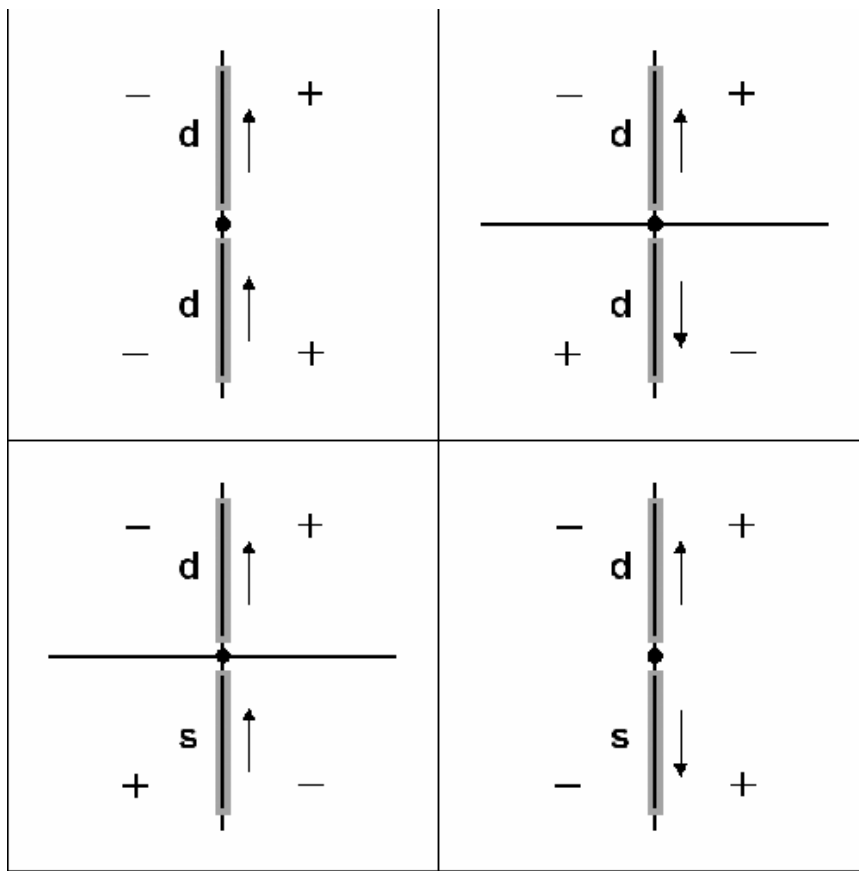


Fig. 30 Schematic diagram of the four possible configurations of interacting prominences: identical (top) or opposite (bottom) chiralities, and aligned (left) or opposed (right) axial magnetic fields. Black lines are the polarity inversion lines of the vertical field, whose direction is denoted by + (upward) and – (downward); shaded gray rectangles are the prominences, whose chiralities are indicated by **d** (dextral) and **s** (sinistral) and whose axial field directions are shown by the arrows; and filled black circles mark the prominence interaction regions.

When a single polarity inversion line is shared by the two bipoles, then identical chiralities necessarily imply aligned axial fields (Fig. 30, left). In this case, magnetic reconnection between field lines from both bipoles links the two initial prominence segments. Both acoustic and Alfvén waves propagate along these newly reconnected field lines, and should be capable of driving existing plasma condensations from one progenitor to another. As the shear increases, the volume between the original segments becomes filled with reconnected field lines, so that they gradually merge into a single filament. This multi-step merging mechanism couples photospheric shear, coronal reconnection, and relaxation to form a longer structure containing numerous dipped field lines where plasma can collect most easily (Aulanier *et al.*, 2006). Furthermore, the case of identical chiralities and aligned axial fields successfully reproduces the observations of filament merging (e.g., Martin *et al.*, 1994; Rust, 2001; Schmieder *et al.*, 2004; van Ballegooijen, 2004). A second model configuration (Fig. 30, upper right) also

contains a shared PIL, but opposite helicities and axial fields between the two segments. No merging ensues because little reconnection occurs between the filament segments, as is consistent with observations (e.g., Martin *et al.*, 1994; Rust, 2001; Deng *et al.*, 2002; Schmieder *et al.*, 2004).

When the initial topology instead is quadrupolar, so that the system contains two orthogonal PILs (Fig. 30, lower panels), then the converse relation holds between chirality and axial-field alignment. Reconstructions that form linking field lines now occur only between filament segments with opposite chiralities (Fig. 30, lower right), while reconnection between same-chirality segments only results in footpoint exchanges (Fig. 30, lower left). The results for quadrupolar topologies have not yet been verified with solar data because multipolar filament interactions are rarely observed. However, these key predictions present an important objective for future observational campaigns.

5.5 Origin of the Hemispheric Pattern of Filaments

Any model which tries to explain the origin of a filament's magnetic field must also explain why this magnetic field exhibits a hemispheric pattern. The first attempt through detailed numerical simulations was carried out by van Ballegooijen *et al.* (1998) who considered whether the surface flux transport effects of differential rotation, meridional flows and supergranular diffusion could in fact create the observed axial fields in filaments. By using observed magnetic flux distributions and initial coronal fields which were potential, they simulated the evolution of both the photospheric and coronal fields. They found that the above-mentioned surface effects when acting on potential fields create approximately equal numbers of dextral and sinistral channels in each hemisphere, in contradiction with observations. However, these authors did not take into account the force balance of the coronal plasma, and only considered statistical relationships between filament chirality and latitude.

In the more recent study of Mackay and van Ballegooijen (2005) the authors reconsider the origin of the hemispheric pattern through combined flux transport and magneto-frictional relaxation simulations. In these simulations as the flux transport effects shear up the photospheric field, the coronal field responds to these motions by relaxing to a non-linear force-free field equilibrium. In the simulations the authors consider an idealized setup of two initially isolated interacting dipoles. They perform a parameter study to determine the type of chirality formed along the PIL between the two dipoles, as the dipoles initial tilt angle (Joy's law) and helicity are varied. Therefore in contrast to the study of van Ballegooijen *et al.* (1998) they did not use initial potential fields. Through the simulations the authors demonstrate that surface diffusion can play a key role in canceling flux between the dipoles and building up an axial field through transporting helicity and sheared fields from the inner parts of the dipoles to the outer edges. The authors demonstrate that the hemispheric pattern of filaments may be explained through the observational properties of newly emerging dipoles such as, (1) their dominant tilt angles ($-10:30^\circ$, Wang and Sheeley (1989)), and (2) the dominant helicity that they emerge with in each hemisphere (Pevtsov *et al.*, 1995). In addition to this, a key feature of the simulations was that for the first time the occurrence of exceptions to the hemispheric pattern as a result of large positive dipole tilt angles and minority helicity could be quantified.

The results of Mackay and van Ballegooijen (2005) have been tested through a direct comparison between theory and observations by Yeates *et al.* (2007, 2008a). In this

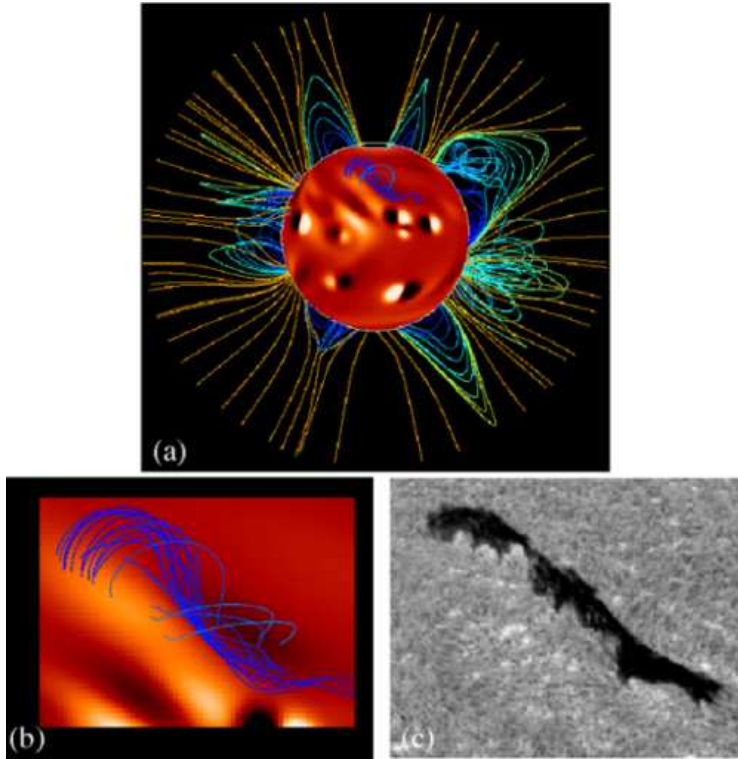


Fig. 31 Example of the comparison of theory and observations performed by Yeates *et al.* (2008a). (a) Example of the magnetic field distribution in the global simulation after 109 days of evolution, showing highly twisted flux ropes, weakly sheared arcades and near potential open fields. On the grey-scale image white/black represents positive/negative flux. (b) Close up view of a dextral flux rope lying above a PIL within the simulation. (c) BBSO H α image of the dextral filament observed at this location.

comparison Yeates *et al.* (2007, 2008a) develop a new technique to model the long term, global evolution of the Sun's magnetic field based on actual magnetogram observations. To carry out the comparison Yeates *et al.* (2007, 2008a) first consider H α observations from BBSO over a 6 month period and determine the location and chirality of 109 filaments (Yeates *et al.*, 2007) relative to the underlying magnetic flux. It should be noted that all of the filaments in the study lie below 65° latitude and no polar crown filaments were included since their chirality could not be determined. To determine the chirality for such filaments direct magnetic field measurements would be required. In the second stage they use combined magnetic flux transport and magneto-frictional relaxation simulations, where the simulations are based on actual photospheric magnetic distributions found on the Sun. They show that by including the process of flux emergence in the flux transport simulations they can reproduce to a high accuracy KP synoptic magnetograms from one Carrington Rotation to the next. Over the 6 month simulation to maintain the accuracy, 119 bipoles were emerged with their properties determined from observations. When the bipoles were emerged they were initially isolated from the surrounding fields and could contain either positive or negative helicity. Their subsequent interaction with neighboring field regions and transport across the

solar surface could then be followed. A key difference of these simulations from previous studies, was that they were run for the whole six month period without ever resetting the surface field back to that found in observations or the coronal field to potential. Therefore the simulations were able to consider long term helicity transport across the solar surface from low to high latitudes.

Using this technique Yeates *et al.* (2008a) carried out a direct one-to-one comparison of the chirality produced by the model with the observed chirality of the filaments at the exact location that the filaments were observed. An example of this can be seen in Figure 31. In Figure 31a the global field distribution can be seen after 108 days of evolution. The photospheric field distribution is given by the grey-scale image (white is positive flux, black is negative flux), while the lines denote the field lines of the non-linear force-free coronal field.

The coronal field can be seen to be made up of highly twisted flux ropes, slightly sheared coronal arcades and near potential open field lines. A zoomed in area of the central portion of this image can be seen in Figure 31b. In this figure a simulated flux rope structure can be seen where the axial field is of dextral chirality. For comparison the H α filament that formed at this location can be seen in Figure 31c. Through studying the barbs and applying a statistical technique, the filament was determined to be of dextral chirality so the chirality formed in the simulation matches that of the filament.

Through varying the sign and amount of helicity emerging within the dipoles, Yeates *et al.* (2008a) (see their Figure 5b) show that by emerging dominantly negative helicity in the northern hemisphere and positive in the southern, a 96% agreement can be found between the observations and simulations where the agreement is equally good for minority chirality filaments as well as for dominant chirality filaments. A key feature of the simulations is that a better agreement between the observations and simulations is found the longer the simulations are run. This indicates that the Sun has a long term memory of the transport of helicity from low to high latitudes. The reason for this high agreement is described in the paper of Yeates and Mackay (2009) where seven different mechanisms are involved in producing the observed chiralities. The results demonstrate that the combined effects of differential rotation, meridional flow, supergranular diffusion and emerging twisted active regions are sufficient to produce the observed hemispheric pattern of filaments.

5.6 Discussion of Filament Classification Schemes, Observations of Formation and Theoretical Models

So far we have discussed a number of properties of solar filaments. These properties have ranged from observations and locations of filament formation, to the wide variety of theoretical models used to explain them. In this sub-section we turn our attention to tying all of these observations together, by forming a unifying hypothesis, to quantify where and at what locations the mechanisms and models discussed in Section 5.3 are appropriate. We hope that this hypothesis will stimulate new observational studies to test it. We will first discuss the formation of large-stable filaments, namely those of the Intermediate and Quiescent filament type. After this we will consider Active Region filaments. A distinction is made as present observational evidence suggests that different mechanisms may apply.

5.6.1 Intermediate and Quiescent Filament Formation

From the observations of large-scale stable filaments discussed in Section 5.1.1 it can be seen that the majority of IF and QF (92%) form in magnetic configurations involving multiple bipole interactions. Very few (7%) form in single bipolar configurations along the internal PIL of the bipole. From this it is clear that it is rare to find either IF or QF in such single bipole configurations. Therefore, while none of the models listed in Table 3 or 4 can be ruled out, it is clear that those involving multiple bipole interactions are the most appropriate.

The question now turns to whether the IF and QF are formed due to surface motions acting on pre-existing coronal fields as Gaizauskas *et al.* (1997), Gaizauskas *et al.* (2001) and Wang and Muglach (2007) argue (Section 5.2.1) or whether they are due to sub-surface processes as argued by Lites and Low (1997) and Okamoto *et al.* (2009).

The answer to this may be alluded from the observations of Mackay *et al.* (2008) who showed (see their Figure 4) that only External Bipolar Region Filaments (EBR), those forming between two neighboring bipoles show any form of solar cycle dependence. Their numbers were found to increase in phase with the solar cycle, peaking around solar maximum and with more present in the declining phase of the cycle than in the rising phase. In contrast, Internal Bipolar Region Filaments (IBR) those forming in a single bipole, clearly showed no solar cycle dependence, with their number remaining at a low constant value throughout the cycle. If flux emergence in the form of flux ropes as used by subsurface models is key to the formation of IF and QF, then one would expect that IBR Filaments should show a strong solar cycle dependence. In addition they should be the dominant type. As more bipoles emerge on the Sun there is a much greater chance of having emerging flux ropes, hence more Internal Bipolar Region Filaments. As they are not the dominant type and exhibit no solar cycle dependence, another process other than flux rope emergence must be acting to form IBR filaments. An alternative explanation for the formation of IBR filaments, which from the observations discussed in this review generally occurs outside activity complexes, is that they may result from strong surface shearing motions or helicity injection and flux cancellation. Evidence for such shearing motions, at least in the later development of a filament, has recently been published by Hindman *et al.* (2006). This fits in with the single bipole model of DeVore and Antiochos (2000) where shear flows play a key role in the formation of the filament. In contrast, the alternate process of injection of helicity followed by cancellation has been described by Wang and Muglach (2007).

If flux rope emergence is unlikely to form IBR filaments, then it is extremely unlikely that such a process could apply to External Bipolar Region Filaments (EBR), the dominant type which tend to form between distinct bipoles after flux emergence has ended (see Section 5.2.1). Again, another process must be acting, one that is closely related to the amount of magnetic flux on the Sun.

The obvious choice deduced from the observations of Gaizauskas *et al.* (1997), Gaizauskas *et al.* (2001) and Wang and Muglach (2007) is the convergence between individual bipoles resulting in flux cancellation and reconnection, since the rates of convergence increase due to the increased rate of flux emergence during periods of high activity. During these periods of high activity the most widespread source of convergent flows would be the natural expansion of all bipolar pairs as soon as they emerge. If these processes are key in explaining the formation of filaments this would lead to an increase in the number of filaments forming between individual magnetic bipoles as activity increases. In addition, one expects more EBR Filaments after cycle maximum

than after cycle minimum; after maximum there is still a significant amount of magnetic flux on the Sun so that convergence and cancellation or magnetic reconnection can still take place.

Therefore, it may be argued that convergence leading to subsequent cancellation and reconnection (i.e., items 3, 4 and 10 in Table 5) are the mechanisms that result in the formation of the majority of large stable filaments found on the Sun, and that flux rope emergence does not play a major role for these filaments. The models in Table 3 which include these mechanisms appear to be the most appropriate. At the present time no further distinction can be made between these models. While this argument is put forward for EBR Filaments, it also applies to Diffuse Bipolar Region Filaments (DBR) because the flux patterns in which they form are a natural consequence of flux convergence and cancellation occurring over long periods of time.

Finally, for Internal/External Bipolar Region Filaments again convergence and cancellation/reconnection may apply but this time strong shear flows or helicity injection may again be applicable. While the above discussion applies to Intermediate and Quiescent filaments, in the next sub-section we consider Active Region filaments.

5.6.2 Active Region Filaments

We now turn our attention to Active Region filaments to consider their formation mechanism. Observations by Lites and Low (1997) and Okamoto et al. (2009) suggest that small-scale unstable active region filaments may be formed as the result of flux rope emergence dragging cool dense photospheric plasma into the corona. While this remains a possibility, most numerical simulations of emerging flux ropes fail to lift the axis and cool material of the original flux tube into the corona. Therefore it remains unclear whether such a process may occur. In contrast, many authors have shown that during the process of flux emergence, after the top of the flux rope has emerged, magnetic reconnection or helicity injection (Manchester *et al.*, 2004; Magara, 2006; Archontis and Török, 2008; Fan, 2009) may reconfigure the emerged coronal arcade to produce a secondary coronal flux rope. During the formation of the secondary flux rope the reconnection may then lift cool dense material to coronal heights. Therefore while emerging flux appears to be important for the formation of active region filaments a key element may still be atmospheric reconnection of pre-emerged fields. To resolve this issue many new observational studies are required.

From the argument presented above it appears that different formation mechanisms may apply to different types of filaments. Quiescent filaments and Intermediate filaments which mainly fall into the Exterior and Diffuse bipolar region types rely on surface effects acting on coronal fields. In contrast for active region filaments a strong possibility is the emergence of flux ropes or the formation of flux ropes during emergence as a result of coronal reconnection. Therefore it is useful to distinguish between IF and QF compared to ARF as they may have a different formation mechanism.

5.6.3 Future Observation of Filament Channels

The formation, structure, and evolution of solar filaments is an important part of our understanding of coronal physics and the behavior of magnetic fields as they are transported across the solar surface. New observational results show that surface motions acting on non-potential magnetic fields may play an integral part in the formation of

large-scale stable filaments while flux rope emergence may play a role for small, unstable active region filaments. In addition the large-scale hemispheric pattern of filaments may just be the result of surface effects redistributing the helicities of new emerging bipoles across the solar surface from low- to high- latitudes.

A better understanding of the formation of prominences requires multi-wavelength observations of prominences situated over a wide range of latitudes, from the active region belts up to the polar crowns. It is imperative to determine whether different formation mechanisms occur at different latitudes on the Sun. To distinguish this, spectral lines from $H\alpha$ to X-rays along with magnetic information are needed to provide full coverage of the wavelength ranges associated with the formation and structure of filaments. Before ordering up this large menu of observations, we must be able to use hindsight as to where and when a long-lived filament might form. Therefore, maintenance of existing synoptic data sets is a vital part of advanced studies of prominence formation.

6 Open Issues

The present review is focused on four aspects of solar prominences, namely, their magnetic structure, the dynamics of prominence plasma, prominence oscillations, and the formation and evolution of filament channels. Other aspects, such as the physical properties of prominence plasmas, spectroscopic methods used to measure these properties and non-LTE models are discussed in Paper I. In the following we outline several outstanding issues, and the observations and modeling required to resolve these issues. The ordering reflects the order of topics considered in the review and no attempt is made to prioritise them:

1. Why do different prominences have such different morphology (e.g., horizontal vs. vertical threads), and why do prominences/filaments look so different in different wavelengths? Current models do not readily explain such differences. What physical mechanism causes the observed thin thread structures and subsequently the gaps between individual threads? To resolve these issues, images with high spatial resolution of filaments and prominences obtained simultaneously are required at different wavelengths, including $H\alpha$, He I 10830 Å and He II 304 Å. These observations should track the same filament as it rotates across the solar disk and above the limb. Three-dimensional (3D) models of prominence threads should be developed (see Paper I).
2. What is the 3D magnetic structure of different types of prominences? In particular, what is the magnetic field orientation in filament barbs, and what is the relationship between the barbs and the evolving photospheric magnetic fields (e.g., parasitic polarities)? What is the effect of the evolving magnetic carpet on prominence magnetic structure? Are non-erupting filaments outside active regions suspended in detached flux ropes? Answering such questions will require spectro-polarimetric measurements of the magnetic fields in prominences at multiple heights including both measurements in prominences (using the Zeeman and Hanle effects) and in the photosphere/chromosphere below filaments. Techniques should be developed for modeling the evolution of filament magnetic structure in response to time-dependent photospheric boundary conditions, including the motions of discrete magnetic elements, flux emergence, and flux cancellation.

3. To what extent can vector field extrapolations from the photosphere or chromosphere be used to deduce magnetic fields within filaments? Answering this question requires photospheric and/or chromospheric vector field measurements, reliable NLFFF modeling to extrapolate the magnetic fields to larger heights, and verification that extrapolation results match the observed filament channel structures and magnetic fields.
4. How does the prominence plasma collect and evolve? What physical mechanisms are responsible for prominence plasma formation and dynamics? Which mechanisms best explain the observations of plasma distributions and flows? As different magnetic field models exhibit a different field structure (e.g. sheared arcade vs flux rope). What effect do these differences have on the distribution and dynamics of the plasma produced by the different plasma formation mechanisms. This requires simultaneous, high cadence, high spatial resolution observations of many spectral lines covering the full range of temperatures present in the solar atmosphere. An important goal is to obtain proper motion and Doppler shift information. Tests of the proposed mechanisms (§3) requires 3D MHD modeling, including relevant energy release, deposition, transport and loss processes.
5. What is the relationship between the observed signatures of the oscillations (spectral line shift, width, and intensity variation) and the physical properties of the MHD waves (velocity, magnetic field, temperature and density perturbations)? How are prominence oscillations excited and damped, and how does this affect the plasma energetics? Can prominence seismology be developed as a powerful diagnostic tool, too for example deduce the distribution and strength of the magnetic field in prominences? Solving this problem requires 2D observations of Doppler shifts with high spatial and temporal resolution, as well as independent estimates of key physical properties (e.g. densities and temperatures). Interpretation of these observations will require multi-dimensional modeling of wave propagation and damping in prominences, eventually incorporating wave excitation processes.
6. How are prominences heated, e.g., by waves (see point 5), shocks or other mechanisms? The temperatures in prominences are higher than the radiative equilibrium temperature of about 5000 K. We need high cadence observations in several spectral lines, and accurate modeling of the ionization state of the plasma and of radiative transport in optically thick spectral lines (see Paper I).
7. How are filament channels formed at all latitudes on the Sun? Currently, few observations of filament channel formation are available. What is the helicity distribution within activity complexes and how does it relate to filament channels? How is this helicity dispersed across the solar surface? This requires low cadence (hours) global observations, including the far side of the Sun over long periods of time (years): photospheric LOS magnetic field, H α , He I 10830 Å, He II 304 Å. Techniques should be developed to simulate the global-scale, long-term evolution of the coronal magnetic field, incorporating the observed distribution of emerged magnetic flux and helicity.
8. How and at what locations along the PILs do filament channels form within active regions and activity complexes? Answering this question requires high-cadence, high-resolution observations of active regions and activity complexes in H α , EUV lines, and LOS magnetic field. To elucidate the role of subsurface processes (§5.3 and §5.6), the emergence of twisted flux ropes should be modeled self-consistently.
9. What is the magnetic structure of polar crown prominences? Do they have the same chirality as mid-latitude prominences in the same hemisphere? If they exhibit

a hemispheric pattern what is the cause of it ? This requires spatially resolved, synoptic measurements of prominence magnetic fields using the Hanle effect. Such observations have not been carried out since the 1980's. Do sub-surface processes play a role in the formation of polar crown prominences? To answer this question requires out-of-ecliptic observations of photospheric magnetic fields (LOS component) and local helio-seismology to determine subsurface flows near the polar crowns.

10. What can filaments and prominences tell us about the distribution of magnetic helicity across the solar surface and subsequently the solar dynamo? Attacking this fundamental issue requires the development of 3D dynamo models that include the distribution and transport of magnetic helicity. The results of such dynamo models should be compared with observations of the helicity in active regions and filament channels on the quiet Sun.

These issues can be addressed by combining spectral and imaging observations from ground- and space-based instruments. Some of the goals may be achieved with currently available resources, but others will require new missions. Planners of future space missions are encouraged to take the above observational requirements into account.

Acknowledgements The authors would like to thank ISSI (Bern) for support of the team "Spectroscopy and Imaging of Quiescent and Eruptive Prominences from Space." They also would like to thank their teammates for the nice working atmosphere and the lively discussions. Financial support by the European Commission through the European Solar Magnetism Network (HPRN-CT-2002-00313) and the SOLAIRE Network (MTRN-CT-2006-035484) is gratefully acknowledged. JK would like to thank S. Antiochos, C.R. DeVore and J.A. Klimchuk for their collaboration on the thermal non-equilibrium studies discussed in section 3. JLB would like to acknowledge I. Arregui, M. Carbonell, A. Díaz, P. Forteza, R. Oliver, R. Soler and J. Teradas, colleagues from the Mallorca Solar Physics Group, for their contributions to the research reported in section 4. JLB would also like to acknowledge the financial support received from the Spanish Ministry of Science and Innovation under grant AYA2006-07637, FEDER funds, and from the Conselleria de Economia, Hisenda i Innovació under grant PCTIB-2005GC3-03. DHM would like to thank the UK STFC for their financial support.

This paper is based on data from many solar observatories. Figure 6 is based on observations from the THÉMIS, which was built by the INSU/CNRS (France) and the CNR (Italy), and is installed at the International Observatory of the Canary Islands (Tenerife, Spain), which is operated by the Instituto de Astrofísica de Canarias. Figures 23, 24 and 25 used data from the Ottawa River Solar Observatory of the National Research Council (Canada), and from the National Solar Observatory (NSO), which is supported by the National Science Foundation (NSF) and by NASA. SOHO is a mission operated by ESA and NASA. Hinode is a Japanese mission developed and launched by ISAS/JAXA, collaborating with NAOJ as a domestic partner, NASA and STFC(UK) as international partners.

References

P. Ambrož, A. Schroll, *A&A* 381, 300 (2002)
 C.-H. An, *ApJ* 298, 409 (1985)
 S.K. Antiochos, R.B. Dahlburg, J.A. Klimchuk, *ApJ* 420, L41 (1994)
 S.K. Antiochos, J.A. Klimchuk, *ApJ* 378, 372 (1991)
 S.K. Antiochos, P.J. MacNeice, D.S. Spicer, J.A. Klimchuk, *ApJ* 512, 985 (1999)
 S.K. Antiochos, P.J. MacNeice, D.S. Spicer, *ApJ* 536, 494 (2000)
 U. Anzer, P. Heinzel, *A&A* 404, 1139 (2003)
 V. Archontis, *J. Geophys. Res.* 113, 12422 (2008)

Archontis, V., Török, T. , A&A , 492, L35 (2008)

V. Archontis, F. Moreno-Insertis, K. Galsgaard, A. Hood, E. O'Shea, A&A , 426, 1047 (2004)

I. Arregui, J. Terradas, R. Oliver, J. L. Ballester, ApJ 682, L141 (2008)

M. Aschwanden, C.J. Schrijver, D. Alexander, ApJ 550, 1036 (2001)

G. Aulanier, P. Démoulin, A&A 329, 1125 (1998)

G. Aulanier, P. Démoulin, A&A , 402, 769 (2003)

G. Aulanier, P. Démoulin, N. Mein, L. van Driel-Gesztelyi, P. Mein, B. Schmieder, A&A 342, 867 (1999)

G. Aulanier, P. Démoulin, L. van Driel-Gesztelyi, P. Mein, C. Deforest, A&A 335, 309 (1998)

G. Aulanier, C.R. DeVore, S.K. Antiochos, ApJ 567, L97 (2002)

G. Aulanier, C.R. DeVore, S.K. Antiochos, ApJ 646, 1349 (2006)

G. Aulanier, B. Schmieder, A&A 386, 1106 (2002)

G. Aulanier, N. Srivastava, N., S.F. Martin, ApJ 543, 447 (2000)

Babcock, H. W., & Babcock, H. D., ApJ , 121, 349 (1955)

K.S. Balasubramaniam, L. Milano, S.L. Keil, 1998 ASP Conf. Series, vol. 140 (Astron. Soc. of the Pacific, San Francisco, 2005), 189

D. Banerjee, R. Erdélyi, R. Oliver, E. O'Shea, Sol. Phys. 246, 3 (2007)

E.E. Benevolenskaya, in *Large-scale Structures and their Role in Solar Activity*, ed. by K. Sankarasubramanian, M. Penn, A. Pevtsov. ASP Conf. Series, vol. 346 (Astron. Soc. of the Pacific, San Francisco, 2005), p. 129

T.E. Berger, R.A. Shine, G.L. Slater, T.D. Tarbell, A.M. Title, T.J. Okamoto, K. Ichimoto, Y. Katsukawa, Y. Suematsu, S. Tsuneta, B.W. Lites, T. Shimizu, ApJ 676, L89 (2008)

P.N. Bernasconi, D.M. Rust, D. Hakim, Sol. Phys. 228, 97 (2005)

M. Bianda, R. Ramelli, J. Trujillo Bueno, J.O. Stenflo, in *Solar Polarization 4*, ed. by R. Casini, B.W. Lites. ASP Conf. Series, vol. 358 (Astron. Soc. of the Pacific, San Francisco, 2006), p. 454

S. Blanco, K. Bocchialini, A. Costa, M. Domenech, M. Rovira, J.C. Vial, Sol. Phys. 186, 281 (1999)

M.G. Bobra, A.A. van Ballegooijen, E.E. DeLuca, ApJ 672, 1209 (2008)

V. Bommier, J.-L. Leroy, in *New Perspectives on Solar Prominences*, IAU Colloq. 167, ed. by D. Webb, D. Rust, B. Schmieder. ASP Conf. Series, vol. 150 (Astron. Soc. of the Pacific, San Francisco, 1998), p. 434

A. Canou, T. Amari, V. Bommier, B. Schmieder, G. Aulanier, H. Li, ApJ 693, L27 (2009)

M. Carbonell, R. Oliver, J.L. Ballester, New Astronomy 14, 277 (2009)

R. Casini, A. López Ariste, S. Tomczyk, B.W. Lites, ApJ 598, 67 (2003)

R. Casini, R. Bevilacqua, A. López Ariste, ApJ 622, 1265 (2005)

J. Chae, ApJ 560, L95 (2001)

J. Chae, ApJ , 584, 1084 (2003)

J. Chae, K. Ahn, E.-K. Lim, G.S. Choe, T. Sakurai, ApJ 689, L73 (2008)

J. Chae, C. Denker, T.J. Spirock, H. Wang, P.R. Goode, Sol. Phys. 195, 333 (2000)

J. Chae, Y.-J. Moon, Y.-D. Park, ApJ , 626, 574 (2005)

J. Chae, Y.-J. Moon, H. Wang, H.S. Yun, Sol. Phys. , 207, 73 (2002)

J. Chae, H. Wang, J. Qiu, P.R. Goode, L. Strous, H.S. Yun, ApJ 560, 476 (2001)

M. Collados, J. Trujillo Bueno, A. Asensio Ramos, in *Solar Polarization Workshop 3*, ed. by J. Trujillo Bueno & J. Sánchez Almeida. ASP Conf. Series, vol. 236 (Astron.

Soc. of the Pacific, San Francisco, 2003), p. 468

d'Azambuja, L. and d'Azambuja, M., *Ann. Obs. Paris-Meudon* 6, 7 (1948)

R.B. Dahlburg, S.K. Antiochos, J.A. Klimchuk, *ApJ* 495, 485 (1998)

Y. Deng, Y. Lin, B. Schmieder, O. Engvold, *Sol. Phys.* 209, 153 (2002)

Y. Deng, B. Schmieder, O. Engvold, E. DeLuca, L. Golub, *Sol. Phys.* 195, 347 (2000)

B. De Pontieu, S. W. McIntosh, M. Carlsson, V.H. Hansteen, T.D. Tarbell, *et al.*, *Science*, 318, 1574 (2007)

C.R. DeVore, S.K. Antiochos, *ApJ* 539, 954 (2000)

C.R. DeVore, S.K. Antiochos, G. Aulanier, *ApJ* , 629, 1122 (2005)

A.J. Díaz, R. Oliver, J.L. Ballester, *ApJ* 580 550 (2002)

A.J. Díaz, R. Oliver, J.L. Ballester, *A&A* 440 1167 (2005)

A.J. Díaz, R. Oliver, R. Erdélyi, J.L. Ballester, *A&A* 379, 1083 (2001)

J. Dudik, G. Aulanier, B. Schmieder, V. Bommier, T. Roudier, *Sol. Phys.* 248, 29 (2008)

O. Engvold, in *Dynamics and Structure of Quiescent Solar Prominences*, ed. by E.R. Priest (Kluwer, Dordrecht, 1989), p. 47

O. Engvold, in *New Perspectives on Solar Prominences*, IAU Colloq. 167, ed. by D. Webb, D. Rust, B. Schmieder. ASP Conf. Series, vol. 150 (Astron. Soc. of the Pacific, San Francisco, 1998), p. 23

O. Engvold, in *Proc. of Workshop on MHD Waves in Astrophysical Plasmas*, ed. by J. L. Ballester, B. Roberts (Universitat de les Illes Balears, Spain, 2001), pp. 123-131

O. Engvold, in *Multiwavelength Investigations of Solar Activity*, ed. by A. Stepanov, E. Benevolenskaya, A.G. Kosovichev (Cambridge University Press, UK, 2004), pp. 187-194

O. Engvold, in *Waves and Oscillations in the Solar Atmosphere: Heating and Magneto-Seismology*, ed. by R. Erdélyi, C.A. Mendoza-Briceño (Cambridge University Press, UK, 2008), pp. 152-157

O. Engvold, E. Jensen, *Sol. Phys.* , 52, 37 (1977)

S. Eto, H. Isobe, N. Narukage, A. Asai, A., T. Morimoto, B. Thompson, S. Yashiro, T. Wang, R. Kitai, H. Kurokawa, K. Shibata, *PASJ* 54, 481 (2002)

Y. H. Fan, *ApJ* 554, L111 (2001)

Y.-H. Fan, S.E. Gibson, *ApJ* 609, 1123 (2004)

Y.-H. Fan, S.E. Gibson, *ApJ* 641, L149 (2006)

Fan, Y., *ApJ* , 697, 1529 (2009)

V.C.A. Ferraro, C. Plumpton, *An Introduction to Magneto- fluid mechanics* (Oxford University Press, UK, 1961)

P. Forteza, R. Oliver, J.L. Ballester, *A&A* , 492, 223 (2008)

P. Forteza, R. Oliver, J.L. Ballester, M. Khodachenko, *A&A* 461, 731 (2007)

P. Foukal, *Sol. Phys.* 19, 59 (1971a)

P. Foukal, *Sol. Phys.* , 20, 298 (1971b)

C. Foullon, E. Verwichte, V. Nakariakov, *A&A* 427, L5 (2004)

Furth, H. P., Killeen, J., & Rosenbluth, M. N., *Physics of Fluids*, 6, 459 (1963)

V. Gaizauskas, in *New Perspectives of Solar Prominences*, IAU Colloq. 167, ed. by D. Webb, D. Rust, B. Schmieder. ASP Conf. Series, vol. 150 (Astron. Soc. of the Pacific, San Francisco, 1998), p. 257

V. Gaizauskas, *Sol. Phys.* 211, 179 (2002)

V. Gaizauskas, *ApJ* 686, 1432 (2008)

V. Gaizauskas, K.L. Harvey, J.W. Harvey, C. Zwaan, *ApJ* 265, 1056 (1983)

V. Gaizauskas, D.H. Mackay, K.L. Harvey, *ApJ* 558, 888 (2001)

V. Gaizauskas, J.B. Zirker, C. Sweetland, A. Kovacs, ApJ 479, 448 (1997)
 V. Gaizauskas, C. Zwaan, BAAS 29, 902 (1997)
 K. Galsgaard, A.W. Longbottom, ApJ 510, 444 (1999)
 K. Galsgaard, V. Archontis, F. Moreno-Insertis, A.W. Hood, ApJ 666, 516 (2007)
 S.E. Gibson, Y. Fan, C. Mandrini, G. Fisher, P. Démoulin, ApJ 617, 600 (2004)
 S.E. Gibson, Y. Fan, J. Geophys. Res. , 111, Issue A12, CiteID A12103 (2006)
 H.R. Gilbert, A.G. Daou, D. Young, D. Tripathi, D. Alexander, ApJ 685, 629 (2008)
 H.R. Gilbert, V. Hansteen, T.E. Holzer, ApJ 577, 464 (2002)
 H.R. Gilbert, G. Kilper, D. Alexander, ApJ 671, 978 (2007)
 M. Goossens, J.V. Hollweg, T. Sakurai, Sol. Phys. 138, 233 (1992)
 M. Goossens, M.S. Ruderman, J.V. Hollweg, Sol. Phys. 157, 75 (1995)
 S. Gunár, P. Heinzel, U. Anzer, B. Schmieder, A&A 490, 307 (2008)
 S. Gunár, P. Heinzel, B. Schmieder, P. Schwartz, U. Anzer, A&A 472, 929 (2007)
 K.L. Harvey, H.P. Jones, C.J. Schrijver, M. Penn, Sol. Phys. 190, 35 (1999)
 P. Heinzel, U. Anzer, A&A 375, 1090 (2001)
 P. Heinzel, U. Anzer, ApJ 643, L65 (2006)
 P. Heinzel, U. Anzer, S. Gunár, A&A 442, 331 (2005)
 P. Heinzel, B. Schmieder, F. Farnik, P. Schwartz, N. Labrosse, P. Kotrc, U. Anzer, G. Molodij, A. Berlicki, E. DeLuca, L. Golub, T. Watanabe, T. Berger, ApJ 686, 1383 (2008)
 P. Heinzel, B. Schmieder, K. Tziotziou, ApJ 561, L223 (2001a)
 P. Heinzel, B. Schmieder, J.-C. Vial, P. Kotrc, A&A 370, 281 (2001b)
 B.W. Hindman, D.A. Haber, J. Toomre, ApJ 653, 725 (2006)
 T. Hirayama, Sol. Phys. 100, 415 (1985)
 J.V. Hollweg, G. Yang, J. Geophys. Res. 93, 5423 (1988)
 Hood, A., & Anzer, U., Sol. Phys. , 115, 61 (1988)
 Hood, A. W., & Anzer, U., Sol. Phys. , 126, 117 (1990)
 C.L. Hyder, ApJ 141, 1374 (1965)
 J. Jing, J. Lee, T.J. Spirock, H. Wang, Sol. Phys. 236, 97 (2006)
 J. Jing, J. Lee, T.J. Spirock, Y. Xu, H. Wang, ApJ 584, L103 (2003)
 P.S. Joarder, B. Roberts, A&A 277, 225 (1993)
 H.P. Jones, Lecture Notes in Computer Science, 3215, 433 (2004)
 J.T. Karpen, S.K. Antiochos, ApJ 676, 658 (2008)
 J.T. Karpen, S.K. Antiochos, M. Hohensee, J.A. Klimchuk, P.J. MacNeice, ApJ 553, L85 (2001)
 J.T. Karpen, S.K. Antiochos, J.A. Klimchuk, ApJ 637, 531 (2006)
 J.T. Karpen, S.K. Antiochos, J.A. Klimchuk, P.J. MacNeice, ApJ 593, 1187 (2003)
 J.T. Karpen, S.K. Antiochos, S.E. Tanner, C.R. DeVore, ApJ 635, 1319 (2005)
 Keil, S., Balasubramaniam, K., Milano, L., Bayliss, A., Jones, J., & Clark, J. 1999,
 High Resolution Solar Physics: Theory, Observations, and Techniques, 183, 540
 D.C. Kendall, C. Plumpton, in *Magnetohydrodynamics with Hydrodynamics, vol. I* (Pergamon Press, 1964)
 M.L. Khodachenko, T.D. Arber, H.O. Rucker, A. Hanslmeier, A&A 422, 1073 (2004)
 M.L. Khodachenko, H.O. Rucker, R. Oliver, T.D. Arber, A. Hanslmeier, Adv. Space Res. 37, 447 (2006)
 K.O. Kiepenheuer, in *The Sun*, ed. by G.P. Kuiper (Univ. of Chicago Press, Chicago, 1953), p. 322
 G.. Kilper, H. Gilbert, D. Alexander, ApJ , submitted (2009)
 R. Kippenhahn, A. Schlüter, Z. für Astrophysik 43, 36 (1957)

J.A. Klimchuk, Sol. Phys. 234, 41 (2006)

C.M. Korendyke, A. Vourlidas, J.W. Cook, K.P. Dere, R.A. Howard, J.S. Morrill, J.D. Modes, N.E. Moulton, D.G. Socker, Sol. Phys. , 200, 63 (2001)

J. Kubota, A. Uesugi, PASJ 38, 903 (1986)

T.A. Kucera, E. Landi, ApJ 645, 1525 (2006)

T.A. Kucera, M. Tovar, B. De Pontieu, Sol. Phys. 212, 81 (2003)

M. Kuperus, Sol. Phys. 169, 349 (1996)

M. Kuperus, M.A. Raadu, A&A 31, 189 (1974)

J. Kuijpers, ApJ 489, L201 (1997)

N. Labrosse, *et al.*, in preparation (2009), paper I

J.M. Laming, U. Feldman, ApJ 403, 434 (1993)

J.E. Leake, T.D. Arber, A&A 450, 2 (2006)

Léger, L., & Paletou, F., A&A , 498, 869 (2009)

J.-L. Leroy, in *Dynamics and Structure of Quiescent Solar Prominences*, ed. by E.R. Priest (Kluwer, Dordrecht, 1989), p. 77

J.-L. Leroy, V. Bommier, S. Sahal-Brechot, Sol. Phys. 83, 135 (1983)

J.-L. Leroy, V. Bommier, S. Sahal-Brechot, A&A 131, 33 (1984)

H. Lin, M.J. Penn, J.R. Kuhn, ApJ 493, 978 (1998)

Y. Lin, Ph.D. Thesis (University of Oslo, Norway, 2004)

Y. Lin, O. Engvold, L. Rouppe van der Voort, M. van Noort, Sol. Phys. 246, 65 (2007)

Y. Lin, O. Engvold, L. Rouppe van der Voort, J.E. Wiik, T.E. Berger, Sol. Phys. 226, 239 (2005a)

Y. Lin, O. Engvold, J.E. Wiik, Sol. Phys. 216, 109 (2003)

Y. Lin, S.F. Martin, O. Engvold, in *Subsurface and Atmospheric Influences of Solar Activity*, ed. by R. Howe, R.W. Komm, K.S. Balasubramaniam, G.J.D. Petrie. ASP Conf. Series, vol. 333 (Astron. Soc. of the Pacific, San Francisco, 2008a), p. 235

Y. Lin, S.F. Martin, O. Engvold, L.H.M. Rouppe van der Voort, M. van Noort, Adv. Space Res. 42, 803 (2008b)

Y. Lin, J.E. Wiik, O. Engvold, L. Rouppe van der Voort, Z. Frank, Sol. Phys. 227, 283 (2005b)

R. Lionello, Z. Mikić, J.A. Linker, T. Amari, ApJ 581, 718 (2002)

B.W. Lites, ApJ 622, 1275 (2005)

B.W. Lites, B.C. Low, Sol. Phys. 174, 91 (1997)

Y.E. Litvinenko, Sol. Phys. 196, 369 (2000)

Y.E. Litvinenko, J. Chae, S.-Y. Park, ApJ 662, 1302 (2007)

Y.E. Litvinenko, S.F. Martin, Sol. Phys. 190, 45 (1999)

Y.E. Litvinenko, M.S. Wheatland, ApJ 630, 587 (2005)

Y. Liu, H. Kurokawa, K. Shibata, ApJ 631, L97 (2005)

S.H.B. Livi, J. Wang, S.F. Martin, Aust. J. Phys. 38, 855 (1985)

A. López Ariste, G. Aulanier, in *The Physics of Chromospheric Plasmas*, ed. by P. Heinzel, I. Dorotovic, R.J. Rutten. ASP Conf. Series, vol. 368 (Astron. Soc. of the Pacific, San Francisco, 2007), p. 291

A. López Ariste, G. Aulanier, B. Schmieder, A. Sainz Dalda, A&A 456, 725 (2006)

A. López Ariste, R. Casini, ApJ 575, 529 (2002)

A. López Ariste, R. Casini, ApJ 528, L51 (2003)

A. López Ariste, R. Casini, F. Paletou, S. Tomczyk, B.W. Lites, M. Semel, E. Landi Degl'Innocenti, J. Trujillo Bueno, K.S. Balasubramaniam, ApJ 621, L145 (2005)

B.C. Low, Physics of Plasmas, 1, 1684 (1994)

B.C. Low, J.R. Hundhausen, ApJ 443, 818 (1995)

B.C. Low, G.J.R. Petrie, ApJ 626, 551 (2005)
 B.C. Low, M. Zhang, ApJ 564, L53 (2002)
 D.H. Mackay, V. Gaizauskas, Sol. Phys. 216, 121 (2003)
 D.H. Mackay, V. Gaizauskas, G.J. Rickard, E.R. Priest, ApJ 486, 534 (1997)
 D.H. Mackay, V. Gaizauskas, A.A. van Ballegooijen, ApJ 544, 1122 (2000)
 D.H. Mackay, V. Gaizauskas, A.R. Yeates, Sol. Phys. 248, 51 (2008)
 D.H. Mackay, K. Galsgaard, Sol. Phys. 198, 289 (2001)
 D.H. Mackay, A.W. Longbottom, E.R. Priest, Sol. Phys. 185, 87 (1999)
 D.H. Mackay, E.R. Priest, V. Gaizauskas, A.A. van Ballegooijen, Sol. Phys. 180, 299 (1998)
 D.H. Mackay, A.A. van Ballegooijen, ApJ 560, 445 (2001)
 D.H. Mackay, A.A. van Ballegooijen, ApJ 621, L77 (2005)
 D.H. Mackay, A.A. van Ballegooijen, ApJ 641, 577 (2006)
 D.H. Mackay, *et al.*, in preparation (2009)
 T. Magara, ApJ 653, 1499 (2006)
 T. Magara, S.K. Antiochos, C.R. DeVore, M.G. Linton, ApJ, submitted (2008)
 T. Magara, R. Kitai, ApJ 524, 469 (1999)
 J.-M. Malherbe, in *Dynamics and Structure of Quiescent Solar Prominences*, ed. E.R. Priest (Kluwer, Dordrecht, 1989), p. 115
 J.-M. Malherbe, E.R. Priest, A&A 123, 80 (1983)
 W. Manchester IV, T. Gombosi, D. DeZeeuw, Y. Fan, ApJ 610, 588 (2004)
 P.C. Martens, C. Zwaan, ApJ 538, 872 (2001)
 S.F. Martin, Sol. Phys. 31, 3 (1973)
 S.F. Martin, Sol. Phys. 182, 107 (1998)
 S.F. Martin, R. Bilimoria, P.W. Tracadas, in *Solar Surface Magnetism*, ed. by R.J. Rutten, C.J. Schrijver (Kluwer, Dordrecht, 1994), p. 303
 S.F. Martin, C.R. Echols, in *Solar Surface Magnetism*, ed. by R.J. Rutten, C.J. Schrijver (Kluwer, Dordrecht, 1994), p. 339
 S.F. Martin, Y. Lin, O. Engvold, Sol. Phys. 250, 31 (2008)
 S.F. Martin, S.H.B. Livi, J. Wang, Aust. J. Phys. 38, 929 (1985)
 S.F. Martin, B. Marquette, R. Bilimoria, in *The Solar Cycle*, ed. by K. Harvey (National Solar Observatory, USA, 1992), p. 53
 S.F. Martin, A.H. McAllister, in *Magnetodynamic Phenomena in the Solar Atmosphere - Prototypes of Stellar Magnetic Activity*, ed. by Y. Uchida, T. Kosugi, H.S. Hudson (Kluwer, Dordrecht, 1996), p. 495
 M.J. Martres, R. Michard, I. Soru-Iscovici, A&A 29, 249 (1966)
 A.H. McAllister, D.H. Mackay, S.F. Martin, Sol. Phys. 211, 155 (2002)
 P.S. McIntosh, B.A.A.S. 34, 737 (2002)
 R.R. McMath, E. Pettit, ApJ 88, 244 (1938)
 C. Mercier, J. Heyvaerts, A&A 61, 285 (1977)
 L. Merenda, J. Trujillo Bueno, E. Landi Degl'Innocenti, M. Collados, ApJ 642 (2006)
 M. Minarovjech, M. Rybansky, V. Rusin, Sol. Phys. 177, 357 (1998)
 Y. Mok, J.F. Drake, D.D. Schnack, G. Van Hoven, ApJ 359, 228 (1990)
 R. Molowny-Horas, E. Wiehr, H. Balthasar, R. Oliver, J. L. Ballester, in *JOSO Annual Report '98* (Astronomical Institute Tatranska Lomnica, Slovakia, 1999), p. 126
 F. Moreno-Insertis, Astrophysics & Space Science 292, 587 (2004)
 Z. Mouradian, I. Soru-Escaut, A&A 290, 279 (1994)
 D.A.N. Müller, A. De Groof, V.H. Hansteen, H. Peter, A&A 436, 1067 (2005)
 D.A.N. Müller, V.H. Hansteen, H. Peter, A&A 411, 605 (2003)

M.J. Murray, A.W. Hood, F. Moreno-Insertis, K. Galsgaard, V. Archontis, A&A 460, 909 (2006)

Z. Ning, W. Cao, T. J. Okamoto, K. Ichimoto, Z. Q. Qu, A&A , 499, 595 (2009)

L. Ofman, J. Klimchuk, J. Davila, ApJ 493, 474 (1998)

T.J. Okamoto, H. Nakai, A. Keiyama, N. Narukage, S. Ueno, R. Kitai, H. Kurokawa, K. Shibata, ApJ 608, 1124 (2004)

T.J. Okamoto, S. Tsuneta, T.E. Berger, K. Ichimoto, Y. Katsukawa, B.W. Lites, S. Nagata, K. Shibata, T. Shimizu, R.A. Shine, Y. Suematsu, T.D. Tarbell, A.M. Title, Science, 318, 1577 (2007)

T.J. Okamoto, S. Tsuneta, B.W. Lites, M. Kubo, T. Yokoyama, T.E. Berger, *et al.*, ApJ 673, L215 (2008)

R. Oliver, in *Proc. 9th European Meeting on Solar Physics, "Magnetic Fields and Solar Processes"*, ed. A. Wilson (European Space agency, 1999), ESA SP-448, p. 425

Okamoto, T. J., et al., ApJ , 697, 913 (2009)

R. Oliver, J.L. Ballester, Sol. Phys. 206, 45 (2002)

R. Oliver, V.M. Cadez, M. Carbonell, J.L. Ballester, A&A 351, 733 (1999)

F. Paletou, in *SF2A-2008: Proc. of the Annual meeting of the French Society of Astronomy and Astrophysics*, ed. by C. Charbonnel, F. Combes, R. Samadi (2008), p. 559. Available online at <http://proc.sf2a.asso.fr>

F. Paletou, G. Aulanier, in *Solar Polarization Workshop 3*, ed. by J. Trujillo Bueno & J. Sánchez Almeida, ASP Conf. Series, vol. 236 (Astron. Soc. of the Pacific, San Francisco, 2003), p. 458

F. Paletou, A. López Ariste, V. Bommier, M. Semel, A&A 375, L39 (2001)

S. Patsourakos, J.-C. Vial, Sol. Phys. 208, 253 (2002)

H. Pecseli, O. Engvold, Sol. Phys. 194, 73 (2000)

A.A. Pevtsov, K.S. Balasubramaniam, J.W. Rogers, ApJ 595, 500 (2003)

A.A. Pevtsov, R.C. Canfield, T.R. Metcalf, ApJ 440, L109 (1995)

S.B. Pikel'ner, Sol. Phys. 17, 44 (1971)

G.W. Pneuman, Sol. Phys. 88, 219 (1983)

A.I. Poland, J.T. Mariska, Sol. Phys. 104, 303 (1986)

G. Pouget, K. Bocchialini, J. Solomon, A&A 450, 1189 (2006)

E.R. Priest, A.W. Hood, U. Anzer, ApJ 344, 1010 (1989)

E.R. Priest, A.A. van Ballegooijen, D.H. Mackay, ApJ 460, 530 (1996)

R. Ramelli, M. Bianda, J. Trujillo Bueno, L. Meranda, J.O. Stenflo in *Solar Polarization 4*, ed. by R. Casini, B.W. Lites, ASP Conf. Series, vol. 358 (Astron. Soc. of the Pacific, San Francisco, 2006), p. 471

H.E. Ramsey, S.F. Smith, Astron. J. 71, 197 (1966)

S. Régnier, T. Amari, A&A 425, 345 (2004)

S. Régnier, T. Amari, E. Kersalé, A&A 392, 1119 (2002)

S. Régnier, R.C. Canfield, A&A 451, 319 (2006)

S. Régnier, E.R. Priest, A&A 468, 701 (2007)

S. Régnier, J. Solomon, J.-C. Vial, A&A 376, 292 (2001)

S. Rondi, Th. Roudier, G. Molodij, V. Bommier, S. Keil, P. Sütterlin, J.M. Malherbe, M. Meunier, B. Schmieder, P. Maloney, A&A 467, 1289 (2007)

T. Roudier, M. Svanda, N. Meunier, S. Keil, M. Rieutord, J.M. Malherbe, S. Rondi, G. Molodij, V. Bommier, B. Schmieder, A&A 480, 255 (2008)

G. Roumeliotis, R. Moore, ApJ 416, 386 (1993)

M. Ruderman, B. Roberts, ApJ 577, 475 (2002)

D.M. Rust, ApJ 150, 313 (1967)

D.M. Rust, J. Geophys. Res. 106, A11, 25075 (2001)

D.M. Rust, A. Kumar, Sol. Phys. 155, 69 (1994)

K. Saito, C.L. Hyder, Sol. Phys. 5, 61 (1968)

K. Saito, E. Tandberg-Hanssen, Sol. Phys. 31, 105 (1973)

T. Sakurai, M. Goossens, J.V. Hollweg, Sol. Phys. 133, 227 (1991)

B. Schmieder, G. Aulanier, P. Mein, A. López Ariste, Sol. Phys. 238, 245 (2006)

B. Schmieder, V. Bommier, T. Kitai, T. Matsumoto, T. Ishii, M. Hagino, H. Li, L. Golub, Sol. Phys. 247, 321 (2008)

B. Schmieder, S. Gunar, P. Heinzel, U. Anzer, Sol. Phys. 241, 53 (2007)

B. Schmieder, N. Mein, Y. Deng, C. Dumitrache, J.M. Malherbe, J. Staiger, E.E. DeLuca, Sol. Phys. 223, 119 (2004)

B. Schmieder, M.A. Raadu, J.E. Wiik, A&A 252, 353 (1991)

B. Schmieder, K. Tziotziou, P. Heinzel, A&A 401, 361 (2003)

B. Schmieder, R. Chandra, A. Berlicki, P. Mein ArXiv e-prints, 0911.5091 (2009)

C.J. Schrijver, Sol. Phys. 198, 325 (2001)

P. Schwartz, P. Heinzel, B. Schmieder, A&A 459, 651 (2006)

S. Serio, G. Peres, G.S. Vaiana, L. Golub, R. Rosner, ApJ 243, 288 (1981)

R. Soler, R. Oliver, J.L. Ballester, in *Waves and Oscillations in the Solar Atmosphere: Heating and Magneto-Seismology*, ed. by R. Erdélyi, C. Mendoza-Briceño (Cambridge University Press, 2008a), p. 173

R. Soler, R. Oliver, J.L. Ballester, ApJ 684, 725 (2008b)

P.A. Sturrock, ApJ 521, 451 (1999)

Y. Su, A.A. van Ballegooijen, B.W. Lites, E.E. DeLuca, L. Golub, P.C. Grigis, G. Huang, H. Ji, ApJ 691, 105 (2009)

E. Tandberg-Hanssen, *The Nature of Solar Prominences* (Kluwer, Dordrecht, 1995), p. 358

F. Tang, Sol. Phys. 319, 163 (1987)

J. Terradas, I. Arregui, R. Oliver, J.L. Ballester, ApJ 678, L153 (2008)

J. Terradas, R. Molowny-Horas, E. Wiehr, H. Balthasar, R. Oliver, J.L. Ballester, A&A 393, 637 (2002)

W.T. Thompson, B. Schmieder, A&A 243, 501 (1991)

J. Trujillo Bueno, E. Landi Degl'Innocenti, M. Collados, L. Merenda, R. Mano Sainz, Nature 415, 403 (2002)

T. Tsubaki, in *Solar and Stellar Coronal Structures and Dynamics*, ed. by R.C. Altrock (National Solar Observatory, USA, 1988), p. 140

A.A. van Ballegooijen, ApJ 612, 519 (2004)

A.A. van Ballegooijen, N.P. Cartledge, E.R. Priest, ApJ 501, 866 (1998)

A.A. van Ballegooijen, P.C.H. Martens, ApJ 343, 971 (1989)

A.A. van Ballegooijen, P.C.H. Martens, ApJ 361, 283 (1990)

A.A. van Ballegooijen, E.R. Priest, D.H. Mackay, ApJ 539, 983 (2000)

B. Von Rekowski, A. Hood, MNRAS 385, 1792 (2008)

Y.-M. Wang, ApJ 520, L71 (1999)

Y.-M. Wang, ApJ 560, 456 (2001)

Y.-M. Wang, K. Muglach, ApJ 666, 1284 (2007)

Y.-M. Wang, N.R. Sheeley Jr., Sol. Phys. 81, 124 (1989)

H. Wang, J. Chae, J.B. Gurman, T.A. Kucera, Sol. Phys. , 183, 91 (1998)

B.T. Welsch, C.R. DeVore, S.K. Antiochos, ApJ 634, 1395 (2005)

E. Wiehr, M. Bianda, A&A 404, L25 (2003)

A.R. Winebarger, H. Warren, A. van Ballegooijen, E.E. DeLuca, L. Golub, *ApJ* 567, L89 (2002)

A.R. Yeates, D.H. Mackay, *Sol. Phys.* , 254, 77 (2009)

A.R. Yeates, D.H. Mackay, A.A. van Ballegooijen, *Sol. Phys.* 245, 87 (2007)

A.R. Yeates, D.H. Mackay, A.A. van Ballegooijen, *Sol. Phys.* 247, 103 (2008a)

A.R. Yeates, D.H. Mackay, A.A. van Ballegooijen, *ApJ* 680, L165 (2008b)

Z. Yi, O. Engvold, *Sol. Phys.* 134, 275 (1991)

Z. Yi, O. Engvold, S. L. Keil, *Sol. Phys.* 132, 63 (1991)

T. Yokoyama, K. Shibata, *Nature* 375, 42 (1995)

J.B. Zirker, *Sol. Phys.* 119, 341 (1989)

J.B. Zirker, O. Engvold, S.F. Martin, *Nature* 396, 440 (1998a)

J.B. Zirker, O. Engvold, Z. Yi, *Sol. Phys.* 150, 81 (1994)

J.B. Zirker, J.-L. Leroy, V. Gaizauskas, in *New Perspectives on Solar Prominences*, IAU Colloquium 167, ed. by D.F. Webb, B. Schmieder, D.M. Rust, ASP Conf. Series, vol. 150 (Astron. Soc. of the Pacific, San Francisco, 1998b), p. 439

J.B. Zirker, S.F. Martin, K. Harvey, V. Gaizauskas, *Sol. Phys.* 175, 27 (1997)

C. Zwaan, *Ann. Rev. Astron. Astrophys.* 25, 83 (1987)